



UNIVERSITY OF UTRECHT

DEBYE INSTITUTE

NANOPHOTONICS GROUP

An Experimental Design to Beamshape Ultrashort Pulses

Author:
Robbert Schoo BSc

Supervisor:
Dr. Dries van Oosten

July 7, 2016

Abstract

The central objective of this thesis is to design a system that allows control over the spatial intensity distribution of an ultrashort light pulse in a target plane, as a useful tool in researching non-linear light-matter interactions. We will use a blazed digital micromirror device as a binary spatial light modulator (SLM). In Section 2 we present exploratory beamshaping results where smooth shaping of the third diffraction order of the SLM is achieved using a $4f$ setup and a spatial filter placed in the Fourier plane. To generate the correction pattern on the SLM we use a simple intensity-shaping algorithm which assigns a probability to each micromirror to be switched off. In Section 3 we adopt a new setup, using a cylindrical lens to image in one direction and focus in the other. By so collapsing approximately a thousand binary degrees of freedom into a section of about 0.12 mm^2 , we increase the precision of our method and create a flattop with 4.3% rms-flatness. Section 4 concerns the spatial dispersion of the linefocus that is observed for broad input spectra. To simulate the broad spectrum that belongs to an ultrashort pulse, we use a laser diode below its lasing threshold. We find that the orientation of the cylindrical lens can be used to compensate for this dispersion, and we report succesful (flattop) beamshaping using broad spectrum light.

Contents

1	Introduction	1
1.1	Motivation	1
1.2	Existing beamshaping methods	1
1.3	Spatial light modulation	2
1.3.1	Optical characteristics of the DLP4500NIR	2
1.3.2	Blazing the DMD	5
1.3.3	Image mode and Fourier mode	7
1.4	Summary	7
2	Beamshaping in an image plane	9
2.1	Definitions	9
2.2	Beamshaping scheme	9
2.2.1	Strategy	9
2.2.2	Setup	10
2.2.3	Calibration	10
2.2.4	Procedure	12
2.3	Results	15
2.4	Discussion	17
2.5	Conclusion	19
3	Beamshaping behind a cylindrical lens	20
3.1	Linefocus setup	20
3.2	Method of preparation of a beamshaped linefocus	22
3.3	Results and analysis of a beamshaped linefocus	23
3.3.1	Results of intensity fits	26
3.3.2	Results of FWHM fits	27

3.3.3	Results of mean position fits	29
3.3.4	Background fits	31
3.4	Time variation of the linefocus	32
3.5	Shuffling	36
3.6	Conclusion	37
4	Beamshaping broad spectrum light	38
4.1	Characterization of the laser diode	39
4.2	Dispersion due to a broad spectrum	41
4.2.1	Transverse dispersion	43
4.2.2	Longitudinal dispersion	45
4.3	Beamshaping spectrally broadened light	47
4.4	Gaussian fits for vertical and horizontal linefoci above and below threshold	50
4.4.1	Parameter plots	50
4.4.2	Variation over time	53
4.5	Depth of focus and depth of image	55
4.6	Conclusion	56
5	Discussion	59
5.1	Effects of overfilling the DMD	59
5.2	Power efficiency and phase control	60
5.3	Time variation due to periodic mirror flipping patterns	60
5.4	Alignment of the hybrid mode setup	64
5.5	Outlook	64
6	Conclusion	66
7	Acknowledgements	67

Appendix A The paraxial approximation leads to Fourier optics	68
--	-----------

1 Introduction

1.1 Motivation

In current physics, fundamental discoveries are being made by investigating the interaction of light and matter at high intensities, where effects depending on non-linear powers of the field strength (e.g. multiphoton absorption) become measurable. The high intensities necessary to access this physics are reached by tightly focusing a laser beam in space, e.g. by using a high NA microscope objective, and by compressing it in time, creating tightly focused pulses whose peak intensity increases with decreasing pulse duration. Sub-picosecond pulse durations are routinely achieved in this manner, and are an essential tool in the study of non-linear optics.

In this thesis we will develop a method to control the spatial distribution of pulsed light using a spatial light modulator (SLM). A flexible and easily applicable method to precisely control the spatial distribution of fluence¹ on a sample would certainly be a useful tool in researching non-linear light-matter interactions. One could change the (radial) intensity profile of the spot from a quasi-gaussian to a more perfect gaussian, or to any other target shape (see Fig.1.1). The central objective of this thesis is to *design a system that allows control over the spatial intensity distribution of an ultrashort light pulse in a target plane.*

After a very brief look at previous work on beamshaping ultrashort pulses, we will provide a detailed description of the SLM used in this project and explain its principle of operation.

1.2 Existing beamshaping methods

Previous work on beamshaping ultrashort pulses, while not as extensive as the work done on temporal pulse shaping, already contains impressive results. In 2002 a liquid crystal phase mask was employed to elongate the depth of focus of an ultrashort pulse to the centimeter range [14], this method has been perfected in later work by the same research group. It was later employed by their co-workers [10] to also shape the beam profile in the focal plane. Others used a diffraction grating to separate optical frequencies and an optically addressed liquid crystal mask to apply phase delays. By spatially varying the phase delay applied by the mask, spatial shaping of the temporal waveform could be achieved [13]. Himmer et al. [4] pioneered the use of micro-electromechanical technology to create a deformable mirror, which also allowed shaping of the phase of a light-pulse. As will be explained below, our approach differs from these methods in that we will shape the intensity of the pulse directly, rather than through its phase.

¹Fluence is the intensity of a pulse integrated over its duration in time.

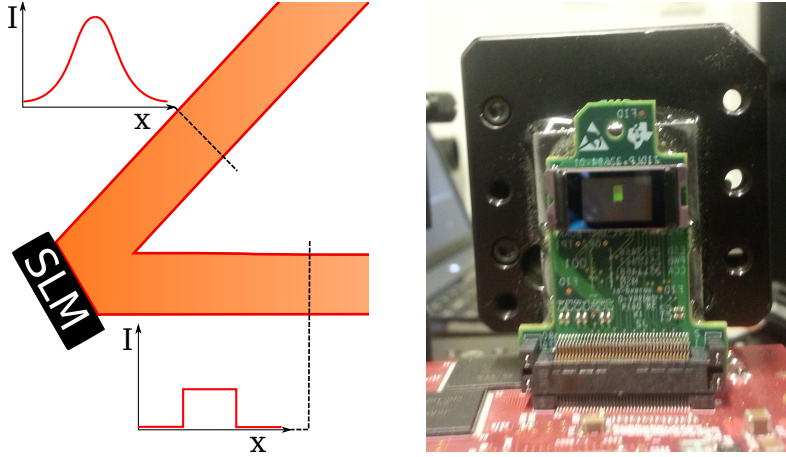


Figure 1.1: *Left* Schematic overview of beamshaping explaining the use of a spatial light modulator (SLM). The target variable is the spatial intensity profile of the cross-section of a beam of light. The input is typically gaussian, the target shape can be chosen at will (a flattop is shown here). *Right* The SLM used in this thesis (TI DLP4500NIR Digital Micromirror Device).

1.3 Spatial light modulation

The SLM we chose to use is a digital micromirror device (DMD). In this section we provide a detailed description of it and explain its principle of operation. A DMD is an array of mirrors whose dimensions are on the order of the wavelength of visible light (about a factor of ten larger, in practice). DMDs were invented in the 1970's for use in digital projectors, but have been applied more recently in scientific settings [3, 5, 16]. Their rapid switching time and programmability are usually considered their main advantage over other SLMs. Our main reason to use a DMD, however, is that it is a reflective device, so that the overlap between the DMD and the beam-intensity is minimal. This is important since we intend to beamshape ultrashort (ablation) pulses and we want to avoid non-linear optical effects which the very high peak intensity of these pulses would cause when they propagate through, for instance, dielectric layers. The Ti:Sapph laser available in our lab has a center frequency of 800 nm so we choose the Texas Instruments DLP4500NIR DMD, which is intended for use in that spectral range.

1.3.1 Optical characteristics of the DLP4500NIR

The DLP4500NIR is an array of square micromirrors arranged in a square lattice that is rotated by 45° w.r.t the sides of the DMD-chip. It is coated to have upwards of 95% reflection in the 700 – 2300 nm wavelength range (for perpendicular incidence). Within $16\mu\text{s}$, the micromirrors can be electronically rotated around their vertical diagonal, placing the micromirror-plane at an angle of $\pm 12^\circ \pm 1^\circ$ with the plane of the DMD (see Fig.1.3). Since the mirrors can only be placed in two positions, DMDs are binary mod-

ulators. In Fig.1.2 a schematic representation of the mirror array of the DLP4500NIR is shown. There are 1140 addressable rows and 912 addressable columns, surrounded by a border of 10 micromirrors which are continuously in the 'on' state (as defined by Fig.1.3). Note that the columns are zig-zagged, making them effectively broader than the rows. Due to this, the vertical side of the active area of the DMD is 6.16 mm and the horizontal side is 9.85 mm, even though there are 30% more mirrors in a column than in a row. The DMD has just over a million binary degrees of freedom on less than a square centimeter.

For some applications, smoother shaping can be attempted by quickly flipping mirrors to produce an average intensity that is a fraction of the on-state intensity. That option is not available to us, however, because the pulses we intend to shape are much shorter than the mirror switching time.

Since the micromirrors are periodically placed, the DMD acts as a 2D diffraction grating. A diffraction grating is an optical instrument that imposes a periodic variation of phase and/or intensity on a beam of light. An excellent derivation, which we will take for granted, of the relation between the periodicity of the grating profile and resulting periodicity of the reflected light field is given in Ref. [7]. We can categorize the diffraction orders produced by the DMD by finding the reciprocal lattice. To do so, we first define the lattice vectors \mathbf{a} and \mathbf{b} as

$$\mathbf{a} = d_{\text{diag}} \left(\frac{\hat{\mathbf{i}} + \hat{\mathbf{j}}}{\sqrt{2}} \right), \quad \mathbf{b} = d_{\text{diag}} \left(\frac{\hat{\mathbf{i}} - \hat{\mathbf{j}}}{\sqrt{2}} \right).$$

Here $d_{\text{diag}} = 7.637 \mu\text{m}$ is the side of a micromirror and the unit vectors $\hat{\mathbf{i}}$ and $\hat{\mathbf{j}}$ are defined in Fig.1.2 (the auxiliary unit vector $\hat{\mathbf{k}}$ points out of the page). There are lattice sites at every position $\mathbf{R}_{mn} = n\mathbf{a} + m\mathbf{b}$ (where $n, m \in \mathbb{Z}$). The angles w.r.t the surface normal at which the diffraction orders leave the lattice depend on the reciprocal lattice vectors \mathbf{a}' and \mathbf{b}' , which are calculated to be

$$\mathbf{a}' = \frac{2\pi}{d_{\text{diag}}} \left(\frac{\hat{\mathbf{i}} + \hat{\mathbf{j}}}{\sqrt{2}} \right), \quad \mathbf{b}' = \frac{2\pi}{d_{\text{diag}}} \left(\frac{\hat{\mathbf{i}} - \hat{\mathbf{j}}}{\sqrt{2}} \right).$$

At any distance from the DMD, the position of the diffraction orders in a plane parallel to the lattice is $\mathbf{R}'_{nm} \propto n\mathbf{a}' + m\mathbf{b}'$. There are orders in both diagonal directions of the micromirror lattice at angles corresponding to the pitch d_{diag} . We use the DMD in a horizontal configuration, meaning we only consider orders for which $\mathbf{R}'_{nm} \propto m(\mathbf{a}' + \mathbf{b}') = \frac{2\pi}{d_{\text{diag}}} \sqrt{2} \hat{\mathbf{i}}$. The spacing between those orders corresponds to a real space pitch of $d \equiv d_{\text{diag}}/\sqrt{2} = 5.4 \mu\text{m}$, i.e. half the diagonal of a micromirror. When a visible laser is used, over sixty diffraction orders can be seen with the naked eye.

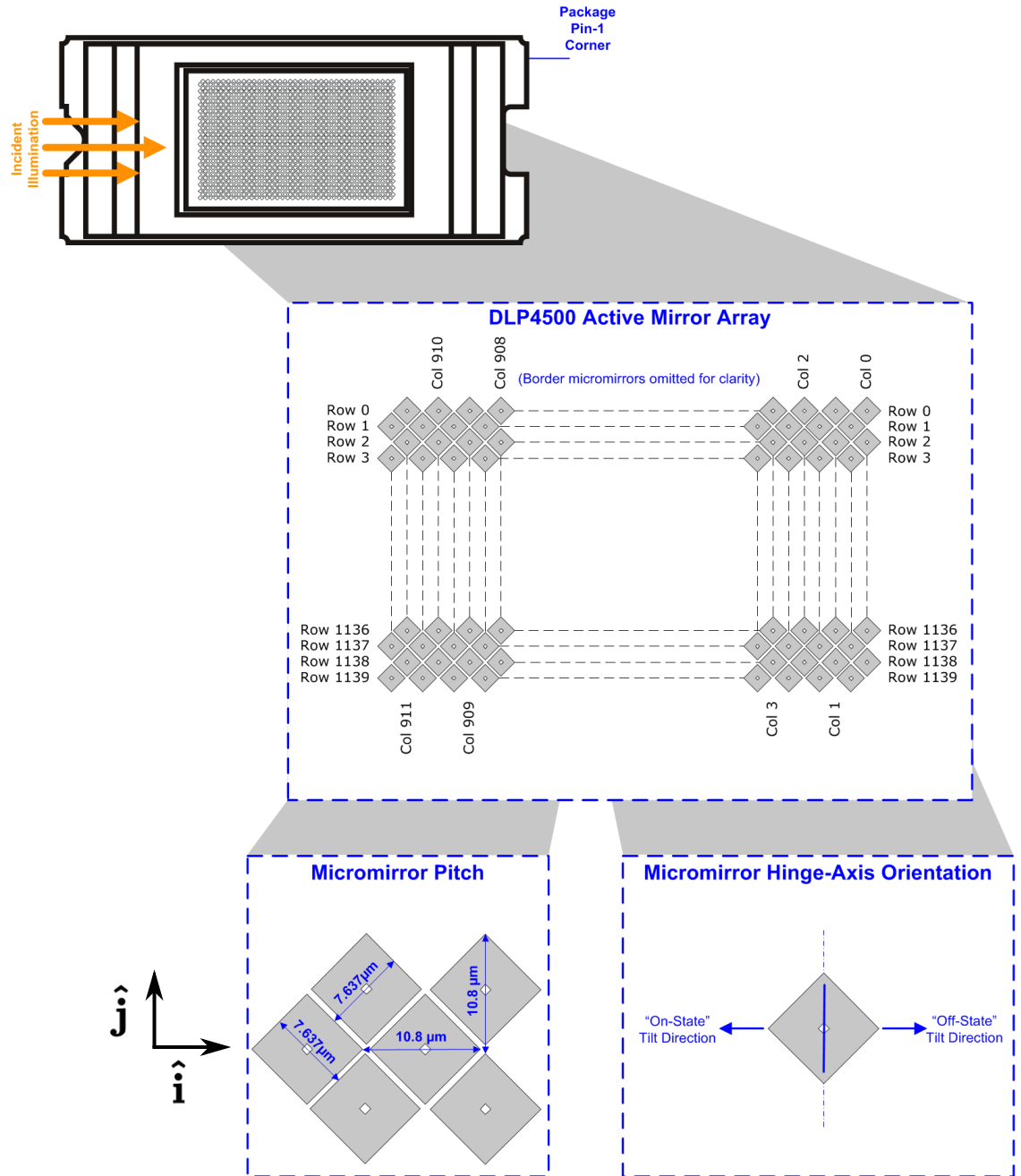


Figure 1.2: Tiling of the DMD and the definition of a row and column. Taken from Ref. [12].

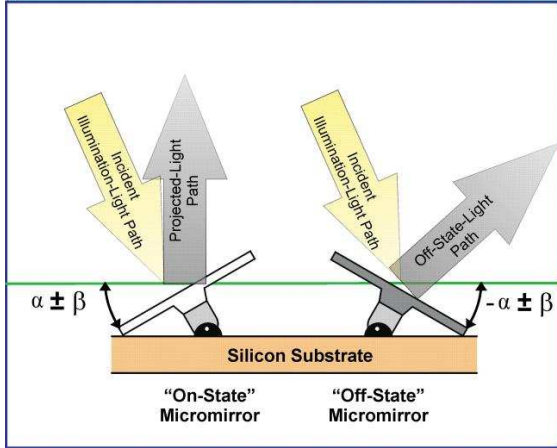


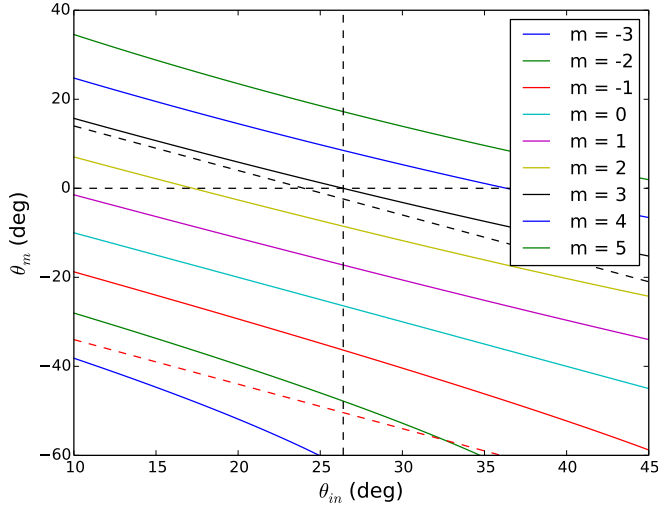
Figure 1.3: Schematic showing the on- and off-states of a single micromirror; $\alpha = 12^\circ$ and $\beta = 1^\circ$. Taken from Ref. [12].

1.3.2 Blazing the DMD

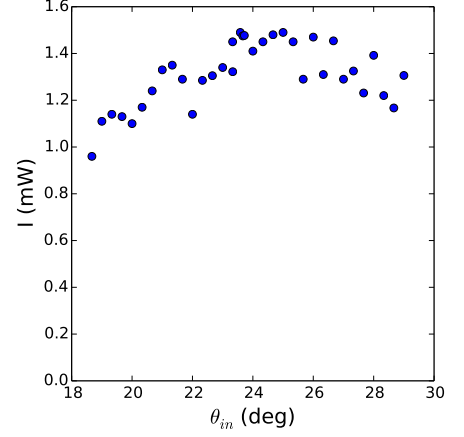
Having determined the directions in which diffraction orders propagate, we next discuss their relative intensities. The distribution of the incident intensity over the diffraction orders hard to determine generally because the shape of the repeating unit of a diffraction grating influences it in a non-trivial way. For slanted planar repeating units, like the micromirrors of the DMD, the distribution of intensity between diffraction orders can be understood through the concept of *blazing*. A grating is said to be blazed when a diffraction order aligns with the specular reflection from a micromirror ($\theta_a = -\theta_b$ in Fig.1.4); blazed orders receive a much larger portion of the incident intensity. Blazing is a familiar phenomenon in the optics industry and is used to increase the efficiency of diffraction gratings (see Ref. [9]).

Due to blazing, the intensity distribution and diffraction efficiency can be controlled by the incident angle, so we must choose it well. The angle at which we operate the DMD is dictated by three requirements. First, the outgoing angle of the diffraction orders must obey the grating equation, so we have $m\lambda = d(\sin(\theta_{\text{in}}) + \sin(\theta_m))$ (see Fig.1.4 for definitions). Second, we want to meet the blazing condition for mirrors in the on-state, meaning $\theta_a = -\theta_b$, or equivalently $-\theta_m = \theta_{\text{in}} - 2\alpha$. Finally, we want the used order to depart perpendicularly to the DMD plane, meaning $\theta_m = 0$, because our intention is to image the DMD's surface. Fig.1.4a shows plots of the grating equation for $d = 5.4 \mu\text{m}$ and $\lambda = 800 \text{ nm}$ and several values of m . From the figure we see that no diffraction order satisfies all three requirements exactly, but that the $m = +3$ order is most convenient because it allows a beam going out perpendicularly when $\theta_{\text{in}} = 26.4^\circ$, which is only 1.4° away from the blazing condition.

It is easy to measure the power in the $m = +3$ order as a function of θ_{in} to determine how much efficiency we lose by not satisfying the blazing condition exactly. A HeNe laser



(a) This figure shows θ_m as a function of θ_{in} for various values of m as dictated by the grating equation. Here, $d = 5.4 \mu\text{m}$ and $\lambda = 800 \text{ nm}$. The horizontal dashed line indicates the normal incidence condition ($\theta_m = 0$). The intersection between the $m = 3$ line and the line $\theta_m = 0$ is at 26.4° , indicated with the vertical black line. The black (red) sloped line is the blazing condition of the on (off) state mirrors ($-\theta_m = \theta_{in} \pm 2\alpha$).



(b) Power of the blazed diffraction maximum ($m = +3$) as a function of angle of incidence.

($\lambda = 632.4 \text{ nm}$) is used to illuminate the DMD with a beam much smaller than the size of the active array with a total power of 2.70 mW . The resulting power in the $m = +3$ order as a function of θ_{in} is shown in Fig.1.4b. In a range of three degrees centered around $\theta_{in} = 24^\circ$, the maximum diffraction efficiency recorded is $1.49/2.70 = 55.2\%$ and the spread $\frac{\sqrt{\text{var}(I)}}{\langle I \rangle}$ is 4.6% . The second brightest order is the zeroth order, which contains 1.0% of the incident power. Since deviations of θ_{in} up to a few degrees do not affect the diffraction efficiency by more than a few percent we conclude that the blazing condition does not need to be met exactly. We used a laser with a wavelength of 632 nm for these measurements, but the same behavior is expected in the near infrared.

Blazing is not only responsible for the high diffraction efficiency of the DMD, but also for the fact that intensity can be removed from a diffraction order by flipping micromirrors at all. When a mirror is flipped to the off-state, its blaze condition becomes $-\theta_m = \theta_{in} + 2\alpha$, and we see in Fig.1.4a that the $m = -2$ order is then close to its blazing condition. The $m = +3$ order is very far from the blaze condition for off-state micromirrors and thus receives almost no intensity from them - they are indeed 'off'.

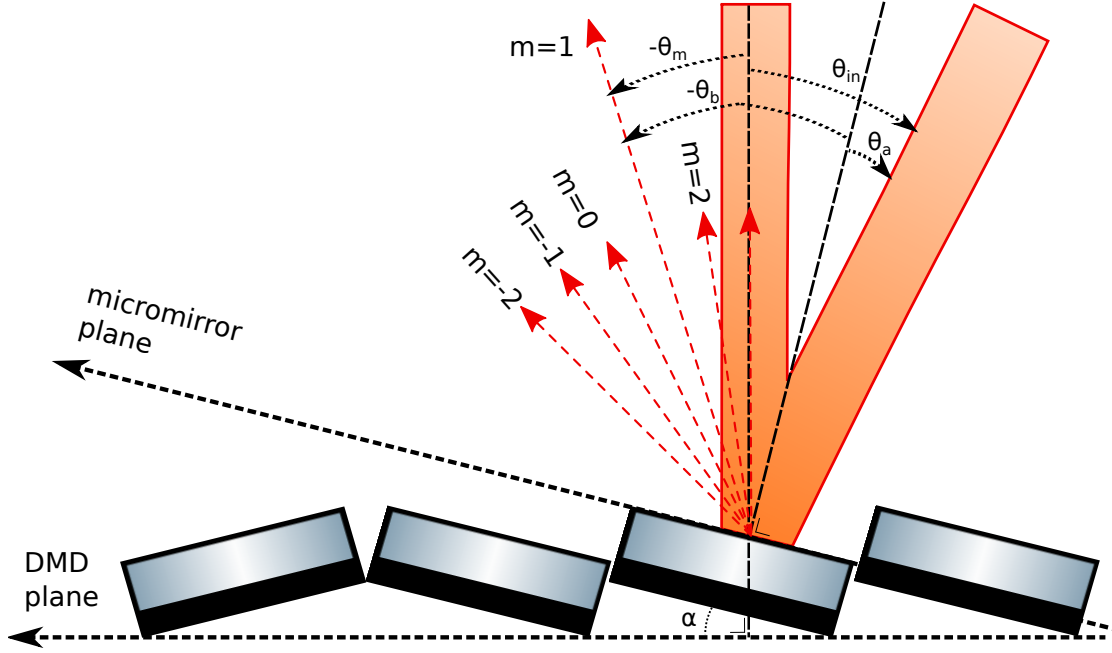


Figure 1.4: This schematic defines the angles used in the text. All angles are positive for clockwise rotation and are shown for the $m = 1$ order.

1.3.3 Image mode and Fourier mode

For later reference, Figure 1.5 illustrates two ways in which DMDs are typically arranged in optical setups. The first is Fourier mode, where the DMD is placed in the back focal plane of a spherical lens and the target plane is in the front focal plane of the same lens. The name is explained by the fact that light fields in the back and front focal plane of a lens are related by a spatial Fourier transform (see Appendix A). The second is image mode, in which a second spherical lens is placed in the beam path and the target plane is chosen in its back focal plane. For an ideal imaging system, the light fields at the DMD and target plane are related by a simple magnification factor.

1.4 Summary

In this thesis we will investigate how to design a system that is able to spatially shape ultrashort pulses in a target plane using a the DLP4500NIR DMD as a binary, programmable SLM.

In Section 2, we use a $4f$ -setup to image the DMD and attempt to create a flattop beam profile in image mode, using a spatial filter to smoothen the profile. In Section 3, we employ a cylindrical lens to create a hybrid plane, where the field at the DMD is Fourier transformed in one direction and imaged in the other. In Section 4, we show that the

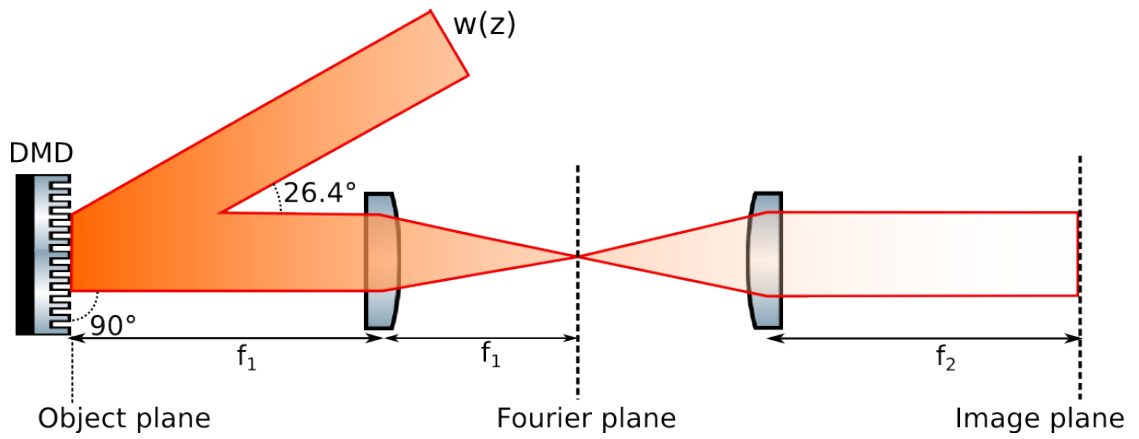


Figure 1.5

hybrid plane setup is able to counteract the significant dispersion that occurs when an ultrashort pulse is passed over a diffraction grating. In the discussion we touch upon some technical aspects of the setup and its operation.

2 Beamshaping in an image plane

For the reasons detailed in Section 1.1 our objective is to create a flat-top beam profile from the (quasi-)gaussian beam profile emitted by our laser diode. In this section we present exploratory beamshaping results where the DMD is imaged using a $4f$ setup and a spatial filter is placed in the Fourier plane. To generate the correction pattern on the DMD we use a simple algorithm which assigns a probability to each pixel to be switched off. The data show that this simple algorithm allows smooth shaping of a beam profile with a binary modulator (see also Ref. [5]) using only intensity modulation.

2.1 Definitions

In accordance with literature the pattern displayed on the spatial light modulator will be called a *kinoform*. Our kinoforms are always binary 2-bit arrays² of 1140 rows by 912 columns. A *beam profile* is the intensity of the light field as a function of position and time in a plane perpendicular to the beam propagation direction. For a beam propagating in the z direction $I(x, y, z_0, t) = \frac{1}{2}\varepsilon_0 c \mathbf{E}(x, y, z_0, t) \cdot \mathbf{E}^*(x, y, z_0, t)$, where I is the beam profile at position z_0 . Usually, the signal we analyze is the output of a CCD-camera placed in the target plane, which we will call $S(x, y)$. Finally, we define the shaping strength η as the fraction of the DMD pixels that are in the off-state. By this definition, $\eta = 0$ when all mirrors are in the on-state and $\eta = 1$ when all mirrors are in the off-state.

2.2 Beamshaping scheme

2.2.1 Strategy

Our strategy for beamshaping is simple. We define a target plane in the beampath after the DMD, measure $I_{\text{target}}(x, y, t)$ there, and turn off pixels on the DMD in areas where the measured intensity is above the target value. Since the target plane and the surface of the DMD do not coincide, this approach requires a mapping from the intensity at the target plane to the DMD. This mapping is relatively easy to obtain in a so-called $4f$ -setup (see Fig. 2.1). Two lenses are placed a distance $f_1 + f_2$ apart, thus performing two consecutive spatial Fourier transformations of the light field at a distance f_1 before the first lens³. By the invertibility of the Fourier transform the field in the front focal plane of the second lens is identical to the field in the back focal plane of the first lens, up to a magnification factor and the point spread function of the optical system. The

²When displaying an 8-bit bitmap only AD-units of 0 and 255 are used.

³Appendix A contains a derivation of the result that lenses perform Fourier transformations between their back and front focal planes.

exact mapping between CCD pixels and 'DMD pixels' (i.e. the micromirrors) will be determined in Sec.2.2.3.

Smooth shaping with a binary modulator requires more than a standard $4f$ -setup, because turning off a DMD pixel introduces sharp edges (in image mode). The trick is to use the Fourier plane that is created between the two lenses to our advantage. Since sharp edges correspond to high spatial frequencies⁴, they pass through the Fourier plane far from the optical axis ($k = 0$) and can be blocked by a circular aperture centered on that axis. The aperture is used as a low-pass *spatial filter*, broadening the point spread function of the imaging system. Qualitatively, the image is blurred when the aperture is closed.

2.2.2 Setup

A CCD-camera is positioned in the image plane, perpendicularly to the optical axis so that it records the beam profile in the target plane. The auto-adjust features of the camera, a simple 480×640 Logitech C270 webcam, could not be switched off, but since the relative flatness of the measured intensity distribution is not influenced by these auto-adjustments this is not problematic. We work with a large beam waist ($2w_0 \sim 1$ cm), overfilling the DMD. The power loss due to overfilling ($I_{\text{in}}\eta_{\text{overfilling}}$) is traded off to the reduction in power loss due to the shaping itself ($I_{\text{in}}(1 - \eta)$). The total efficiency of the beamshaping procedure can be factorized as $\eta_{\text{total}} = \eta_{\text{overfilling}} \times \eta_{\text{diffraction}} \times (1 - \eta)$, where $\eta_{\text{diffraction}} = 55\%$ (see Sec. 1.3). Special care is taken to ensure that the DMD surface is perpendicular to the optical axis and that the (blazed) diffraction order propagates parallel to the DMD-surface normal, so that the entire DMD is imaged at the camera.

2.2.3 Calibration

We now describe how to find the mapping between CCD pixels and DMD pixels. We use functions from the python cv2 package, which is dedicated to image processing, to implement a standard method in camera calibration that achieves sub-pixel accuracy. The trick is to display a chessboard pattern on the DMD (see Fig.2.2), whose lines are straight and whose surfaces are square, and determine the transformation needed on the recorded image to make sure the recorded chessboard is straight and square.

Our calibration script is based on the following functions:

- `cv2.cornerSubPix()` is used for contrast-based corner detection. It is applied to both the recorded image and the kinoform to obtain two sets of corner coordinates, which are supposed to be the corners of the checkerboard. It is crucial that the

⁴In other words, high order terms in a Fourier expansion to accurately represent sharp edges.

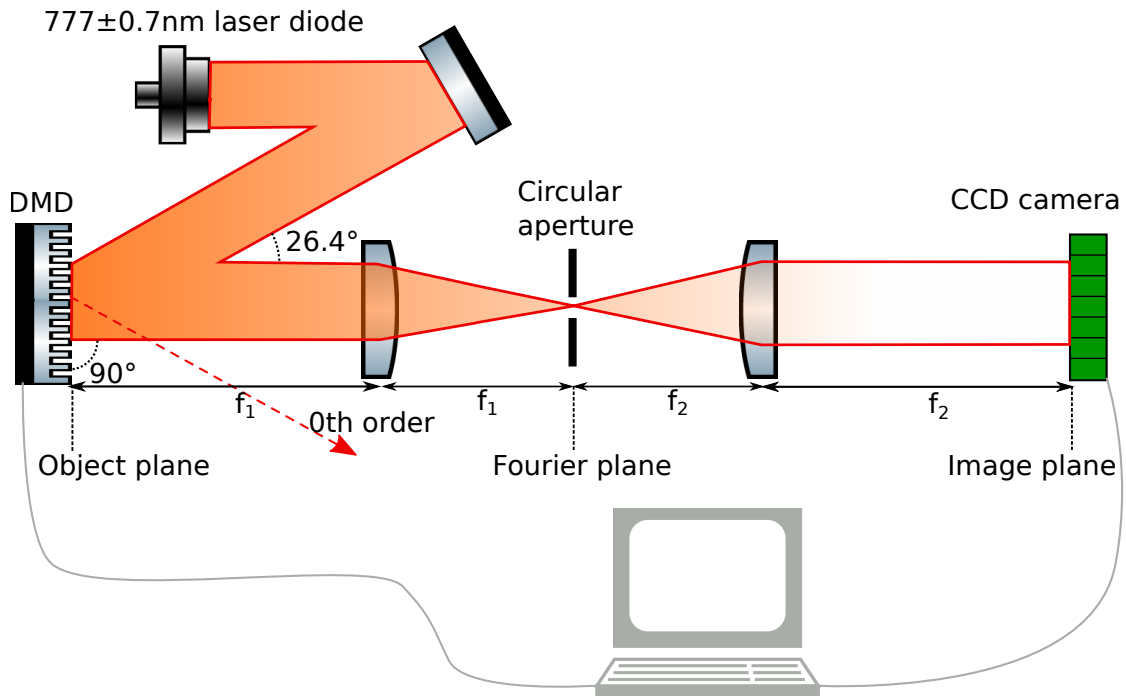


Figure 2.1: Schematic of the $4f$ image-mode beamshaping setup, $f_1 = 150 \text{ mm}$ and $f_2 = 50 \text{ mm}$. The target plane is the surface of the CCD camera (Logitech C270), where a magnified image of the DMD surface is created. The spherical aperture is placed in the Fourier plane (w.r.t. the object plane), so the aperture acts as a low-pass spatial filter. Some elements have not been depicted: a telescope right after the laser diode which enlarges the beam, a second mirror which aids in aligning the DMD and some neutral density filters.

entire displayed checkerboard is visible on the camera so that all corners can be found. The resulting corner coordinates are drawn in Fig.2.2.

- `cv2.calibrateCamera()` and `cv2.undistort()`; the first function analyzes the corners found by `cv2.cornerSubPix()` and determines distortion parameters, needed if the detected chessboard does not have straight lines. The second function applies the distortion transformation. These functions together generate an image that is free of all distortions except those that are due to perspective transformations.
- `cv2.getPerspectiveTransform()`. Uses the (outermost) undistorted corners to calculate an affine transformation. This means that only distortions due to rescaling and 2D projections of rotations are calculated.

The final output of these functions are two 3x3 matrices and five distortion parameters which serve as input for `cv2.warpPerspective()`, together with the image to be transformed. The `warpPerspective` function then outputs the same image mapped onto the DMD pixels. Corners are more easily detected if the input image is divided by a checkerboard image before analysis because that division cancels the quasi-gaussian beam profile.

2.2.4 Procedure

The recipe for beamshaping in image mode is as follows:

- Determine the calibration transformation by displaying a chessboard pattern and running the calibration script.
- Establish a region of interest (ROI) and a target intensity, which has to be lower than or equal to the lowest intensity in the ROI.
- Turn off all pixels outside the ROI and record $S(x, y)$ with the aperture open.
- Apply the calibration transformation to the recorded figure to map it on the DMD pixels.
- Give each pixel a probability to be switched off, where that probability increases with the difference between the target and measured intensity in that region. Generate a beamshaping kinoform.
- Display the shaped kinoform on the DMD; the recorded image is now beamshaped.
- To smoothen the beamshape, filter out high spatial frequencies from the object plane by closing the aperture.

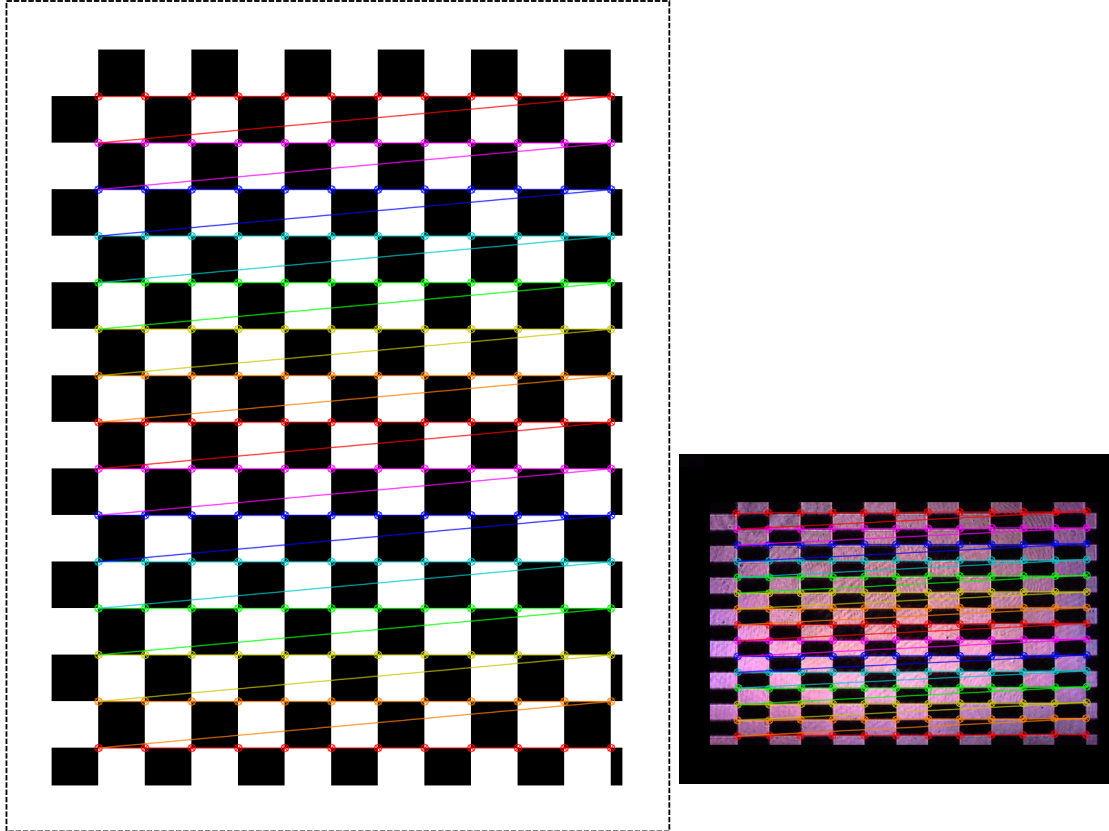
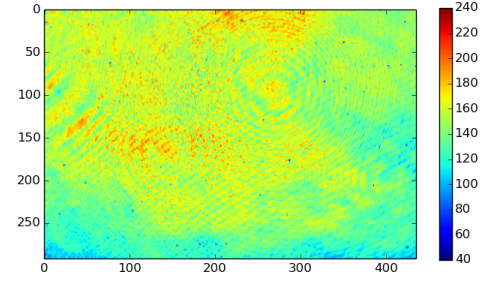
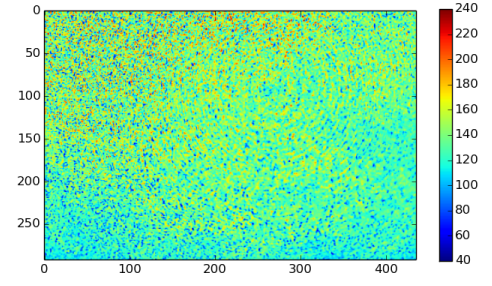
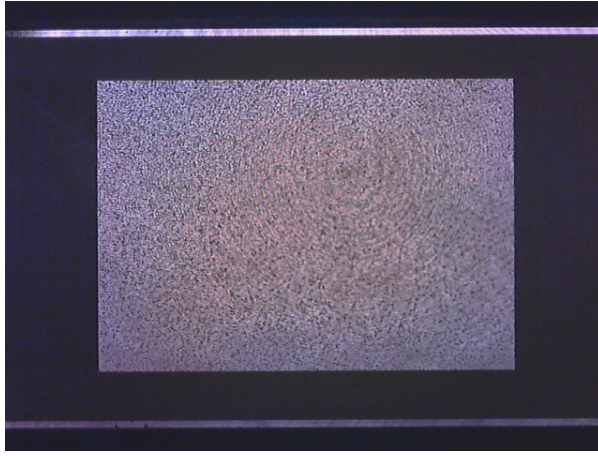


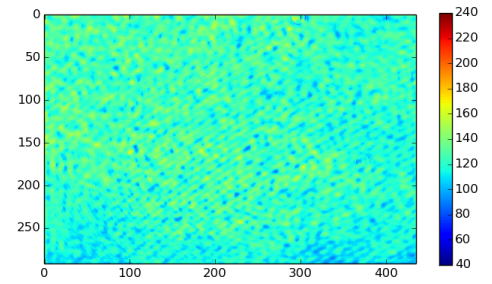
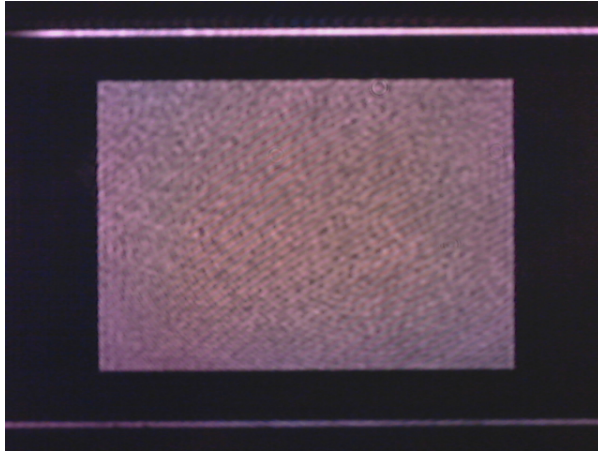
Figure 2.2: *Left* The checkerboard kinoform (1140×912 pixels). *Right* Camera recording corresponding to the kinoform (480×640), both images are to scale in units of their respective pixel dimensions. The corners found by the calibration script in each image are drawn in color. The pattern is inverted, due to the direction from which the laser beam is incident on the DMD in this example. The aspect ratio of the pattern is changed because the diamond configuration of the DMD pixel array (see Sec. 1.3).



(a) Unshaped, unfiltered. $\sqrt{\text{var}(S_{\text{ROI}}(x, y))} = 16.6$, $\langle S_{\text{ROI}}(x, y) \rangle = 135.4$, $\eta_{\text{ROI}} = 0$.



(b) Shaped, unfiltered. $\sqrt{\text{var}(S_{\text{ROI}}(x, y))} = 23.9$, $\langle S_{\text{ROI}}(x, y) \rangle = 133.9$, $\eta_{\text{ROI}} = 0.519$.



(c) Shaped, filtered. $\sqrt{\text{var}(S_{\text{ROI}}(x, y))} = 9.57$, $\langle S_{\text{ROI}}(x, y) \rangle = 123.3$, $\eta_{\text{ROI}} = 0.519$.

Figure 2.3: These figures qualitatively explain the flow of the beamshaping procedure. (a) shows the signal $S(x, y)$ before beamshaping. On the left the camera recording is shown and on the right a color plot of the region of interest (ROI), which was a rectangle with (88, 102) and (380, 538) (row, column) as corners. The standard deviations and means reported are calculated for within this ROI. In (b) a beamshaped image was displayed on the DMD. In (c) the aperture was closed. The horizontal bars on the top and bottom are due to a rim of 10 inactive pixels which frame the active area of the DMD.

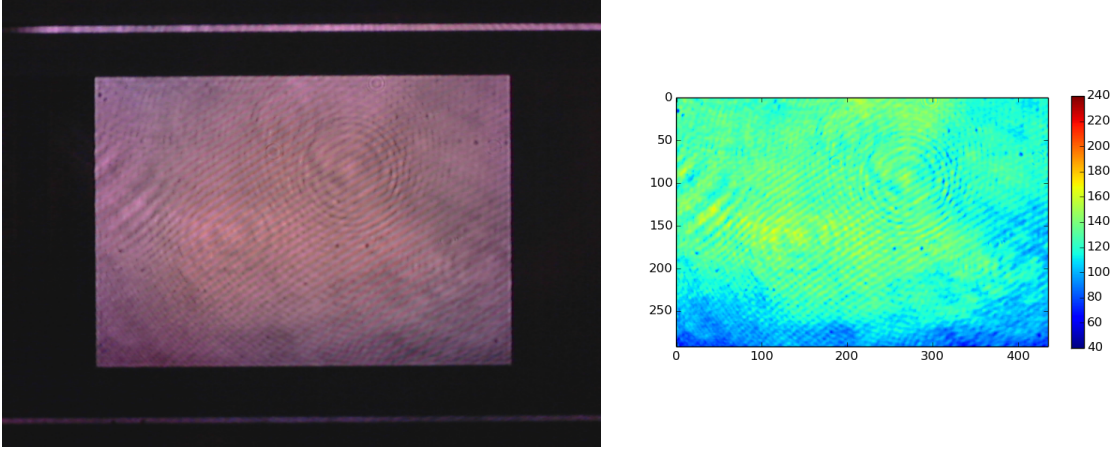


Figure 2.4: For comparison to Figure 2.3a, this picture shows the effect of spatial filtering without beamshaping. $\sqrt{\text{var}(S_{\text{ROI}}(x, y))} = 14.5$, $\langle S_{\text{ROI}}(x, y) \rangle = 123.5$, $\eta_{\text{ROI}} = 0$.

In this scheme we use the DMD to shape the amplitude of the light field non-iteratively, distributing off-pixels probabilistically in proportion to the excess intensity. Figs. 2.3 and 2.4 show examples of $S(x, y)$ before and after beamshaping with open and closed apertures.

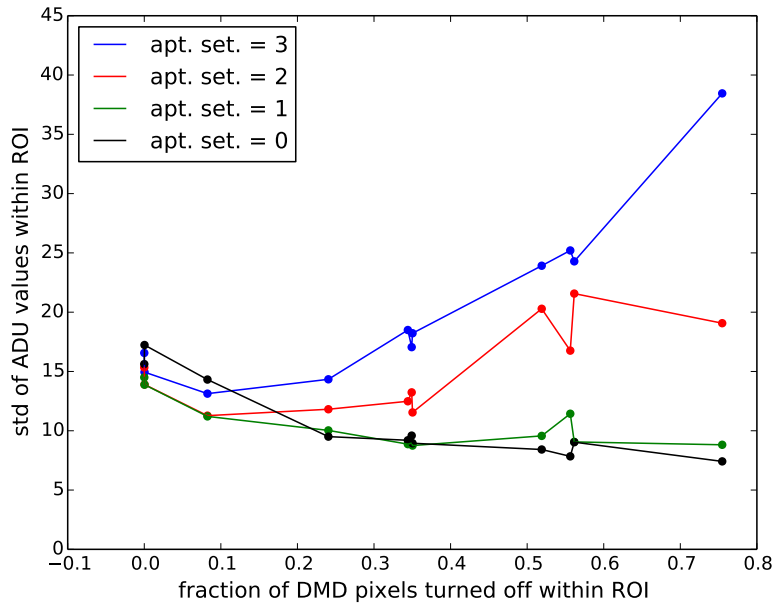
For these trials, we only shaped within a rectangle in the center of the DMD to reduce the necessary shaping strength. No effort was made to produce a neat beam-profile prior to the DMD, as the beamshaping procedure should be able to clean up the beam.

2.3 Results

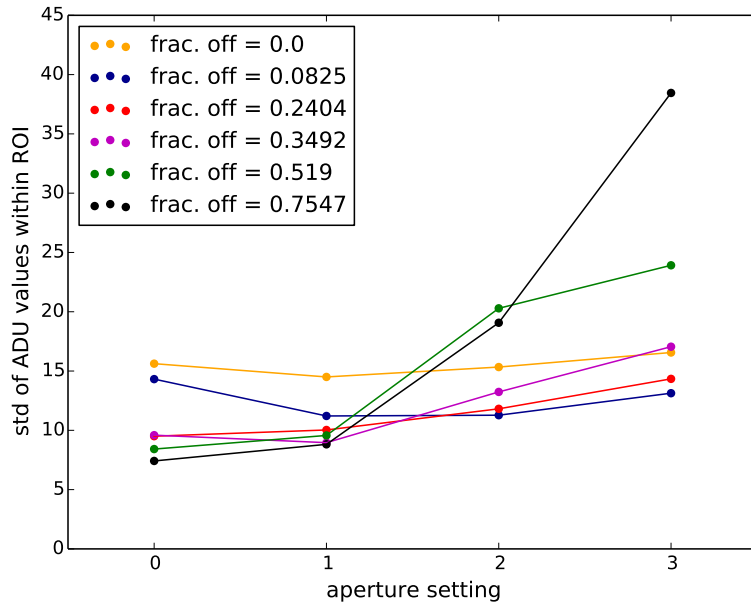
In Figure 2.5 the results of eleven beamshaping routines at various shaping strengths are plotted for four settings of the spatial filter aperture. Prior to beamshaping, all pixels within the ROI are on and all pixels outside the ROI are off ($\eta_{\text{ROI}} = 0$). Regrettably, the aperture settings could not be made quantitative with the available equipment but care was taken to reproduce the same settings in every iteration of the routine. Setting 3 is open (aperture diameter > 1 cm), setting 0 is closed (aperture diameter ~ 1 mm) and settings 2 and 1 are intermediate aperture sizes.

We are interested in creating a flattop, meaning that we the standard deviation (sd) of $S_{\text{ROI}}(x, y)$ to be as small as possible. Since we are only interested in relative flatness of the shaped image, a power calibration of the signal is unnecessary and we use uncalibrated Analog-to-Digital Units (ADU). Since we used an 8-bit camera the ADU take integer values between 0 and 255 (2^8).

Fig. 2.5a highlights the effect of varying the beamshaping strength on the flatness of the flattop. Indeed, the lowest sd is achieved for the strongest beamshaping, although the



(a) Standard deviation within ROI vs. η_{ROI} . The aperture setting is indicated in the legend. Setting 3 is open (aperture diameter > 1 cm), setting 0 is closed (aperture diameter ~ 1 mm).



(b) Standard deviation vs. aperture setting (large aperture to the right) for six selected beamshaping strengths. The y-axis measures the flatness of the flattop and the x-axis the amount of spatial filtering (strongest filtering on the left). η_{ROI} is given in the legend.

Figure 2.5: Two different representations of the same data. The yellow line in the bottom plot is the unshaped reference, corresponding to the left-most points in the top plot.

figure shows that the effect improves only marginally when $\eta_{\text{ROI}} > 0.2$.

Fig.2.5b highlights the effect of closing the aperture. The yellow line is a reference, which shows the effect of spatial filtering for $\eta_{\text{ROI}} = 0$. Observe that strong shaping increases the sd of the flattop if there is no spatial filtering, but that the introduced error is all filtered out when the aperture is closed. A direct look at the images shows that the increase in sd that found for several values of η when going from aperture setting 2 to 3 (Fig. 2.5b) is due to the aperture cutting into the side of the ROI, adding low spatial frequency deviations from the target flattop intensity.

Fig.2.6 shows spatial Fourier transforms of $S_{\text{ROI}}(x, y)$, illustrating the operating principle of binary beamshaping in image mode. The beamshaping procedure shifts the standard deviation within the ROI from low spatial frequencies to high spatial frequencies. In real space, this means that the sd due to the quasi-gaussian beam profile is transferred to sharp dark spots caused by off-state micromirrors, which can subsequently be filtered out by the aperture, leaving a beamshape that is closer to a flattop.

The lowest rms-flatness (the standard deviation divided by the mean value) achieved within the ROI in image mode is 7.5%. The remaining error is mainly due to phase effects occurring after the DMD in the beampath, which cause interference bands such as the diagonal ones seen in Fig.2.3 and the Fourier transforms in Fig.2.6. Optical interference patterns due to, for instance, dust specks on the optics between the DMD and the CCD or Fabry-Perot like interferences in the glass covering the CCD limit the flatness because they disrupt the point-to-point mapping on which our method relies. Since we operate the DMD in image mode, we cannot influence the phase profile directly, but we can reduce the background in regions where the interference is constructive. However, the whole ROI then has to be lowered to the deepest interference fringe, meaning that power efficiency goes down radically. This effect may explain the small decrease in sd observed for $\eta_{\text{ROI}} > 0.25$.

2.4 Discussion

Two points related to the data presented in this chapter merit a short discussion, namely, Moiré interference and time variation of $S(x, y)$.

In the imaging setup, Moiré effects can be observed when a diagonal grating with a pitch of 3 or more pixels is displayed on the DMD, but not for smaller pitches. Moiré patterns are basic interferences due to the overlap of two periodic structures, for instance between the DMD array and the CCD array. They can be distinguished from optical interference effects because Moiré patterns are very sensitive to the relative orientation of the grids. The observed Moiré patterns disappeared upon spatial filtering. Moiré interference between the DMD and CCD lattice is clearly beyond the resolution of our imaging setup and does not contribute significantly to the remaining spatial variation of the flattop.

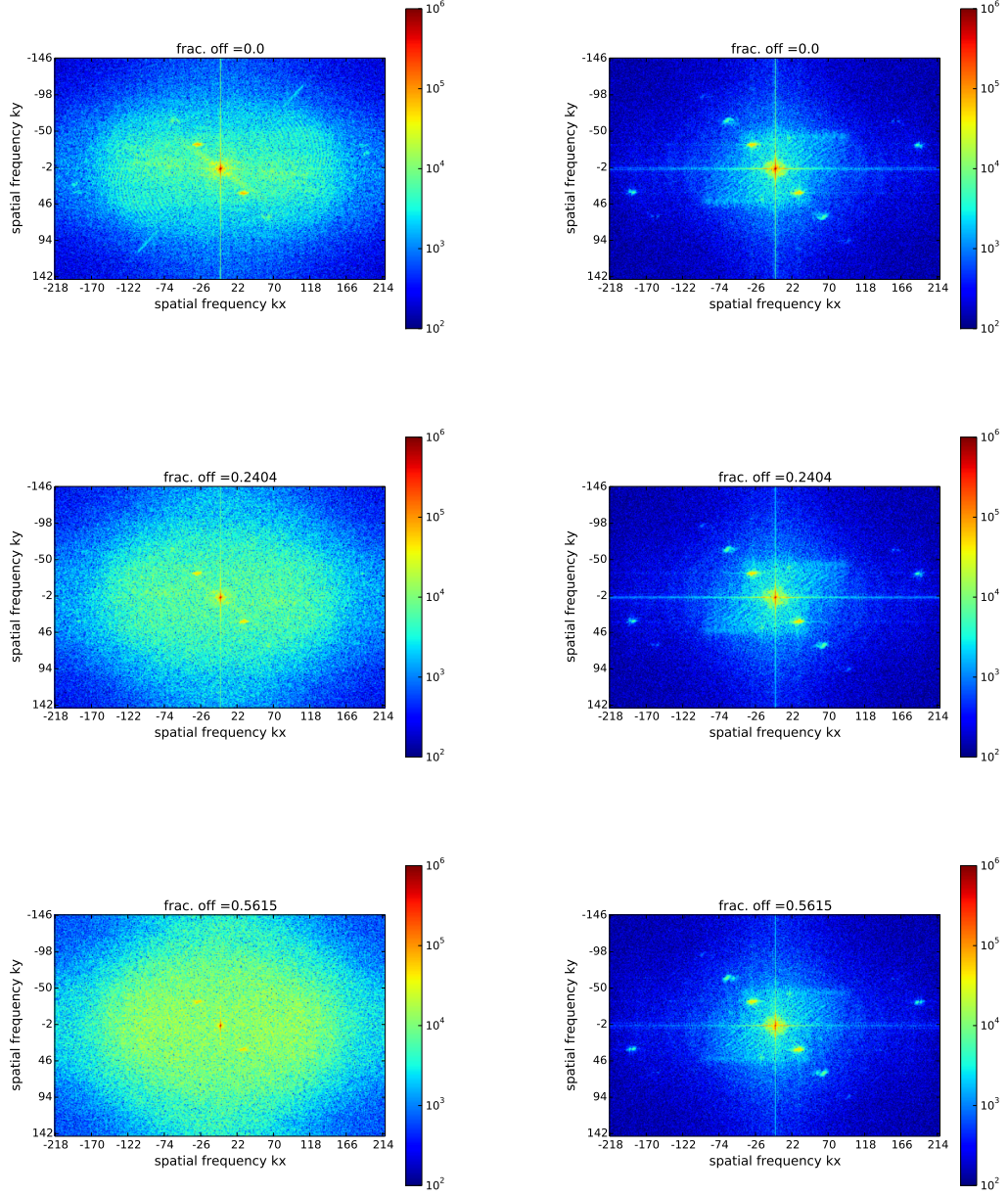


Figure 2.6: 2D Fourier transforms (FFT-algorithm) of the ROI for increasing η_{ROI} . On the left, the aperture is open (setting 3) while on the right it is closed (setting 0). The color bar is logarithmic and low spatial frequencies are at the center of the plot. Observe how the beamshaping procedure adds high spatial frequency noise, but also narrows the peak at the center.

In the above, we have assumed that $S(x, y)$ is time independent. Since our algorithm allows several seconds to pass between the recording of the unshaped and the shaped images, time variation of $S(x, y)$ can compromise our method. Curiously, the camera image was observed to fluctuate periodically over time, but only in regions where $0 \lesssim \eta \lesssim 1$. The camera shutter time was adjusted to integrate those fluctuations over an integer number of periods, so all data reported in this chapter should in fact be regarded as a time average of a periodically varying signal. The reason for this periodic fluctuation is explained in detail in Section 5.3.

2.5 Conclusion

We conclude that, although proof of principle is established beyond doubt, intensity control is insufficient to generate patterns from an arbitrary beam in the image plane to the accuracy we desire. To improve the results without changing the approach, additional effort would have to be put into cleaning up the beam before passing it over the DMD, but that would defy its purpose, since we want to use the device itself to clean up the beam.

3 Beamshaping behind a cylindrical lens

In this chapter we aim to improve the rms-error of the flattop by increasing the number of controllable degrees of freedom per area in the target plane. This is achieved by focusing the beam in one direction, using a cylindrical lens. The result is a strongly elongated focus measuring a few microns by a few centimeters (see Fig.3.2 and Table 3.1).

This chapter will show that a linefocus setup allows the control of the intensity profile that we need along its elongated direction. The rms error of the peak intensity is reduced to 4.3% (compared to an rms error of 7.5% in the previous chapter).

3.1 Linefocus setup

Compared to the image mode setup used in the previous chapter we made the following general improvements:

- To reduce vibrations, the micro-mirror array is glued to an optical mount and fixated separately from its control board.
- A scientific camera (Pointgrey Chameleon CMLN-13S2M-CS, 1280×960 px, $3.75 \mu\text{m}$ pitch) is installed which allowed full control of its settings (shutter time, gain etc.). All gain and auto-adjust features are disabled. We first removed two sheets of glass that were in front of the camera, which were found to cause Fabry-Perot like interferences with the infrared wavelength of our laser.
- An infrared (777 nm) laser diode is pigtailed to a single-mode optical fiber (Thorlabs LPS-785-FC) which is directly connected to a collimation lens (Thorlabs F810FC-780) to produce a wide, collimated beam (~ 0.75 cm beam diameter). Passing the laser through a single-mode optical fiber creates a more gaussian beam-profile compared to the direct output of the laser diode. The beam waist is, again, intentionally made larger than the DMD active array, to reduce the intensity variation of the input beam to be shaped.

The optical setup in Fig.3.1 shows the optics of the hybrid mode setup. The beam is incident on the DMD under an angle of 26.4° so that a blazed diffraction order exits perpendicularly from its surface. A spherical lens ($f = 15$ cm) is placed in the beam, the DMD is positioned in the back focal plane of this lens and the camera in its front focal plane. A cylindrical lens ($f = 12.5$ cm) is placed 2.5 cm behind the positive lens so that the back focal planes of the cylindrical and the spherical lenses coincide, completing the setup. A cylindrical lens has an infinite radius of curvature in its inactive direction and a finite one, corresponding to its focal length, in the orthogonal direction. The active direction of the cylindrical lens images the DMD, while the inactive direction of

the cylindrical lens allows the spherical lens to create a focus (i.e. a Fourier transform). Nota bene: it is not the cylindrical lens that focuses the beam in this setup, but the spherical lens. If different focal distances are chosen, the order of the spherical and cylindrical lenses could be reversed.

Ray optics shows that two consecutive, positive lenses create an image of the back focal plane of the first lens in the front focal plane of the second lens regardless of the distance between the lenses and that the magnification of the image is, in this case, $12.5/15$. This means one row of the DMD is imaged on ~ 2.1 rows of camera pixels.

We align the linefocus setup using the following steps:

- Place the DMD in the back focal plane of the spherical lens by using a ruler to measure the distance.
- Position the camera in the front focal plane by adding a mirror between the DMD and the spherical lens and imaging a scene at a large distance. This method is preferable to the obvious alternative -finding the smallest beam waist of a collimated beam passing over the DMD and through the lens- because a slight curvature of the DMD's surface produces fringes around the DMD's Fourier plane. This curvature makes it impossible to determine the position of the front focal plane with sufficient precision by using a coherent light source that passes the DMD.
- Insert the cylindrical lens.
- Move back the camera to account for the fact that the inactive direction of the cylindrical lens has a different refractive index than the surrounding air. This causes a slight increase of the focal distance of the spherical lens. Using gaussian optics, the necessary adjustment is calculated to be 0.3 mm.
- Finally, adjust the position of the cylindrical lens until the camera is in the imaging plane. The imaging plane is recognized by creating a sharp edge on the DMD and making its image as sharp as possible.

Besides the proper placement of the optical elements along the optical axis, proper imaging of the DMD's rows requires that the active direction of the cylindrical lens and the side of the DMD are parallel. To that end, the cylindrical lens was mounted on a stage that allowed it to rotate around the optical axis of the system.

In the transverse direction, all ~ 1000 pixels of a DMD-column are focused together, allowing smooth shaping of the intensity. In the longitudinal direction, each DMD row is imaged separately, so that the intensity of longitudinal sections of width $\sim 8 \mu\text{m}$ can be adjusted separately. We have turned the target plane into a hybrid of image plane in the longitudinal direction and Fourier plane in the transverse direction.

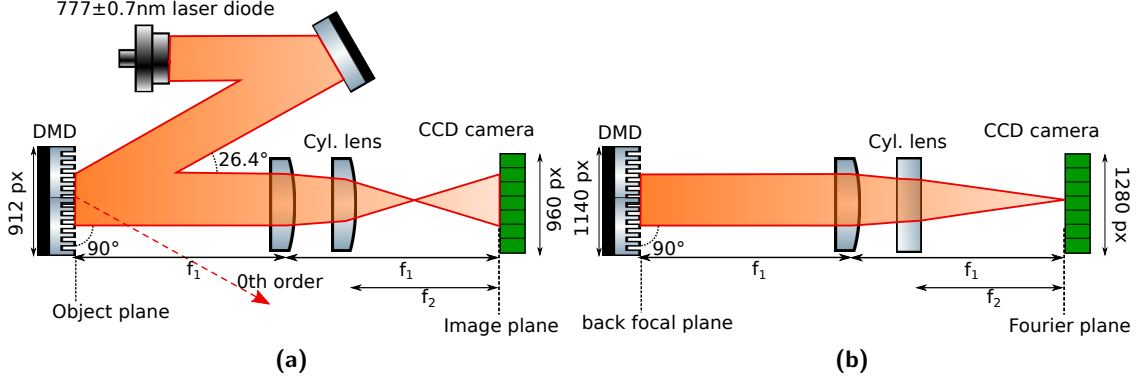


Figure 3.1: The hybrid mode setup. Because the beam is now focused in one direction, attenuators are placed immediately after the laser diode to avoid camera saturation, but these are not depicted. (a) Top view of the setup, showing the active direction of the cylindrical lens creating the longitudinal dimension of the linefocus. (b) Side view, showing the inactive direction of the cylindrical lens and the transverse dimension of the linefocus.

3.2 Method of preparation of a beamshaped linefocus

To shape the beamprofile, a calibration map between rows of the CCD and columns of the DMD⁵ is needed. A convenient way to create this mapping is to switch on a single column on the DMD and let it walk off both edges of the CCD. When the maximum intensity of the entire image coincides with the edge of the CCD, the DMD-column turned on at that time corresponds to the edge of the CCD. After finding the positions of the edges this way, a linear interpolation specifies the rest of the mapping.

The signal used to determine the beamshaped kinoform is S_{BS} , defined as

$$S_{BS}(y) = \sum_{x_{\min}}^{x_{\max}} S(x, y).$$

Where $S(x, y)$ is the recorded image and x_{\max} and x_{\min} are the boundaries of a rectangular region of interest (± 20 px) around the linefocus. S_{BS} is a convenient target variable, because it can be calculated quickly, and it is insensitive to both discretization errors and small fluctuations of the position of the linefocus, if x_{\max} and x_{\min} are chosen far enough apart. The number of pixels to be turned off in each CCD row is determined by the following formula

$$N_{\text{off}}(y) = \lfloor \frac{1140}{1.80} \times (1 - I_{\text{target}}/S_{BS}(y)) \rfloor.$$

⁵Practicalities of our setup requires the camera to be rotated by 90°, so that a row on the camera corresponds to a column on the DMD.

Where $N_{\text{off}}(y)$ is the number of pixels to be turned off in the DMD-column corresponding to CCD-row y (maximum 1140) and I_{target} is the target intensity. Surprisingly, the constant of proportionality between N_{off} and the measured laser power was not 1, but $1/1.80$. Its value depended on the details of the setup, in particular the magnification factor. This factor is probably related to the DMD-addressing issues discussed in Sec.5.3.

When N_{off} is known for all DMD-columns, the beamshaping kinoform is generated and displayed on the DMD. It is important to note that the locations of the off-pixels within each DMD-column were randomized. Fourteen seconds elapsed between the recording of the unshaped and the shaped image in Section 3.3.

Fig.3.2 shows the camera images recorded before and after shaping. These images are analyzed in detail in the next section.

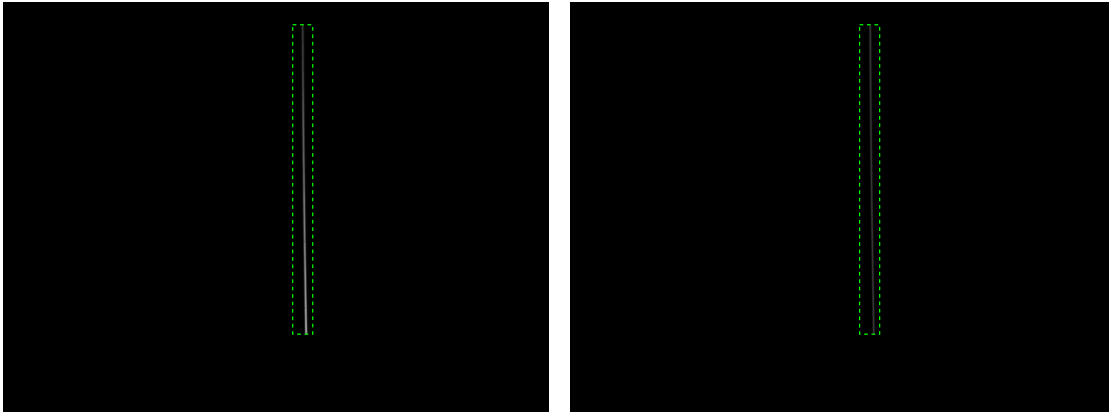


Figure 3.2: The figure shows the data analyzed in this section. On the left, the prepared linefocus before beamshaping - all DMD mirrors are in their 'on' position. On the right, the linefocus after beamshaping, where some mirrors have been flipped. The dashed line indicates the region of interest (730×40 pixels), which is identical in both images.

3.3 Results and analysis of a beamshaped linefocus

We are primarily interested in how the rms-flatness (the standard deviation divided by the mean value) of the peak intensity (I_{peak}) of the shaped light field compares to that of the unshaped light field. To obtain I_{peak} with sub-pixel accuracy, we perform a least-squares fit for each row of the recorded image using Python's orthogonal linear regression package (the module *scipy.odr*). Since the linefocus is only a few camera pixels wide, the discretization of the signal by CCD-pixels has a large effect on the maximum intensity recorded within a row. Performing fits is therefore crucial to find realistic values for the peak intensity. In this section we first report and interpret the results of these fits for a single linefocus before and after beamshaping. Next we compare the temporal variation of the fit parameters to their spatial variation, to determine whether temporal fluctuation of the signal limits the rms-flatness. Finally we investigate the variation of

the flatness between different beamshaping trials.

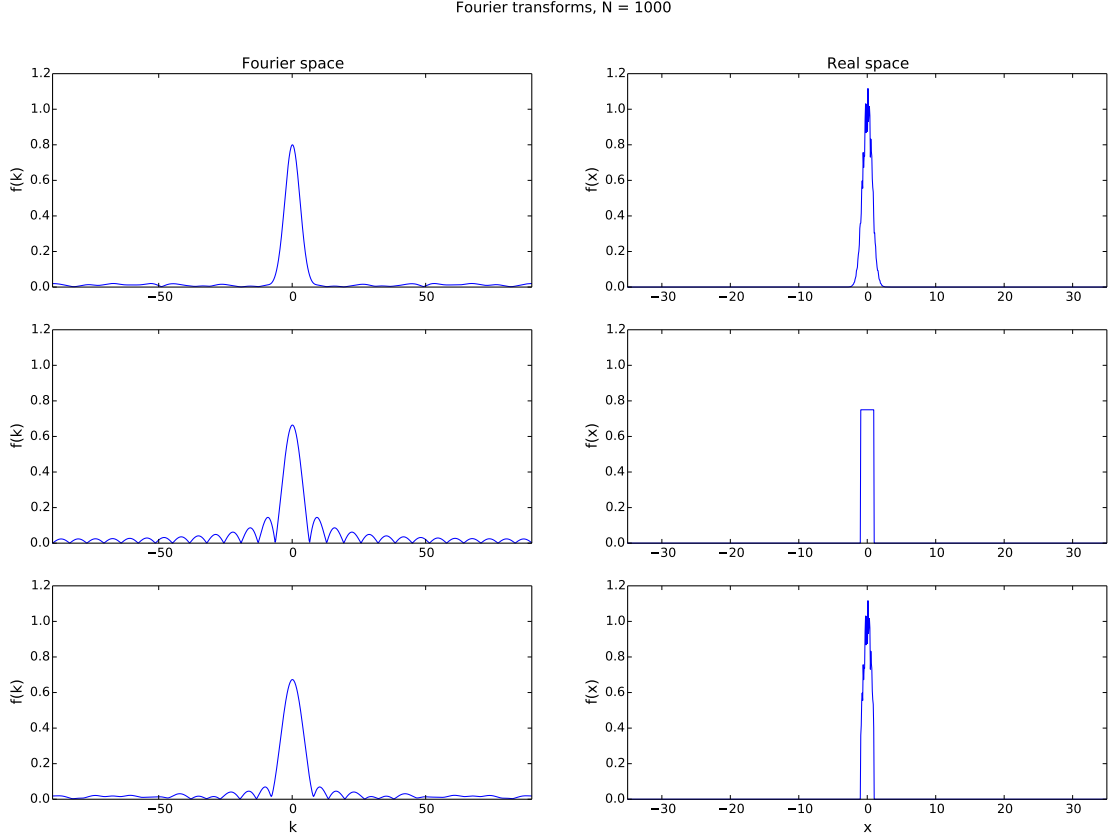


Figure 3.3: This simple simulation shows, from top to bottom, Fourier transforms of a gaussian with high spatial frequency noise, a block wave, and their product. The bottom figure shows the most accurate expectation of the transverse intensity profile before beamshaping. The Fourier transforms were calculated with the FFT-algorithm ($N = 1000$).

To choose an appropriate fit function, recall that the recorded transverse intensity profile is the Fourier transform of the transverse intensity profile at the DMD. The functions plotted in Fig.3.3 illustrate the transverse intensity profile that we expect to find, given that the gaussian input beam is noisy and overfills the DMD,.

The top figure shows that adding (high frequency) noise to a gaussian leads to symmetric fluctuations in the Fourier transform at high $|k|$. The middle figure shows that the effect of sharp edges, i.e. clipping the gaussian wings, leads to additional symmetric, high- $|k|$ components separated by nodes. The Fourier transform of a block wave is known as a sinc-squared function (see Eq.3.2). The bottom figure shows the product of both functions and its Fourier transform. Of the three figures, the bottom one shows the most accurate expectation of the transverse profile.

The simulations shown in Fig.3.3 suggest that both a gaussian and a sinc-squared function may fit the data. Indeed, both fitting functions are found to have comparably small fitting errors (see Tables 3.1 and 3.2) and were in qualitative agreement for all parameters except I_{bg} .

The following definitions are used for the gaussian

$$f(x, y) = I_{\text{peak}}(y) \exp(-(x - \mu(y))^2 / 2\sigma(y)_{\text{gauss}}^2) + I_{\text{bg}}(y), \quad (3.1)$$

and sinc-squared function

$$f(x, y) = I_{\text{peak}}(y) \left(\frac{\sin((x - \mu(y))/\sigma(y)_{\text{sinc}})}{(x - \mu(y))/\sigma(y)_{\text{sinc}}} \right)^2 + I_{\text{bg}}(y). \quad (3.2)$$

Here x is the transverse position, i.e. the column index of the CCD, y is the longitudinal position, i.e. the row index of the CCD, and $f(x, y)$ is the fit function. For both fit functions, four fit parameters are used: I_{peak} is the maximum intensity, μ is the mean position of the central maximum, σ determines the width of the central maximum and I_{bg} is the background intensity. Every row of the CCD is fitted separately. To be able to compare the widths found by both fitting functions, we relate σ to the full width half maximum (FWHM). For the definitions given above, $\text{FWHM}_{\text{sinc}} = 2.718 \times \sigma_{\text{sinc}}$ whereas $\text{FWHM}_{\text{gauss}} = 2 \times \sqrt{2 \times \ln 2} \times \sigma_{\text{gauss}} = 2.355 \times \sigma_{\text{gauss}}$.

Some debris was left on the CCD-array when the protective glass covers were removed. Since the linefocus is very narrow (~ 4 pixels wide) the debris' shadows disturbed the measured properties of the linefocus, especially I_{peak} and its variance. We solved this problem by applying a data-mask, i.e. by excluding data-points from the analysis using a pre-specified criterion. This mask is constructed by illuminating the CCD with white light and dividing the resulting image by a 2D gaussian fit of its intensity. All pixels below a threshold value of 0.85 do not follow the intensity profile of the total image and are masked. In our case this amounted to 0.68% of all pixels. If any pixel in row y' within the region of interest was masked, row y' was entirely discarded from the fitting results. Since the region within which we fit is but 40 px wide, only $\sim 3.5\%$ of rows have to be discarded. No masks were employed in the beamshaping procedure itself, only in the analysis.

Although our target variable is I_{peak} , the other fit parameters give important insights into the effects that the DMD has on the beam. Therefore, the results for all four gaussian fit parameters are shown before and after shaping in Figs.3.4 - 3.9 as a function of longitudinal position. These data were taken 14 seconds apart during which time the kinoform on the DMD was adjusted. Positions are shown in micrometers with the origin chosen at the center of the region of interest. A summary of the means and standard deviations of the parameters are listed for both fit functions in tables 3.1 and 3.2. The

parameters reported in these tables were calculated using only the data points within the vertical dashed lines, to negate edge effects. The error bars in these figures are the standard least-square fitting errors as reported by the odr fitting package⁶. For all data reported in Sec.3.3, an 18 ms camera shutter time was used.

3.3.1 Results of intensity fits

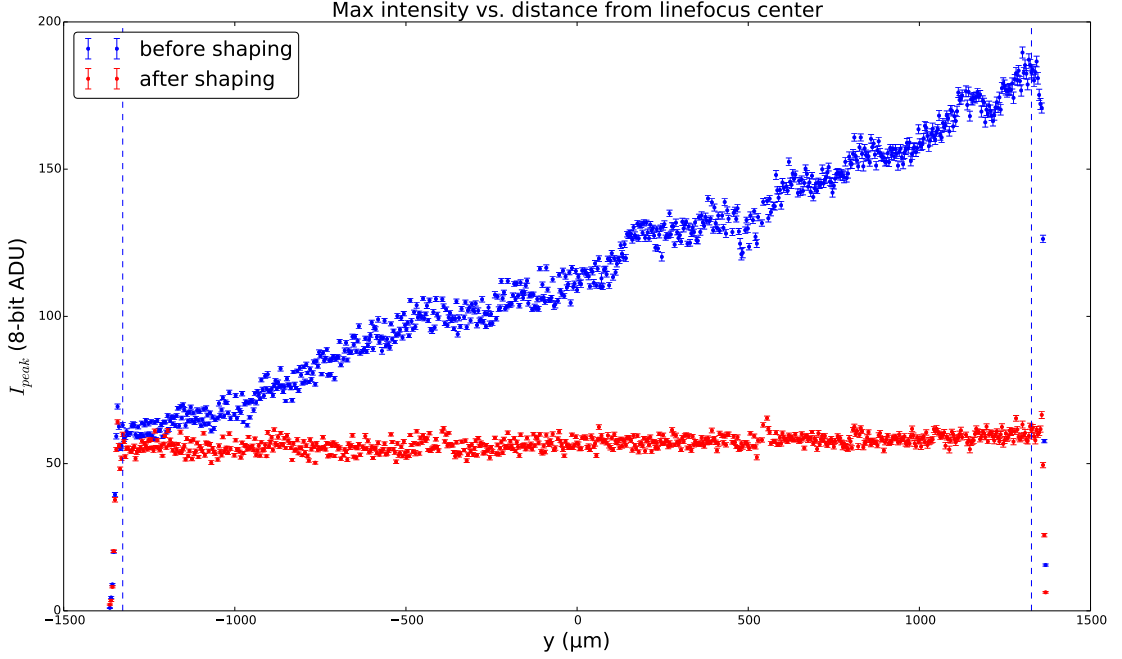


Figure 3.4: In blue are the gaussian fit values of the peak intensity when all mirrors are turned on, red when the beamshaping kinoform is displayed. From this figure one may calculate that 49% of the power in the used diffraction order is discarded to create this flattop. See Table 3.1 for further details.

Fig.3.4 shows that the longitudinal intensity profile is successfully flattened. All mirrors outside the region of interest are turned off and the target intensity is 55 ADU. This shaped flattop has rms error = 4.2%. The average rms fitting error is lower, namely 1.2%, indicating that there may be room for improvement of the flatness. We will investigate in sections 3.4 and 3.5 what causes the residual variance in the shaped flattop. To create this flattop, 49% of the power in the used diffraction order is discarded.

⁶These fitting errors are the output of `scipy.odr.run().sd.beta`

3.3.2 Results of FWHM fits

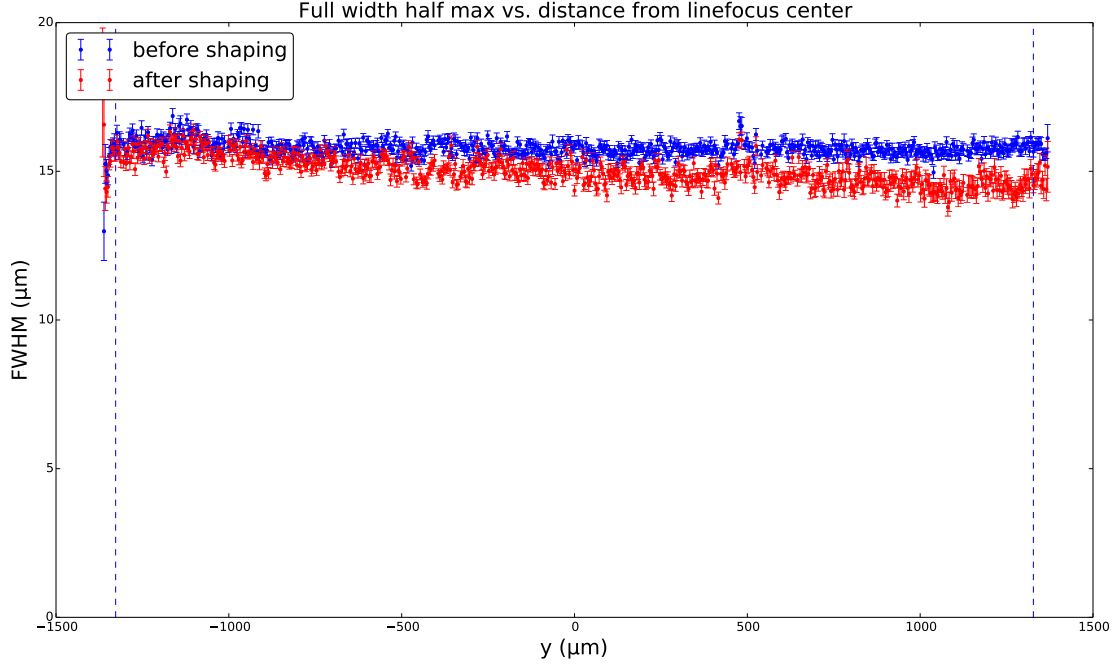
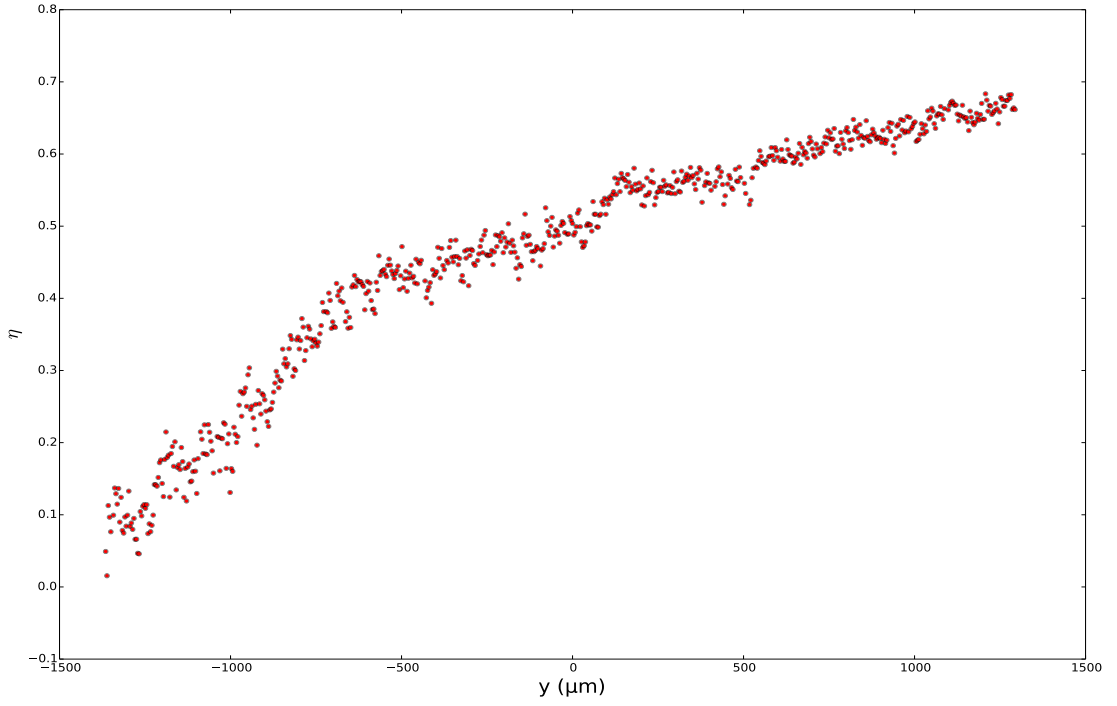


Figure 3.5: Full width half maximum fit values for the gaussian fits. See Table 3.1 for further details.

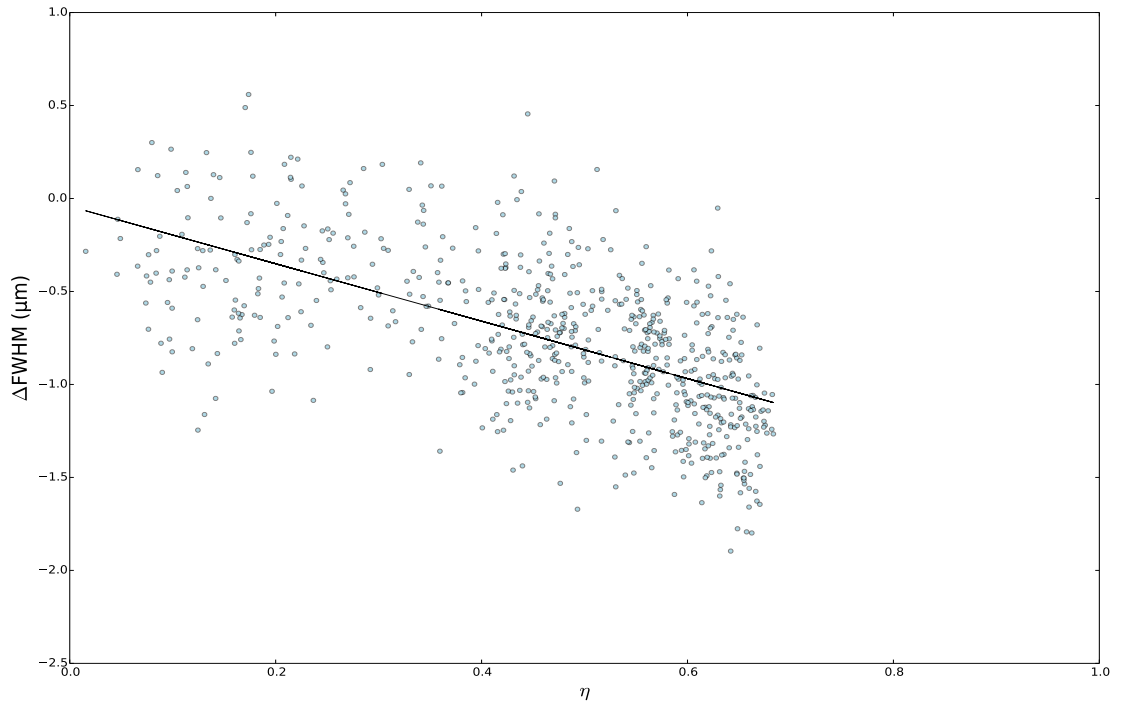
Fig.3.5 shows that the width of the unshaped linefocus is uniform to a small rms-error of 1.6%, indicating that the image plane of the DMD is properly parallel to the CCD-array. The average width of the linefocus prior to beamshaping was $15.8 \mu\text{m}$ - for comparison, the diffraction limit for a 1-inch lens with $f = 0.15 \text{ m}$ is about $4.6 \mu\text{m}$.

It is interesting that the width decreases noticeably after beamshaping, especially toward the right of the figure. To investigate whether this effect is in fact due to the beamshaping itself, we plot it against the shaping strength $\eta(y) = (I_{\text{peak,unshaped}}(y) - I_{\text{peak,shaped}}(y)) / I_{\text{peak,unshaped}}(y)$. The parameter η takes values between zero (no mirrors switched off) and one (all mirrors switched off). Fig.3.6a shows $\eta(y)$ for the kinoform displayed in this section. Due to the roughly linear intensity profile prior to beamshaping, the shaping strength correlates almost linearly with position.

Fig.3.6b shows the difference of the data in Fig.3.5 (i.e. $\text{FWHM}_{\text{shaped}}(y) - \text{FWHM}_{\text{unshaped}}(y)$) plotted against $\eta(y)$. The linear fit in this figure shows that the width of the linefocus decreases linearly (to a good approximation) with shaping strength, so we conclude that turning off mirrors in a DMD column makes the linefocus narrower in the corresponding camera rows. The same behavior is found for the sinc-squared fits.



(a) Shaping strength η as a function of longitudinal position y . See text for definitions. The apparent existence of two linear regimes remains unexplained.



(b) $\text{FWHM}_{\text{shaped}} - \text{FWHM}_{\text{unshaped}}$ is shown as a function of η . A linear fit of the form $a\eta + b$ is shown as well. We found $a = -1.54 \pm 0.08$, $b = -0.04 \pm 0.04$. This figure shows that the decrease of the width of the linefocus after shaping, observed in Fig.3.5, is indeed due to the beamshaping itself.

Figure 3.6

3.3.3 Results of mean position fits

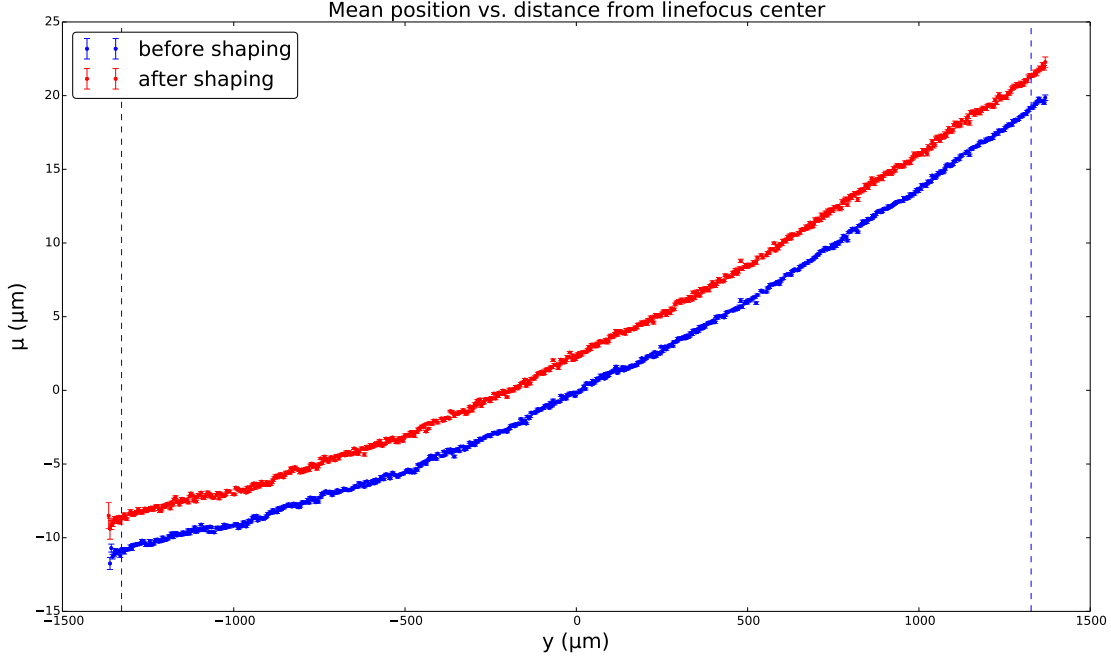
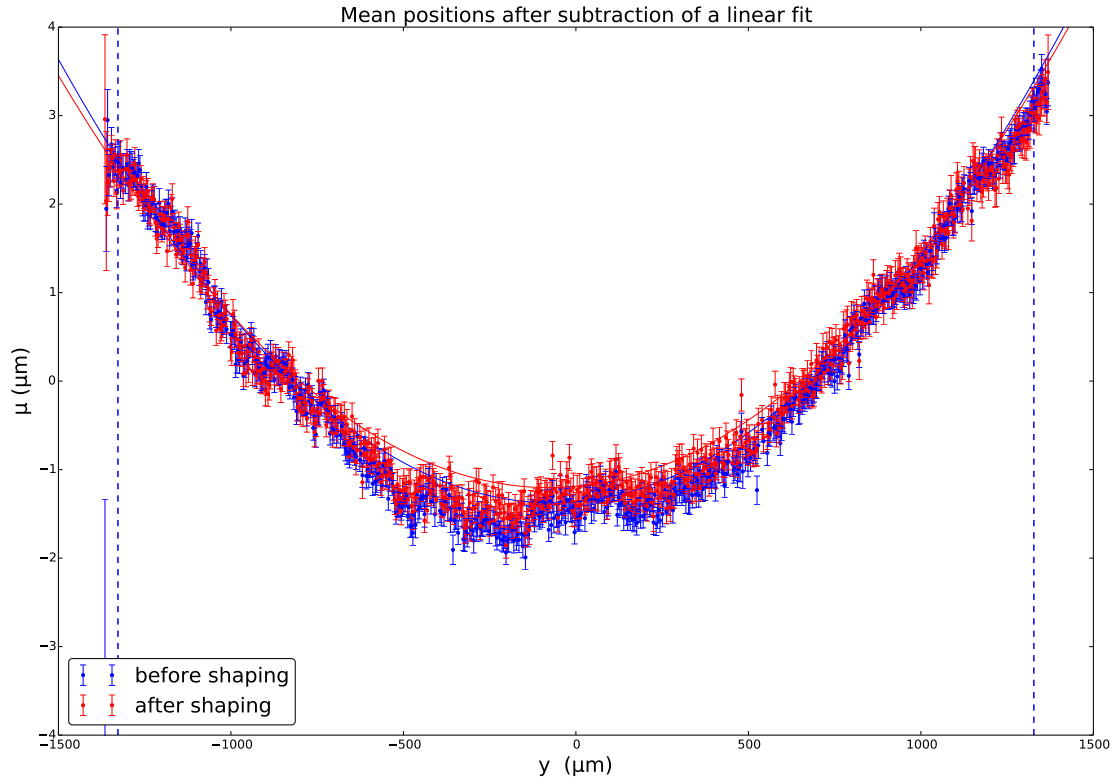


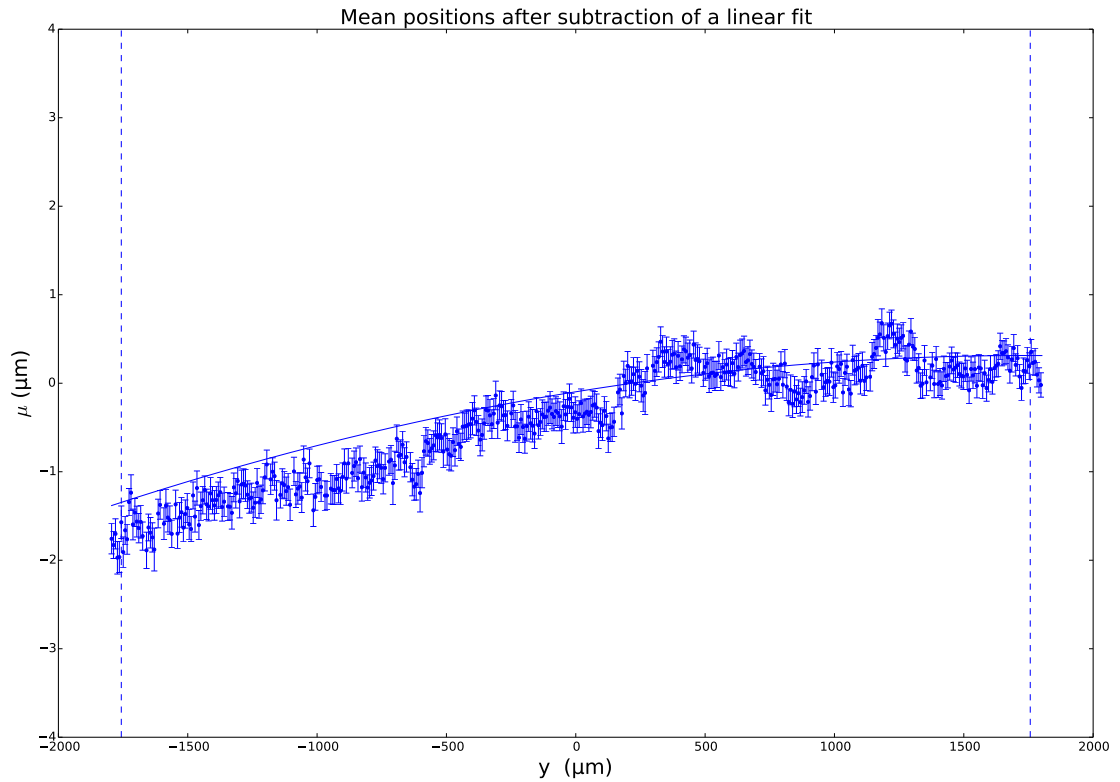
Figure 3.7: The gaussian-fitted transverse mean position of the peak intensity as a function of the longitudinal position. See Table 3.1 for further details.

Fig.3.7 shows μ , the mean transverse position of the linefocus, as a function of y . The linear slope of these data is the result of a difference in orientation ($0.636^\circ \pm 0.006^\circ$) between the DMD and the camera. The constant offset between the DMD before and after beamshaping is the result of time variation of the mean of μ . The curvature of μ is isolated in Fig.3.8a, where a linear fit to $\mu(y)$ has been subtracted. It is a notable effect because it increases when additional lenses are placed between the DMD and the target plane - it must be accounted for when designing more complicated setups involving lasers and the DMD.

In Fig.3.8b, the DMD is replaced by a mirror that had the same outline as the DMDs mirror array (to within 1 mm) and the same analysis as in Fig.3.8a is performed. Comparing Figs.3.8a and 3.8b we see that the curvature is actually due to the DMD, since the quadratic fitted curvature of $\mu(y)$ is an order of magnitude lower for the mirror ($-1.3 \times 10^{-7} \pm 0.3 \times 10^{-7} \mu m^{-1}$) than for the DMD ($2.5 \times 10^{-6} \pm 0.1 \times 10^{-6} \mu m^{-1}$). We therefore speculate that the curvature of μ is caused by a physical curvature of the DMD surface.



(a) Mean positions after subtracting a linear fit from the data in Fig.3.7. The error bars are the sum of the error bars in Fig.3.7 and the fitting error on the constant offset of the linear fit. The slope of both data sets was 0.0111 ± 0.0001 , making the inclination of the linefocus $0.636^\circ \pm 0.006^\circ$ w.r.t. the CCD array. A quadratic fit to this figure showed that the curvature of both linefoci was also identical and equal to $2.5 * 10^{-6} \pm 0.1 * 10^{-6} \mu m^{-1}$.



(b) Mean positions after subtracting a linear fit from the position data when the DMD is replaced by a mirror with an aperture. To obtain this figure an identical analysis was performed as for Fig.3.8a. Here, the slope of both data sets was 0.00934 ± 0.00009 . So the inclination of this linefocus was $0.535^\circ \pm 0.005^\circ$. A quadratic fit to this figure shows that the curvature of the linefoci was $-1.3 * 10^{-7} \pm 0.3 * 10^{-7} \mu m^{-1}$, opposite in sign and about twenty times smaller than the curvature of the mean position in the presence of the DMD.

Figure 3.8

3.3.4 Background fits

The most important thing to notice in Fig.3.9, which shows the (gaussian) fitted values for I_{bg} , is that I_{bg} was small. We have an excellent signal to noise ratio. Toward the right side of the figure the gaussian fitting algorithm raised the background to compensate for fringes that were observed next to the linefocus. The sinc-squared function was able to fit the fringes and did not show a similar increase of the background, which should therefore be regarded as mere sfitting artefact.

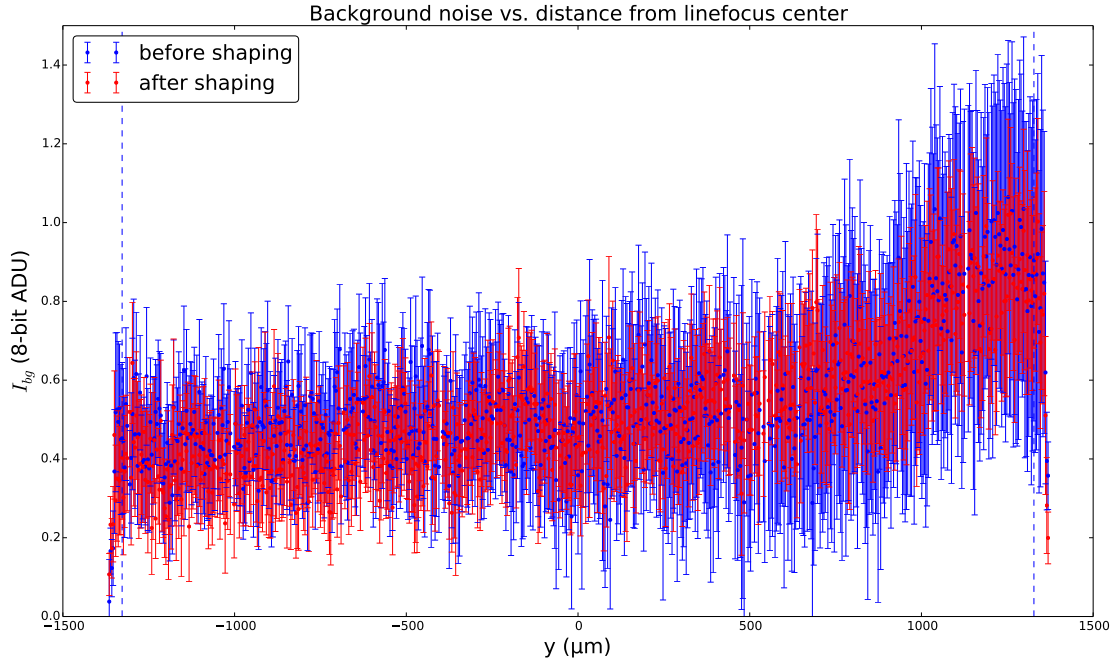


Figure 3.9: The gaussian-fitted background of the peak intensity as a function of the longitudinal position. See Table 3.1 for further details.

An overview of the averages of all fit parameters can be found in Tables 3.1 and 3.2. Comparison of the two tables shows that both fitting functions yield approximately the same results. The sinc-width is slightly larger and the sinc-intensity somewhat lower. The sinc-squared fit is better able to fit fringes, which were most pronounced in regions of high I_{peak} . Compared to Ref. [5] we can create a homogeneous flattop over a much longer range using our hybrid mode setup. The rms-flatness is improved from 30.1% to 4.4%. However, since the standard deviation of I_{peak} after beamshaping is still three times larger than the fitting error, there is room for improvement of the flatness.

Parameter	Before beamshaping	After beamshaping
Intensity I_{peak} (ADU)	$116 \pm 35 \pm 1.0$	$57 \pm 2.5 \pm 0.7$
FWHM (μm)	$15.8 \pm 0.3 \pm 0.17$	$15.0 \pm 0.5 \pm 0.22$
Mean position μ (μm)	$1.27 \pm 8.88 \pm 0.070$	$3.64 \pm 8.89 \pm 0.09$
Background I_{bg} (ADU)	$0.5 \pm 0.2 \pm 0.24$	$0.5 \pm 0.2 \pm 0.16$

Table 3.1: Average values of the gaussian fit parameters. Numbers are calculated for the data between the vertical lines in Figs.3.4 - 3.9. The unit of intensity and background is 8-bit ADU. The first number indicates the average of the fit parameter, the second its (spatial) standard deviation and the third its average fitting error.

Parameter	Before beamshaping	After beamshaping
Intensity I_{peak} (ADU)	$114 \pm 34 \pm 1.0$	$56 \pm 2.4 \pm 0.6$
FWHM (μm)	$16.5 \pm 0.2 \pm 0.15$	$15.7 \pm 0.4 \pm 0.16$
Mean position μ (μm)	$1.25 \pm 8.87 \pm 0.070$	$3.63 \pm 8.87 \pm 0.080$
Background I_{bg} (ADU)	$-0.2 \pm 0.2 \pm 0.24$	$0.3 \pm 0.1 \pm 0.14$

Table 3.2: Average values of the sinc-squared fit parameters. Numbers are, again, calculated for the data between the vertical lines in Figs.3.4 - 3.9. The unit of intensity and background is 8-bit ADU. The first number indicates the average of the fit parameter, the second its (spatial) standard deviation and the third its average fitting error.

3.4 Time variation of the linefocus

The shaped linefocus reported in 3.3 is only flat to within a few percent, mostly because of noise components with high spatial frequency. Because we have a thousand degrees of freedom to shape a segment of the linefocus ~ 2 camera pixels wide, one would expect higher accuracy. However, if there is significant time fluctuation of $S(x, y)$ during the fourteen seconds that elapse between the recording of the reference and the beamshaped image, the generated kinoform does not correctly shape the field that is present when the kinoform is displayed. To determine whether the linefocus can be made flatter by speeding up the shaping procedure, we investigate its time variation.

Time variation may occur on short or long timescales compared to the integration time of the camera. With four runs of fifty images we characterize the linefocus under different circumstances: shaped or unshaped and with 18 ms or 78 ms camera integration time. The magnitude of time variation is quantified by the standard deviation of these data sets. Recording fifty images over twenty seconds will expose any relevant slow drift in the signal. A random waiting time $0s < t_{\text{wait}} < 1s$ is inserted between each shot. When increasing the shutter time, ND-filters must be added to avoid camera saturation.

For each shot we performed the same transverse gaussian fits as in Sec.3.3, so that we obtain the fit parameters as a function of space (y) and time (t). The fitting errors in each run were comparable to those reported in Table 3.1.

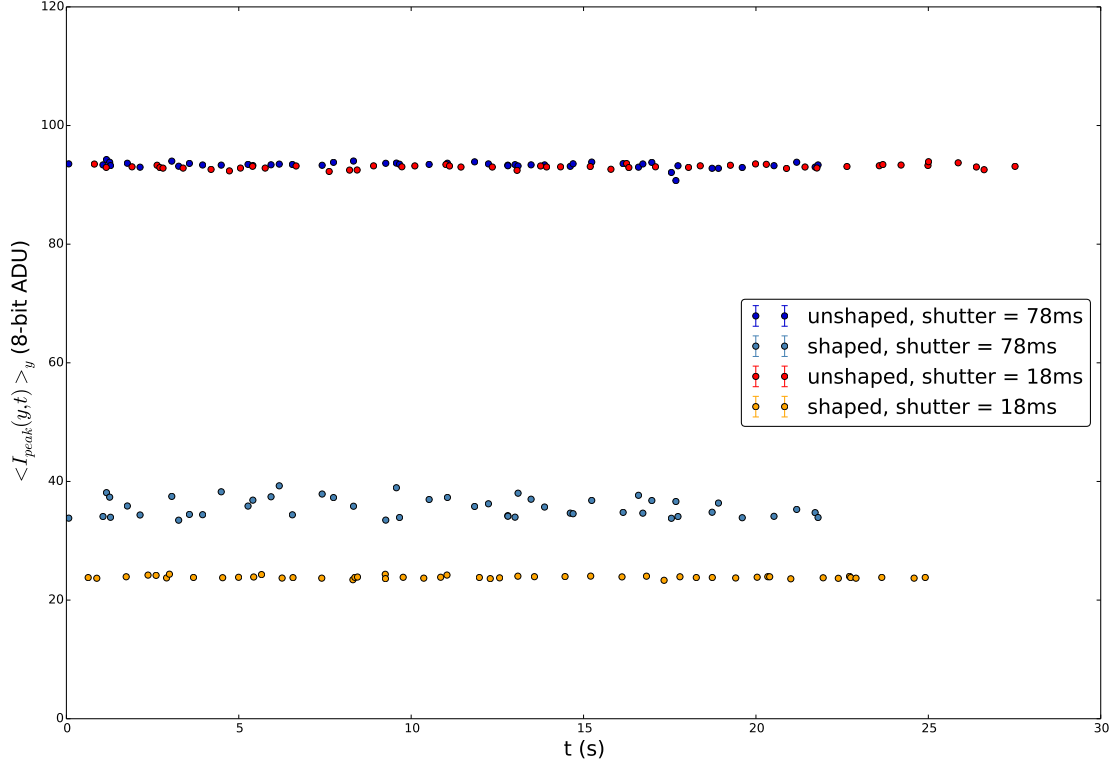


Figure 3.10: Each data point represents the peak intensity of one image averaged over the entire length of the linefocus (820 pixel rows). The average intensities fluctuate strongly over time only for shaped images and only for certain integration times (shutter times). See Table 3.3, first row, for the standard deviations of these distributions. The error bars are smaller than the points representing the data.

Fig.3.10 shows the average over y of $I_{\text{peak}}(y, t)$ as a function of time. The time variation of the unshaped linefoci is in the order of only a few percent and is similar for both shutter times (see also the top row of Table 3.3). The time variation of the shaped linefoci, however, is eight times larger when recorded with a 78 ms shutter time compared to an 18 ms shutter time - it appears that the beamshaping procedure introduces time variation. Note that since the time variations in Fig.3.10 remain even after spatial averaging, they must be in phase over wide regions of the linefocus. If the time variation were due to noise, it should be averaged out for longer camera integration times. However, the *shortest* integration time gives the most *constant* signal, which shows that the time variation is not random. In contrast to random noise, periodic signals will appear constant if the camera integration time is an integer multiple of their period, but will fluctuate when a different integration time is chosen. Therefore $\langle I_{\text{peak}}(y, t) \rangle_y$ must fluctuate periodically with a period (in ms) that is approximately a divisor of 18 but not of 78. This finding is confirmed with photodiode measurements in Sec.5.3.

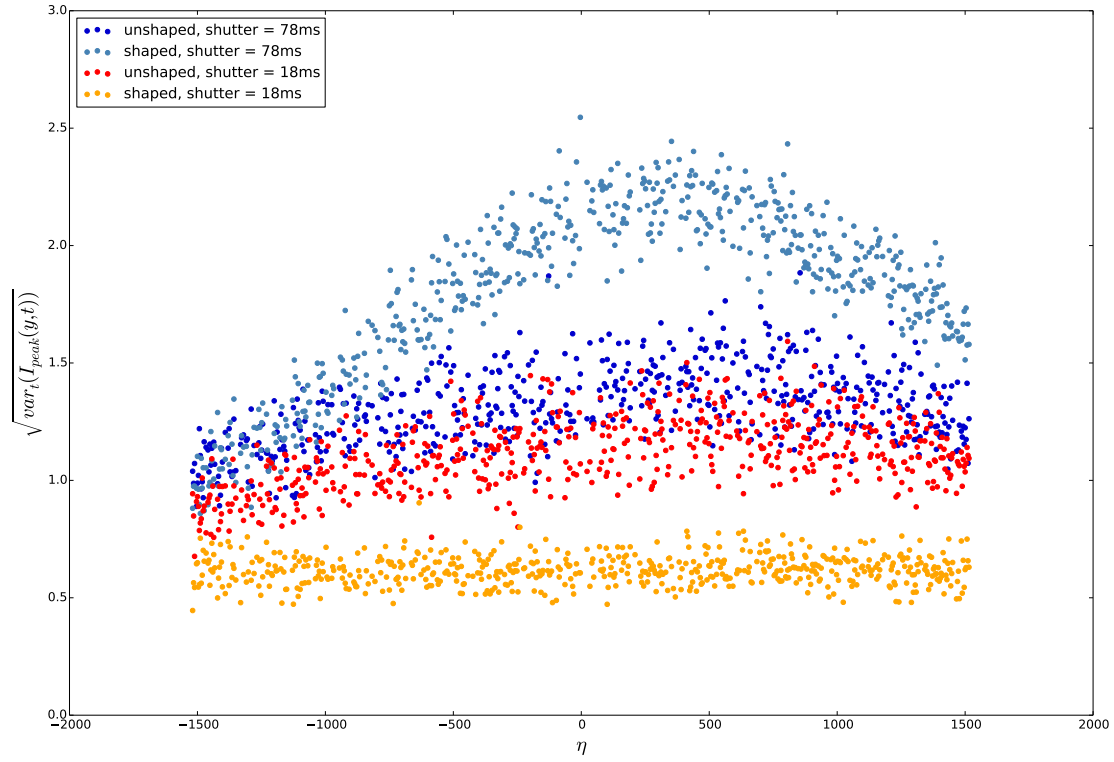
Parameter	Before beamshaping		After beamshaping			
	18ms	78ms	18ms	78ms	not shuffled	shuffled
$\sqrt{\text{var}_t(\langle I_{\text{peak}}(y, t) \rangle_y)}$ Time variation of average intensity	0.3425	0.5219	0.2059	1.613	0.5427	0.4077
$\langle \sqrt{\text{var}_t(I_{\text{peak}}(y, t))} \rangle_y$ Average time variation per row	1.144	1.349	0.6208	1.945	1.073	1.021
$\langle \langle I_{\text{peak}}(y, t) \rangle_y \rangle_t$ Intensity averaged over time and space	93.04	93.36	23.85	35.67	50.47	49.91
$\langle \sqrt{\text{var}_y(I_{\text{peak}}(y, t))} \rangle_t$ Flatness averaged over time	16.96	15.89	1.185	3.103	3.949	3.961

Table 3.3: The quantities in this table are chosen to characterize the stability of the linefocus. All values are in 8-bit ADU. Fifty consecutive shots represent the time dimension. The region of interest spans 820×40 camera rows, representing the space dimension. The interpretation of the first and second row is discussed in the text. The ratio of the fourth and third rows gives the time average of the rms-flatness of the linefoci. The two rightmost columns show the data from Section 3.5, which is recorded with an 18 ms integration time.

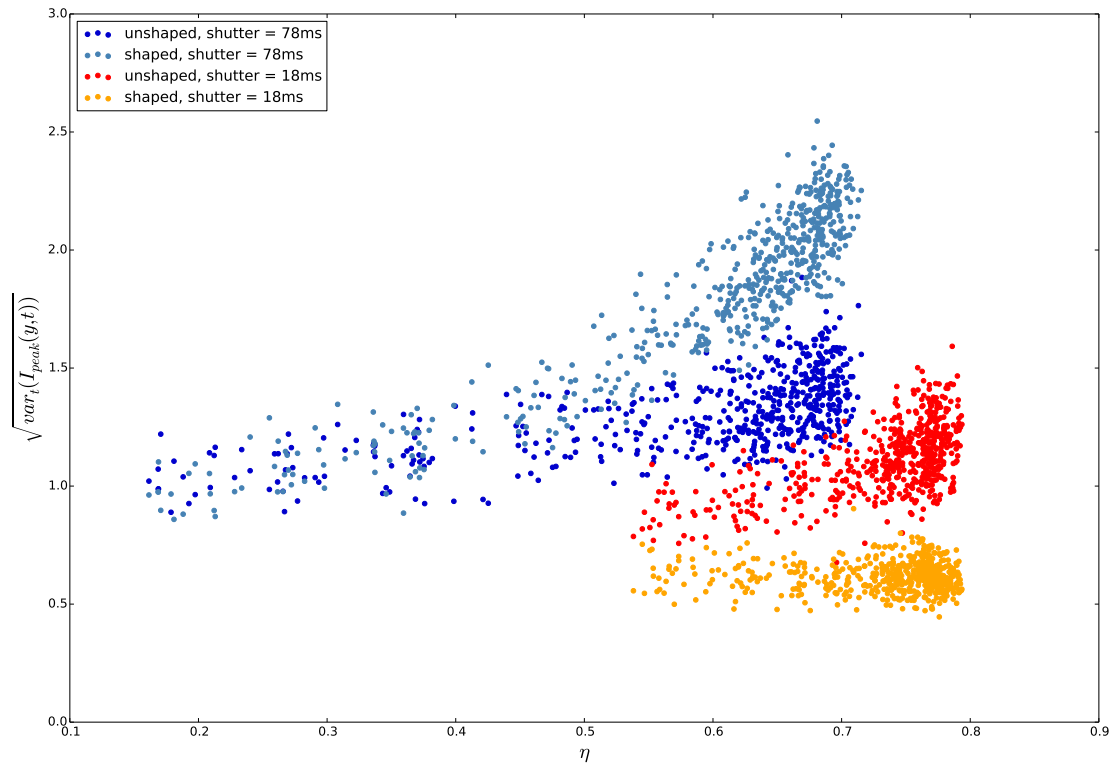
Fig.3.11a plots the time variation per row ($\sqrt{\text{var}_t(I_{\text{peak}}(y, t))}$) as a function of y , showing which rows of each linefocus are responsible for the time variation of the mean shown in Fig.3.10 (corresponding to the second row of Table 3.3). We see maxima in time variation around $y \sim 400 \mu\text{m}$ for all linefoci except the shaped 18 ms one, indicating that not rows in that vicinity fluctuate more strongly. Fig.3.11b shows that the beamshaping procedure itself causes the time variation, since $\sqrt{\text{var}_t(I_{\text{peak}}(y, t))}$ correlates η , most strongly so for the 78 ms case.

In summary, from the figures in this section we draw the conclusion that there is time variation, which is caused by the beamshaping itself and dominated by a periodic contribution, and that the shutter time of the camera may be adjusted to compensate for the effect.

These findings are confirmed by further investigations in section 5.3. The average time variation of $I_{\text{peak}}(y)$, for a well-adjusted shutter time, is equal to 0.62ADU. Since this is on the same order as the average fitting error of I_{peak} in the previous section (which was 0.6ADU), we may conclude that the time variation can be suppressed sufficiently to give a dependable reference for calculating a shaped kinoform and does not limit the achievable flatness. However, we hereafter keep in mind that all reported linefocus data are integrations over an integer number of periods of a periodic signal.



(a) The time variation ($\sqrt{\text{var}_t(I_{\text{peak}}(y, t))}$) is plotted as a function of longitudinal position y . The data used is the same as in Fig.3.10. The behavior of the shaped linefocus recorded with 78 ms is anomalous.



(b) For each row the standard deviation over time is plotted against shaping strength, the data are the same as in Fig.3.10. The time variation of the beamshaped signal significantly increases with shaping strength if the integration time is 78 ms, but does not change if the integration time is 18 ms.

Figure 3.11

3.5 Shuffling

When determining beamshaping kinoforms, we have not accounted for the quasi-gaussian transverse intensity profile at the DMD. Ideally, each DMD pixel would be weighed for the local intensity when calculating the kinoform. This information, however, is not directly accessible in the hybrid mode so the probability to be switched off was simply made equal for each pixel. In addition to the transverse variation in intensity, light originating from different DMD-pixels also arrives to the image plane with a different phase. This might affect the linefocus in ways that are not immediately obvious.

Light fields can be simulated to figure out the effect of the placement of off-pixels, but a quick experiment suffices to determine whether the particular random pattern of off-pixels influences the achievable flatness. To that end, we shuffled the pixels, meaning that the distribution of off-pixels was re-randomized separately for each row, while keeping the total $N_{\text{off}}(y)$ constant.

We perform two runs of 50 images, with random time intervals interjected, using an 18 ms shutter time to minimize time variation. In one run, the kinoform is shuffled between each image, in the other run only one kinoform is displayed. The results are shown in Fig.3.12 and Table 3.3. The figure shows that $I_{\text{peak}}(y, t)$ does not fluctuate more in the shuffled run than can be explained by the time variation. No significant differences between the 'shuffled' and 'not shuffled' runs were found for the other three fit parameters either. Since all 50 random distributions of the off pixels appear to be equivalent, we may conclude that the flatness of the linefocus can not be improved by shuffling.

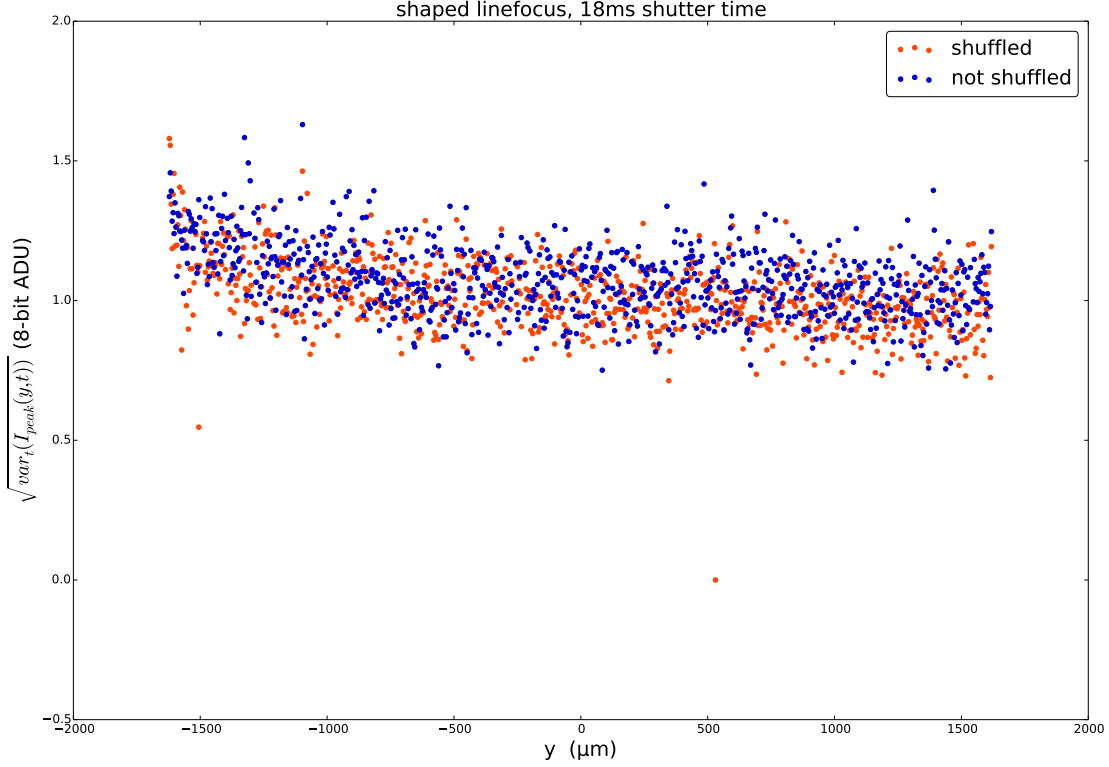


Figure 3.12: Each data point represents the standard deviation of I_{peak} in one row over 50 shots. In the shuffled run, a new kinoform is generated between each shot. For numbers characterizing the linefoci, see Table 3.3.

3.6 Conclusion

We have improved the rms-flatness of a linefocus from $34.87/115.84 = 30\%$ to $2.46/56.94 = 4.3\%$ over a length of 3 mm in the target plane, without strongly affecting its width or mean position. To achieve this, 49% of the power within the region of interest is shaped away. Our beamshaping procedure causes a periodic variation of the intensity over time, but this effect can be integrated out by choosing a camera shutter time of 18 ms. This solution is sufficient to shape a CW-laser, but the time variation will need to be understood and counteracted if the DMD is applied to shape femtosecond pulses. The minimum measured time variations of a beamshaped linefocus are $0.628/23.85 = 2.6\%$, and $1.073/50.47 = 2.1\%$. The shuffling experiment shows that it does not matter where pixels in a DMD column are turned off, as long as their distribution is random and the right number are turned off. If a linefocus of this quality can also be created using a femtosecond pulse laser and a microscope objective, it would be sufficient for our purposes.

4 Beamshaping broad spectrum light

In the previous chapter we have described a simple method and setup that can produce a satisfactory flattop using CW-light from an infrared laser diode. Before refining the beamshaping method, we need to see whether our method is applicable to (ultrashort) pulses.

The defining property of a pulse is that its intensity $I(\mathbf{x}, t)$ is time-dependent even when an optical cycle is averaged out. Since $I(\mathbf{x}, t)$ and its spectrum $I(\mathbf{x}, \omega(\lambda))$ are related by Fourier transformation, pulses must have broader spectra than CW fields - since the latter transform to the δ -function in frequency space. For a pulse with gaussian temporal profile of 100 fs duration and a center wavelength of 800 nm this relation dictates that it has a minimum spectral width of 18.6 nm⁷. Such a broad spectrum is a potential problem because the DMD operates as a diffraction grating, meaning that the diffraction angle of its orders is sensitive to wavelength (see Eq.4.1, the grating equation). In the Fourier (back focal) plane of the DMD, the variation of diffraction angle turns into a variation in position, which complicates experiments with beamshaped pulses. The grating equation can be used to calculate that, for our optical system (see Fig.3.1), a spectral shift $\Delta\lambda$ of 20 nm leads to a position shift Δx of about 1.7 mm in the back focal plane - over a hundred times the width of the linefocus found in the previous chapter. Clearly, broad spectra are a fundamental property of short pulses that may interfere with our beamshaping scheme.

To investigate the effect of a pulse's broad spectrum on our beamshaping method more precisely, we use a model system to isolate it from the effect of other differences between pulse- and CW-lasers. Our model system is a subthreshold CW laser diode with a linewidth of about 16.6 nm. Besides practical advantages, this model system offers the benefit that CW-light averages over vibrations of the DMD. It is important to keep in mind, though, that the results in this chapter were not obtained with an actual 100 fs pulse laser, but with a CW-laser of a similar spectral width.

In Section 4.1, the spectrum of the laser diode is characterized as a function of the applied current. In Section 4.2 we look at the spatial dispersion of the linefocus caused by the broad spectrum in both the transverse and longitudinal direction. In Section 4.3 we report succesful beamshaping of broad spectrum light with a DMD. In Section 4.4 we shed more light on the differences that are to be expected between linefoci created with CW and pulsed light. We will find that the orientation of the cylindrical lens in our beamshaping setup can compensate for the dispersion of the focus caused by the broad spectrum.

⁷From Fourier transformation: $\sigma_t^{-1} = 2\pi\sigma_f$. Error propagation formula: $\sigma_\lambda = \sigma_f |\partial\lambda/\partial f|$ with $c = \lambda f$ yields $\sigma_\lambda = \sigma_t^{-1} \lambda^2 / c$.

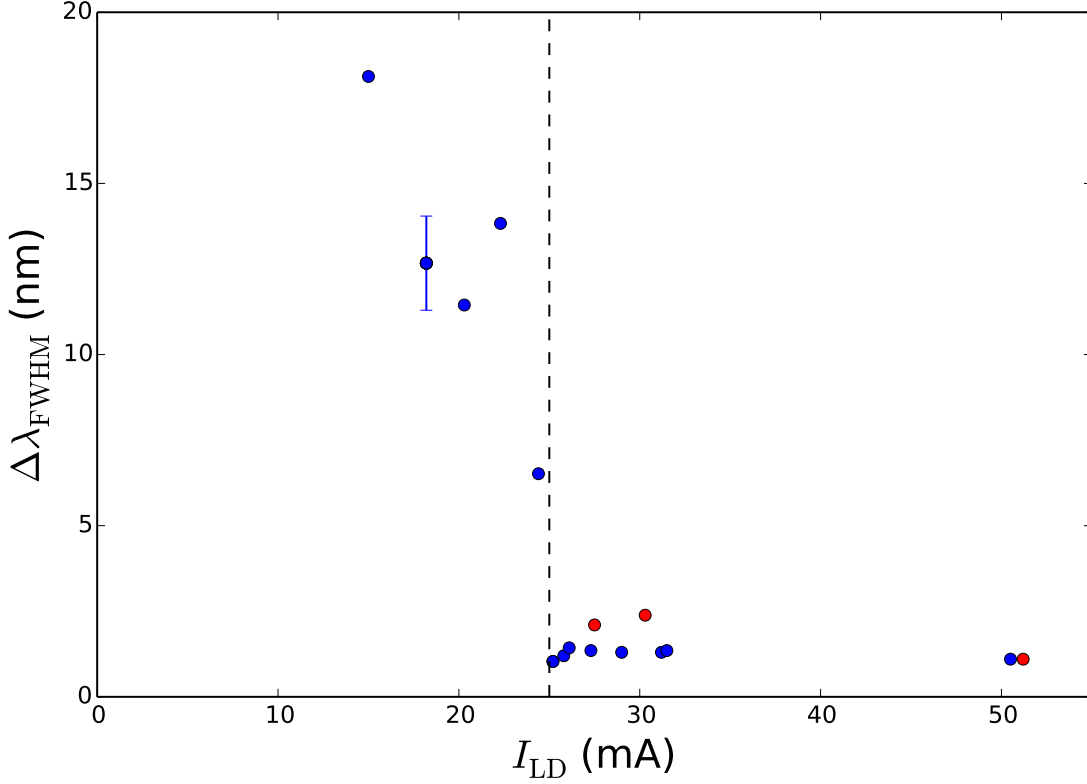


Figure 4.1: This figure shows the full width half maximum of the spectrum of the laser diode versus applied current as obtained from spectrometer data. The vertical line indicates the lasing threshold current as reported by the manufacturer (25.0 mA). The three red data points indicate currents at which multimode lasing is observed (see for examples Fig. 4.2). Five measurements taken at $I_{\text{LD}} = 18.2$ mA allow us to estimate the error of $\Delta\lambda_{\text{FWHM}}$ there.

4.1 Characterization of the laser diode

For diode lasers population inversion between the upper and lower levels of the lasing transition, which is required to induce lasing, is achieved by applying a sufficient electrical current to the diode. The applied current can therefore be used to control whether the diode emits dominantly via lasing (narrow spectrum) or other processes (broad spectrum). In this section we characterize the spectrum of the diode laser used in our model system as a function of the applied current I_{LD} , focusing on the full width half maximum $\Delta\lambda_{\text{FWHM}}$ of the laser diode spectrum. $\Delta\lambda_{\text{FWHM}}$ is determined visually from spectrometer data, after background correction. This approach works well for the narrow, peaked spectra above threshold, but introduces a sizeable error for the broad, noisy spectra below threshold. For the points at $I_{\text{LD}} = 18.2$ mA, which is the current we will use in our model system, four spectra are averaged before determining the FWHM.

Fig.4.1 shows $\Delta\lambda_{\text{FWHM}}$ as a function of I_{LD} as measured with an OceanOptics HR2000CG-

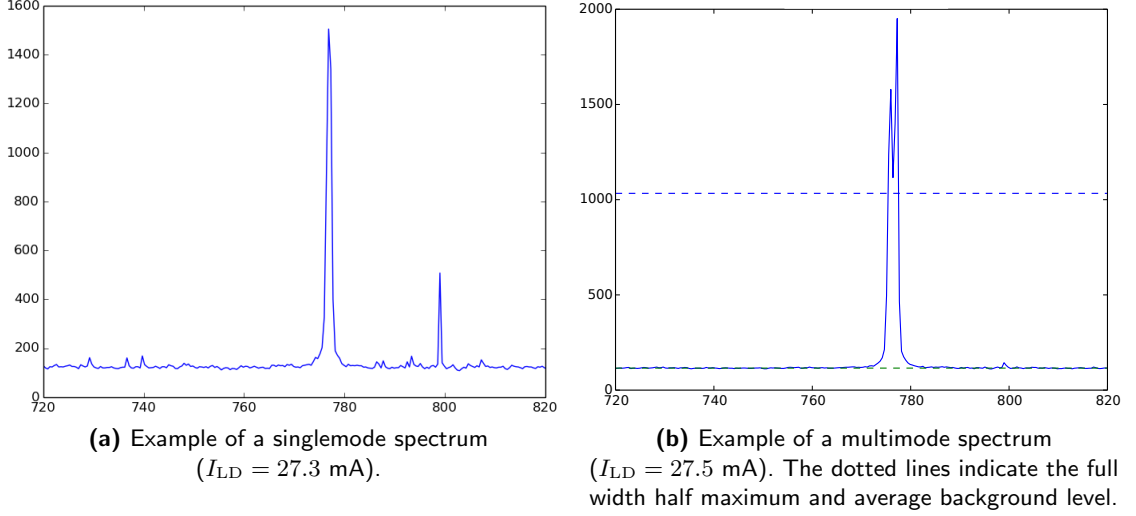


Figure 4.2: The horizontal axis shows the wavelength in nanometers. The vertical axis shows intensity in ADU of the spectrometer. In Fig. 4.2b a short integration time of $5\mu\text{s}$ is used compared Fig. 4.2a. The peak observed at 800 nm in Fig. 4.2a is due to a systematic error in the spectrometer which causes background noise accumulation for long exposure times.

UV-NIR spectrometer (with a resolution of 2.27 px/nm). Between the data points at 24.4 mA and 25.2 mA the linewidth decreases by a factor four, indicating that the lasing threshold lies between these two data points. This is consistent with the lasing threshold of 25 mA reported by the manufacturer. As expected, the output power of the laser diode increases by several orders of magnitude concurrently with the decrease in $\Delta\lambda$. Above threshold, the laser emits at a center wavelength of 776.8 ± 0.44 nm,⁸ which is also within the bounds (785 ± 10 nm) provided in the data sheet.

Above threshold, two types of spectra can be observed, namely singlemode (Fig.4.2a) and multimode (Fig.4.2b). In the multimode spectrum the diode lases in two cavity modes which have slightly different resonant frequencies leading to two peaks in the output spectrum. Obviously, multimode lasing leads to higher recorded values of $\Delta\lambda_{FWHM}$. Multimode lasing was observed at 27.5 mA, 30.3 mA and 51.2 mA, and $\Delta\lambda_{FWHM}$ is indeed larger at those currents (indicated in red in Fig.4.1). Note that the laser can jump between ordinary and multimode lasing when I_{LD} is varied by as little as 0.2 mA. Multimode spectra are not stable over time.

The relevant parameters of the model system can be calculated from the data shown in Fig.4.1. Taking all points above lasing threshold, we find an average linewidth of 1.4 ± 0.41 nm. If points at which multimode lasing occurs are removed, we find 1.26 ± 0.13 nm. Below the lasing threshold we identify $I_{LD} = 18.2$ mA as a suitable current for our model

⁸Here the error is the standard deviation of the center wavelength for $I_{LD} > 25$ mA, not to be confused with the linewidth of the laser.

system. The spectrum there is broadened by about a factor of ten to 12.8 ± 1.4 nm, which is the same order of magnitude as the spectral width of a 100 fs pulse. When we determine $\Delta\lambda_{\text{FWHM}}$ by fitting a gaussian to the spectrum at $I_{\text{LD}} = 18.2$ mA, we find a somewhat higher spectral width of $\Delta\lambda_{\text{FWHM}} = 16.6$ nm.

4.2 Dispersion due to a broad spectrum

Having described the spectrum of our model system we return to the question how broad spectra affect a linefocus and our beamshaping method.

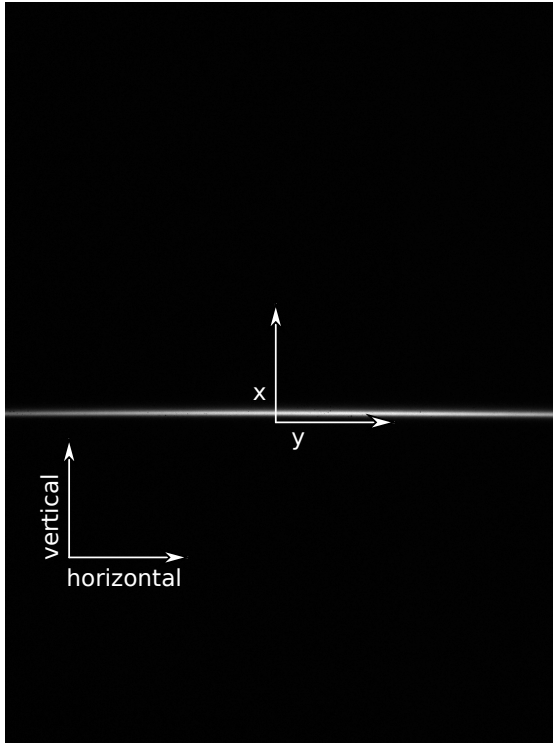
A qualitative answer to this question is given by Fig.4.3, which shows camera images of horizontal and vertical linefoci below and above lasing threshold. In all figures, the vertical direction is perpendicular to the plane of the beampath so that the diffraction of the beam by the DMD occurs in the horizontal direction. The orientation of the linefocus is changed by rotating the cylindrical lens by 90° around the optical axis (for details of the setup see Fig. 3.1).

Comparing the left- to the right-hand figures we see that, both above and below threshold, the transverse profile is broadest if the transverse direction x is horizontal (i.e. in plane with the beam path). If the input beam has a broad spectrum (Fig.4.3b), the vertical linefocus is broadened much more strongly than when the input beam has a narrow spectrum (Fig.4.3d). Comparing Figs.4.3a and 4.3c one can observe that the horizontal linefocus is relatively unaffected by spectral broadening. Clearly, the width of the linefocus is positively correlated with the spectral width of the laser, and this effect is much stronger for vertical linefoci than for horizontal linefoci.

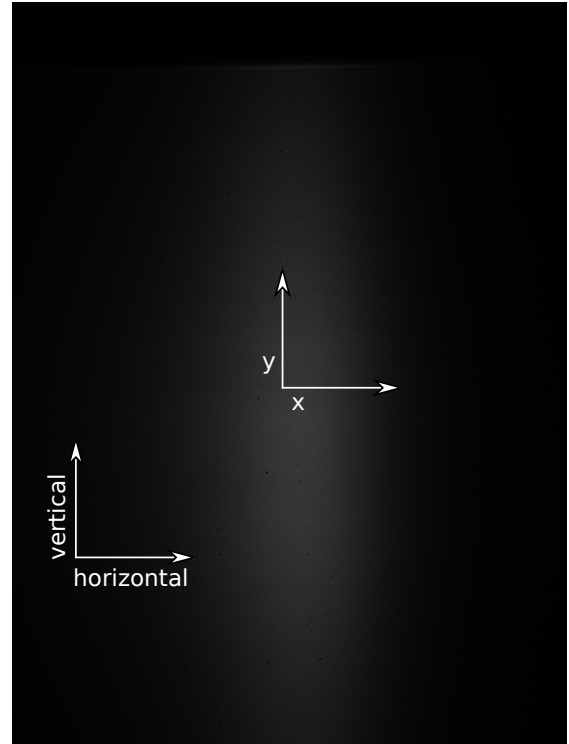
As mentioned, the explanation of these observations is found in the grating equation. Ray-tracing the path of the third diffraction order from the DMD, we find that the transverse position x (in the Fourier plane) and the spectrum λ are related by

$$x(\lambda) = l * \arctan\left(\frac{m\lambda}{d} - \sin(\theta_{\text{in}})\right). \quad (4.1)$$

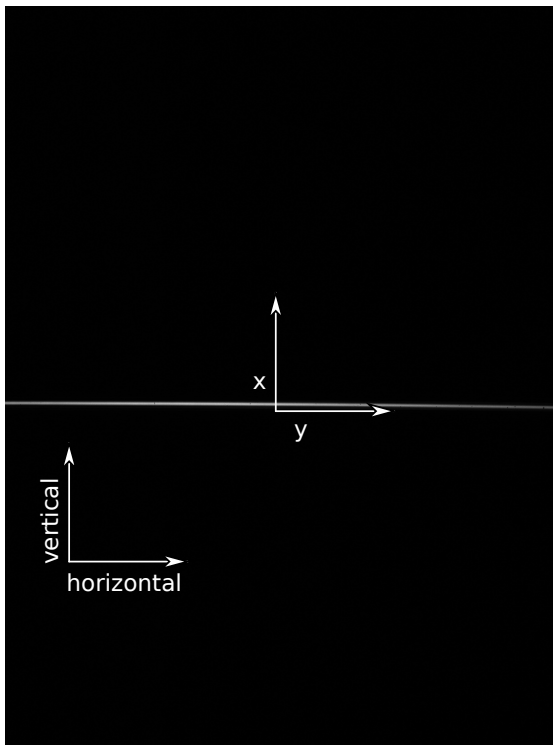
Here $l = 15$ cm is the distance to the spherical lens, $m = +3$ is the diffraction order, $d = 5.4$ μm is the grating pitch and $\theta_{\text{in}} = 24^\circ$ is the angle of incidence. For $\Delta\lambda_{\text{FWHM}} = 16.6$ nm, this equation gives a large transverse dispersion of $\Delta x = 1.4$ mm. Considering that the active area of the CCD is about 4.8×3.6 mm large, the broadening in Fig.4.3b is indeed of the expected order of magnitude. A ray-tracing analysis for the longitudinal position y shows that it is unaffected by the input spectrum - no longitudinal dispersion occurs because imaging is independent of the angle under which a ray in the object plane travels. This property of imaging systems only holds strictly in the idealized context of ray optics. In Fourier optics, any imaging system introduces a non-trivial point spread function, except when lenses of infinite radius are used. It turns out that the point-spread



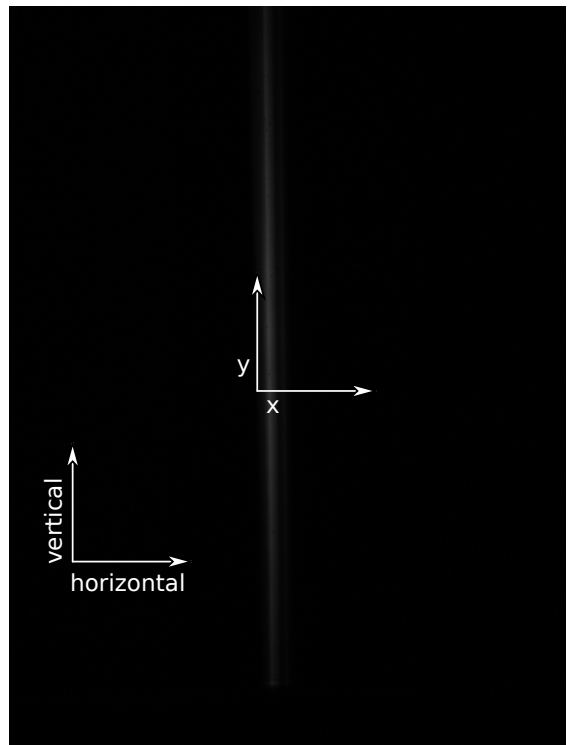
(a) Horizontal linefocus, with longitudinal dispersion.



(b) Vertical linefocus, with transverse dispersion.



(c) Horizontal linefocus, with longitudinal dispersion.



(d) Vertical linefocus, with transverse dispersion.

Figure 4.3: (a) and (b) show linefoci below lasing threshold ($I_{LD} = 18.2$ mA) for two orthogonal orientations of the cylindrical lens; (c) and (d) show linefoci above lasing threshold ($I_{LD} = 51.2$ mA). The situation studied in Section 3 is analogous to Fig.(c).

function of the imaging system determines the effect of broad spectra on longitudinal dispersion (see Sec.4.2.2).

4.2.1 Transverse dispersion

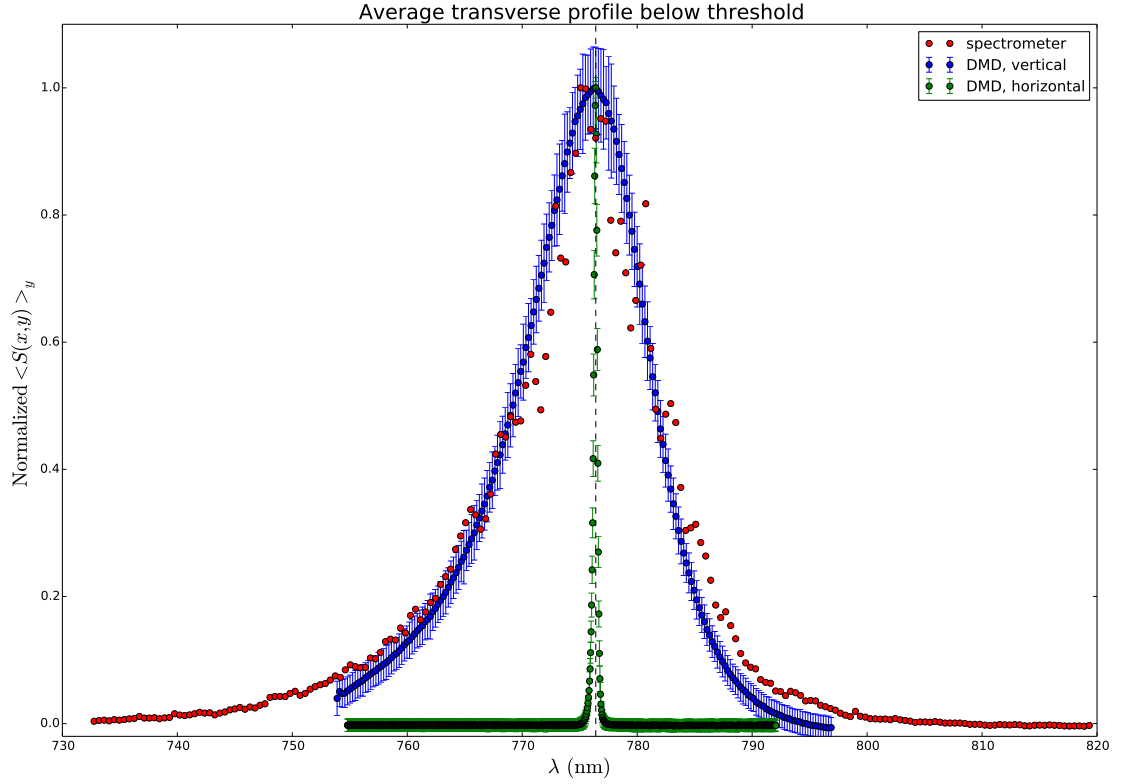
To ascertain whether spectral width indeed fully explains the transverse width observed for vertical linefoci, we describe it quantitatively in this section by averaging the transverse profile of the linefocus in the longitudinal direction (i.e. calculating $\langle S(x(\lambda), y) \rangle_y$). A simple simulation of the expected transverse profile has already been performed in the previous chapter and can be found in Fig.3.3.

Figs.4.4b and 4.4a show these average transverse profile for the horizontal and vertical linefoci above and below threshold. To facilitate comparison of the transverse profiles to the spectra measured with the spectrometer, Eq. 4.1 is used in these figures to rescale the transverse position x to λ .

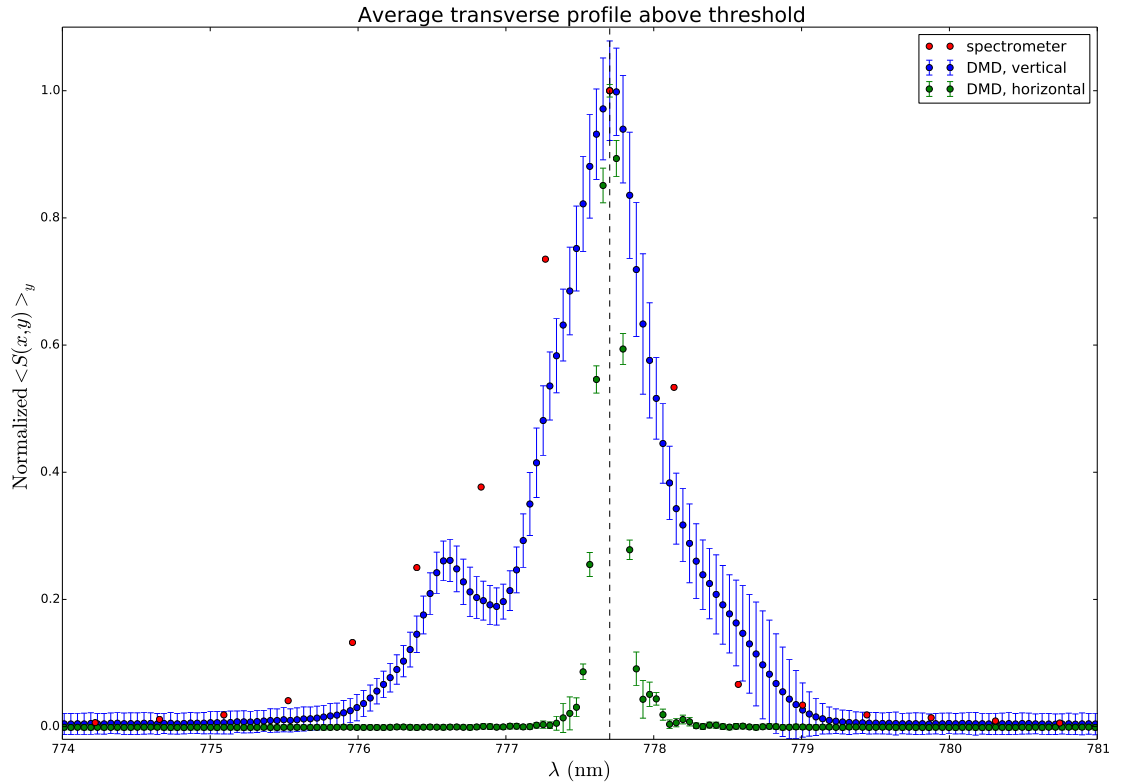
From these figures we find that the FWHM of the vertical linefocus follows the FWHM of the spectrum quite closely. Below threshold they are 14.6 nm and 16.6 nm respectively. Above threshold we find 0.92 nm and 1.27 nm respectively. The FWHM of the horizontal linefocus, on the other hand, only increases from 0.196 nm to 0.38 nm when the spectrum is broadened by a factor 10, it is clearly not very sensitive to the spectral content. Not only the widths are congruent, the overall similarity between the spectrometer data and the vertical profile is striking below threshold and even above threshold, where we push the limits of the resolution of the spectrometer, the asymmetry of the spectrometer data is reproduced in the vertical profile.

Above threshold, however, the difference between the spectrum and the vertical profile is not within the error margins. The DMD data fall short on the left hand side. Also, the average width of the linefocus below threshold is 1.193 ± 0.008 mm (see Table 4.2) which is slightly below the expected 1.31 mm. In fact, multimode lasing partially compensated for this effect in Fig. 4.4b, which can be seen when comparing the profiles in Figs.4.4a and 4.4b, recorded for singlemode spectra above threshold. So, although the transverse width of a linefocus with transverse dispersion is certainly dominated by the spectrum of the incident beam, spectral broadening is not the only effect at play.

A few notes about the analysis necessary to produce Figs.4.4b and 4.4a are in order. To account for the fact that y is not exactly parallel to the CCD grid, the transverse profile of each row/column is shifted, using interpolation, by a distance μ (the gaussian fitted mean position) before calculating the average transverse profile. In principle, shifting may broaden the profile by an amount on the order of the fitting error of μ , but since that fitting error is only $0.8 \mu\text{m}$ (see Table 4.2), corresponding to $\Delta\lambda = 0.01$ nm, broadening of the profile by fitting artefacts is negligible. Furthermore, the maxima of the DMD data are translated by -23.0 to -27.7 nm to overlap with the center wavelength of the spectrometer, since the latter is calibrated to find the correct center wavelength. Each



(a) In blue (green): the transverse profile of a vertical (horizontal) linefocus averaged over y at $I_{LD} = 18.2 \text{ mA}$, data has been shifted to match the center wavelength of the laser diode (dotted line). In red: the laser diode spectrum at the same current, measured with a spectrometer. For the blue data, only one in five points is shown to reduce cluttering. A gaussian fit to the average transverse profile yields $\Delta\lambda_{FWHM} = 16.6 \pm 0.3 \text{ nm}$ for the spectrometer data. From the average FWHM (Table 4.2) we find $\Delta\lambda_{FWHM} = 14.62 \pm 0.06 \text{ nm}$ for the vertical and $\Delta\lambda_{FWHM} = 0.38 \pm 0.010 \text{ nm}$ for the horizontal linefocus.



(b) In blue (green): the transverse profile of a vertical (horizontal) linefocus averaged over y for $I_{LD} = 51.2 \text{ mA}$, data has been shifted to match the center wavelength of the laser diode (dotted line). In red: the laser diode spectrum at the same current, measured with a spectrometer. A gaussian fit to the average transverse profile yields $\Delta\lambda_{FWHM} = 1.27 \pm 0.02 \text{ nm}$ for the spectrometer data. From the average FWHM (Table 4.2) we find $\Delta\lambda_{FWHM} = 0.92 \pm 0.08 \text{ nm}$ for the vertical and $0.196 \pm 0.002 \text{ nm}$ for the horizontal linefocus.

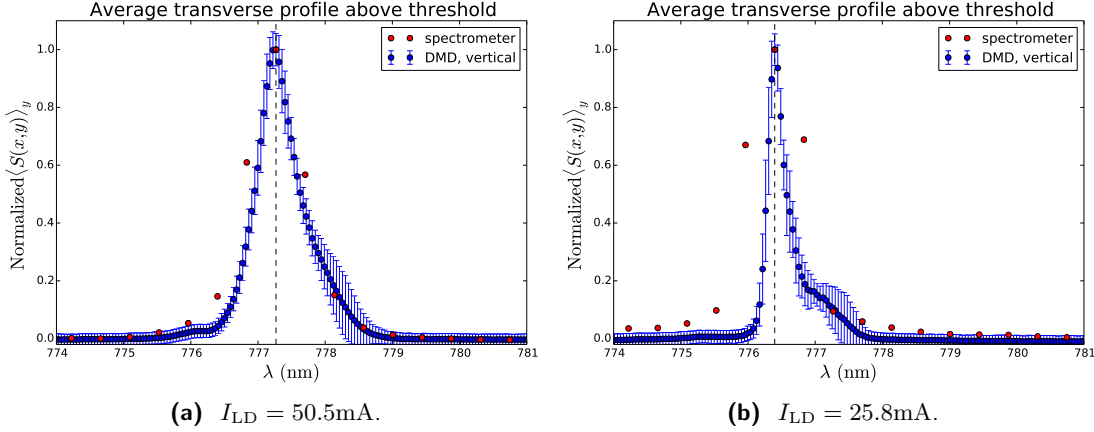


Figure 4.4: In blue: the transverse profile of a vertical linefocus above threshold averaged over y . The transverse position x has been scaled to wavelength λ using Eq. 4.1. In red: the laser diode spectrum at the same current, measured with a spectrometer.

set is shown normalized to its own maximum value after having its own background subtracted, because the data are recorded with different devices. For the linefocus data, $I_{bg}(y)$ is used as a background estimate; for the spectrometer data the average reading between 870.5 nm and 1092.3 nm is used. The errorbars show the variation along y relative to the peak intensity at that longitudinal position (i.e. $\sqrt{\text{var}_y(\frac{S(x,y)}{I_{peak}(y)})}$) and are therefore indicative of the consistency of the shown profile along the length of the linefocus. The errors of the spectrometer data are not known.

4.2.2 Longitudinal dispersion

In this section we investigate horizontal linefoci and quantify the dependence of the longitudinal dispersion on $\Delta\lambda_{FWHM}$. To that end, we use the DMD to create sharp edges in the longitudinal direction. We use the width of these edges, Δy_{edge} , as a measure of the longitudinal dispersion caused by spectral broadening. We expect Δy_{edge} to increase below threshold when the dispersion is longitudinal, just as the FWHM increases below threshold when the dispersion is transverse.

To find Δy_{edge} we sum the intensity in the transverse direction over a region of interest (150 pixels wide) that contains the entire horizontal linefocus⁹. The resulting data are visually divided into three regions. One region containing the data points that comprise the edge, a second region containing the 200 data points to the left of the edge and a third region containing the 100 points to the right of the edge. Subsequently we perform a separate linear fit to the data in each region. The intersections of these three linear fits

⁹This approach is preferable to the transverse gaussian fits used so far, because those fits become inaccurate at the low end of an edge and we are interested in the change in total intensity anyway.

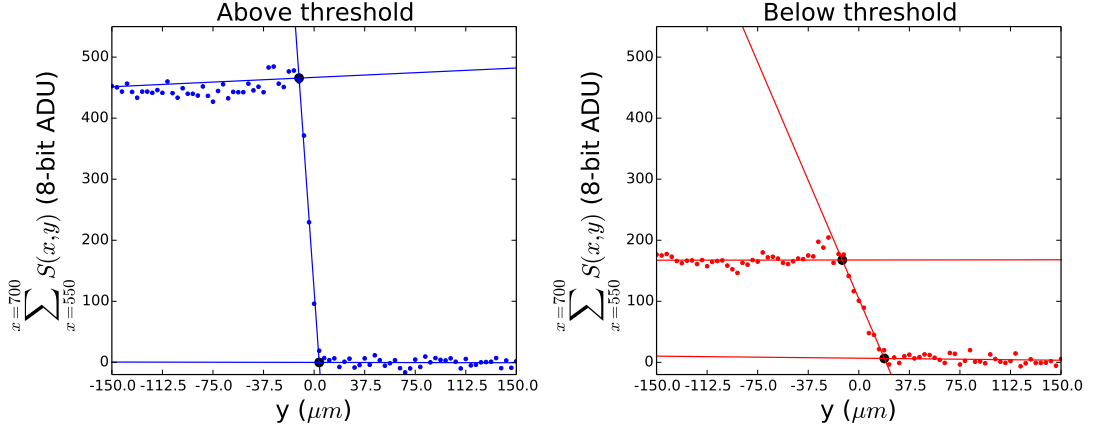


Figure 4.5: In this figure the data and linear fits used to calculate longitudinal dispersion above and below threshold are shown. The thick black dots indicate the intersections of the linear fits, the edge width is defined as the horizontal distance between two intersections. Below threshold we find $\Delta y_{\text{edge}} = 31 \pm 1.7 \mu\text{m}$, above threshold we find $\Delta y_{\text{edge}} = 15 \pm 1.3 \mu\text{m}$. Both figures are shown on the same scale. See text for further explanation.

are good estimates of the leftmost and the rightmost borders of the edge and so Δy_{edge} can be found from the distance parallel to the horizontal axis between the intersections. The error on Δy_{edge} can be obtained straightforwardly from error propagation of the errors of the linear fits, we assumed their covariance matrix to be diagonal.

The results of this analysis are shown in Fig.4.5, for horizontal linefoci above threshold ($I_{\text{LD}} = 51.2 \text{ mA}$) and below threshold ($I_{\text{LD}} = 18.2 \text{ mA}$). The intersections of the linear fits are shown as big black dots. We find $\Delta y_{\text{edge}} = 31 \pm 1.7 \mu\text{m}$ below threshold and $\Delta y_{\text{edge}} = 15 \pm 1.3 \mu\text{m}$ above threshold. This means that when the spectrum broadens by a factor of 10, the longitudinal dispersion only doubles. By comparison, we found in the previous section that the transverse dispersion increases 15-fold. Comparing Δy_{edge} above and below threshold to the transverse FWHMs of the horizontal linefoci (see Table 4.2), which are $31.9 \pm 0.8 \mu\text{m}$ and $16.4 \pm 0.2 \mu\text{m}$ respectively, we find remarkably good agreement. This agreement indicates that the minimum edge width of the vertical linefocus is limited by the same factors as its transverse FWHM, namely the (wavelength-dependent) pointspread function of the optical system. We conclude that, within the accuracy of our measurement, the pointspread function of the imaging system is not affected by the angular dispersion caused by the DMD, meaning that the imaging system can compensate for the dispersion that would be found in an ultrashort pulse.

Since the slope of the linear fit in the edge region depends on the value at the upper edge, the Δy_{edge} we find by this method depends on it as well. To check whether this dependence is significant, we recalculate Δy_{edge} after first normalizing both data sets to their own maximum value, which yields $31.9 \mu\text{m}$ below threshold and $15.0 \mu\text{m}$ above. Alternatively, if we rescale the data below threshold so that it has the same maximum as the data above threshold we find $14.9 \mu\text{m}$ above threshold and $30.9 \mu\text{m}$ below. So

although an effect is present, it falls well within the error margin.

4.3 Beamshaping spectrally broadened light

In this section we show that, in our model system, beamshaping is possible below threshold and achieves comparable rms-flatness as shaping above threshold. It is shown above that the horizontal orientation compensates dispersion much better than the vertical orientation does. That makes the horizontal linefocus the most feasible candidate for use with ultrashort pulses, so we only report beamshaping for that configuration.

Figs.4.6 and 4.7 show the results of transverse gaussian fits (see Eq. 3.1) of a vertical linefocus at $I_{LD} = 18.2$ mA for the parameters $I_{\text{peak}}(y)$, $2.355 \times \sigma(y)$, $\mu(y)$ and $I_{\text{bg}}(y)$ before and after beamshaping. The values shown are time averages and the errorbars are the standard deviation of the data at that position over time, where the time axis consists of 50 images of the same linefocus taken at random time intervals smaller than one second. The average fitting errors are given for each parameter in Table 4.1.

The I_{peak} figure shows that a flattop is produced succesfully: the rms-flatness within the region of interest is reduced from 21% to 6%. As desired, the other fitparameters are virtually unchanged by the beamshaping procedure, as is shown in Table 4.1. The average error bar, representing time variation, of the shaped (unshaped) data is 0.63ADU (1.11ADU).

The mean positions are curved below threshold, just as they are above threshold. Performing the same quadratic fits as in Fig. 3.8a we find similar curvatures of $3.24 * 10^{-6} \pm 0.01 * 10^{-6} \mu\text{m}^{-1}$ and $3.20 * 10^{-6} \pm 0.01 * 10^{-6} \mu\text{m}^{-1}$ for the unshaped and shaped data respectively. The average error bar, representing time fluctuation, of the shaped (unshaped) data is $1.21\mu\text{m}$ ($1.07\mu\text{m}$).

We find no significant difference below threshold in the FWHM before and after beamshaping. This shows that the dependence of the FWHM on the shaping strength, which is present above threshold (see Fig. 3.6b), only occurs for coherent light. The average error bar, representing time fluctuation, of the shaped (unshaped) data is $0.59\mu\text{m}$ ($0.26\mu\text{m}$).

The average error bar, representing time fluctuation, of the shaped (unshaped) I_{bg} data is 0.14ADU (0.030ADU).

It is remarkable that our beamshaping method, using kinoforms randomized per column, does not seem to suffer significantly from the broadening of the point spread function below threshold. This is probably because we shape the *large* features of the beamprofile. So as long as light from a DMD column ends up on the correct average position any broadening of the pointspread function is approximately compensated by the neighbouring columns, so that, on average, the shaping strength ends up where it is supposed to.

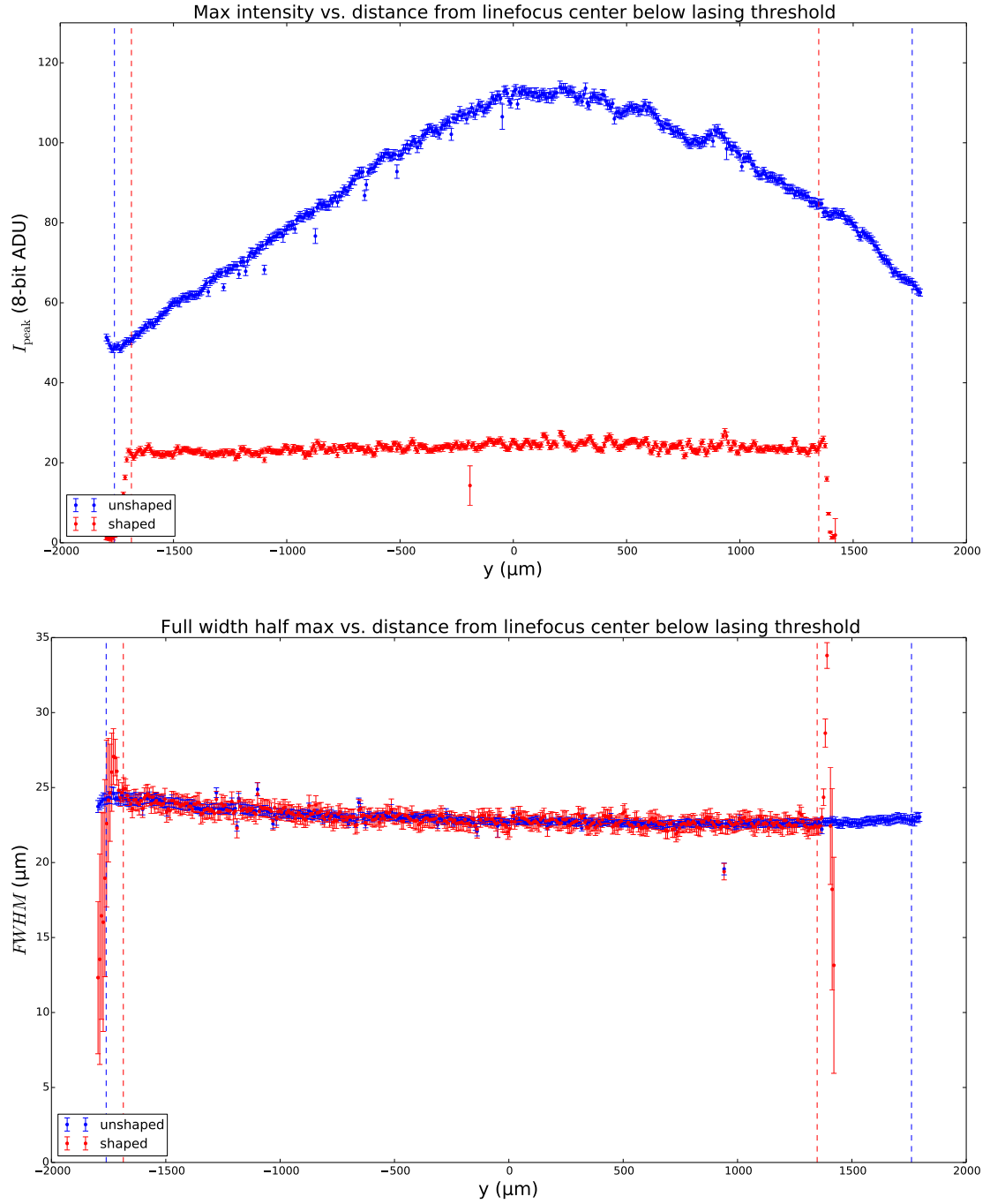


Figure 4.6: The gaussian fit values of I_{peak} and the FWHM (see Eqn. 3.1) for the horizontal linefocus (longitudinal dispersion), red for the vertical linefocus (transverse dispersion). See Table 4.1 for further details. In both cases the transverse fits were made over 200 pixels. To reduce cluttering, each point here represents two adjacent data points. The error bar shown is the standard deviation of the fitted value at that position over 50 consecutive shots. For both linefoci, 4% of the rows were discarded in the masking procedure.

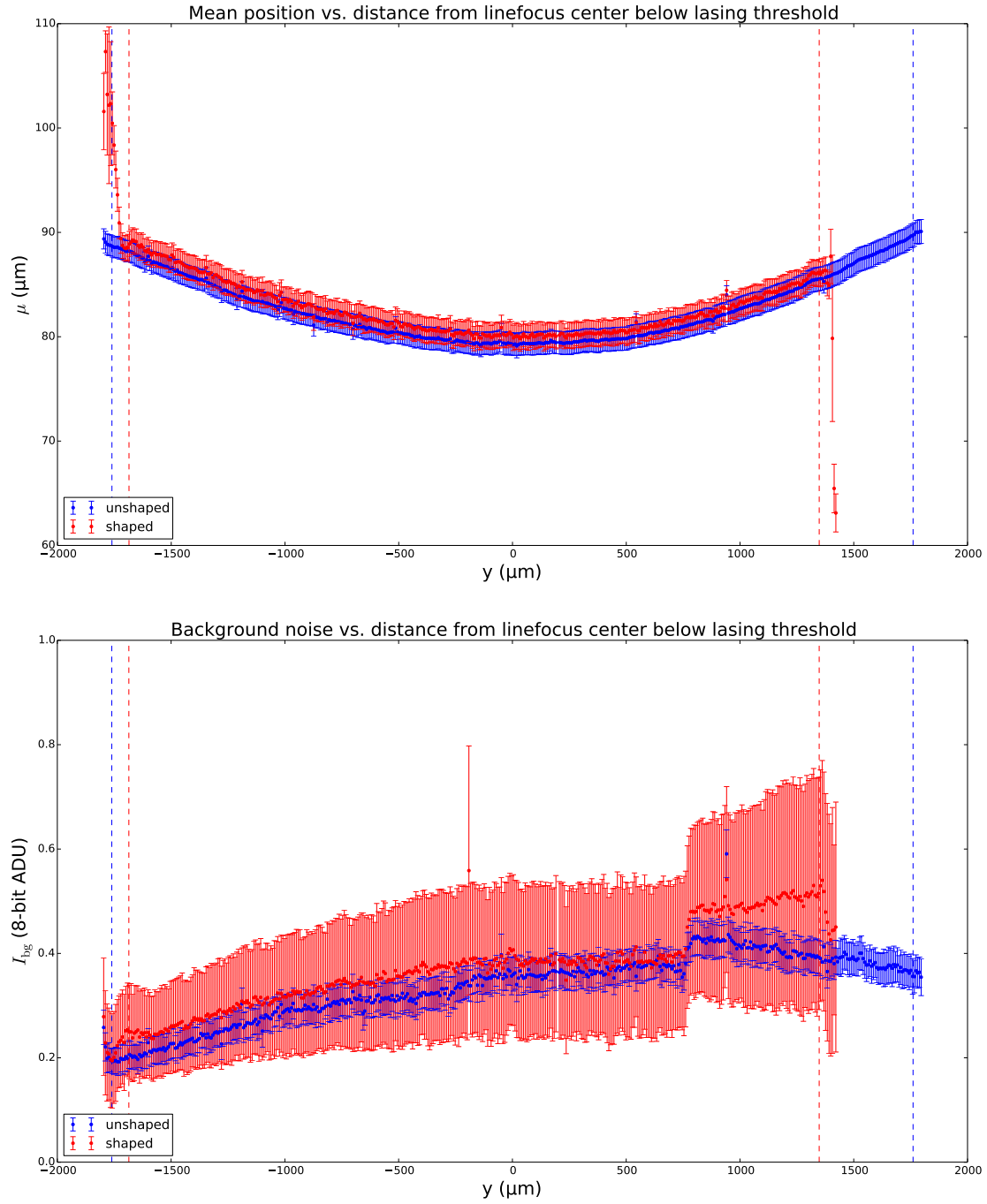


Figure 4.7: The gaussian fit values of the μ and I_{bg} (see Eqn. 3.1) for the horizontal linefocus (longitudinal dispersion), red for the vertical linefocus (transverse dispersion). See Table 4.1 for further details. In both cases the transverse fits were made over 200 pixels. To reduce cluttering, each point here represents two adjacent data points. The error bar shown is the standard deviation of the fitted value at that position over 50 consecutive shots. For both linefoci, 4% of the rows were discarded in the masking procedure.

Parameter	Horizontal below lasing threshold		Horizontal above lasing threshold	
	Before beamshaping	After beamshaping	Before beamshaping	After beamshaping
Intensity I_{peak} (ADU)	$89.3 \pm 18.3 \pm 0.5$	$23.7 \pm 1.4 \pm 0.3$	$116 \pm 35 \pm 1.0$	$57 \pm 2.5 \pm 0.7$
FWHM (μm)	$23.0 \pm 0.6 \pm 0.2$	$23.0 \pm 0.6 \pm 0.3$	$15.8 \pm 0.3 \pm 0.17$	$15.0 \pm 0.5 \pm 0.2$
Mean position μ (μm)	$82.8 \pm 3.0 \pm 0.07$	$82.7 \pm 2.5 \pm 0.1$	$1.27 \pm 8.88 \pm 0.07$	$3.64 \pm 8.89 \pm 0.09$
Background I_{bg} (ADU)	$0.34 \pm 0.06 \pm 0.06$	$0.37 \pm 0.08 \pm 0.04$	$0.5 \pm 0.2 \pm 0.24$	$0.5 \pm 0.2 \pm 0.16$

Table 4.1: Average values of the gaussian fit-parameters for the linefoci shown in Fig.4.6. To negate edge effects, these numbers are calculated for the data between the vertical lines of the appropriate color. The first number indicates the average of the fit-parameter (e.g. $\langle \text{FWHM}(y, t) \rangle_t$), the second its standard deviation (e.g. $\sqrt{\text{var}_y(\langle \mu(y, t) \rangle_t)}$), and the third its average fitting error. For easy reference, the data above threshold from Table 3.1 is reproduced in the rightmost columns. In all cases, fits are calculated from a ROI 200 pixels wide.

4.4 Gaussian fits for vertical and horizontal linefoci above and below threshold

For reference, we list in this section the properties of horizontal and vertical linefoci above ($I_{\text{LD}} = 51.2\text{mA}$) and below ($I_{\text{LD}} = 18.2\text{mA}$) the lasing threshold, for $\eta = 0$.

4.4.1 Parameter plots

Figs.4.8 and 4.9 show the mean values over time of the four gaussian fitparameters in these four situations as a function of longitudinal position. The error bars show the standard deviation over time, the average fitting errors are shown in Table 4.2. To reduce cluttering, each data point represents 6 adjacent data points binned together.

Regarding I_{peak} , we must first note that the the relative intensities of the linefoci above and below threshold are not meaningful because different ND-filters are used to record them. The relative intensities of the horizontal and vertical orientations at the same current are comparable however. We find that I_{peak} is lower in the vertical cases, which is primarily because the linefocus is wider and total power is conserved. The I_{peak} profile changes when the cylindrical lens is reoriented because the gaussian input beam is not fully symmetric around the optical axis.

The increase of the FWHM below threshold has already been described in Sec.4.2.1. Fig.4.8 shows, additionally, that the FWHM of the horizontal linefoci is far more constant in space and time than the FWHM of the vertical linefoci. The FWHM for a vertical linefocus below threshold, which is over an order of magnitude larger than the others, is shown separately in Fig.4.10.

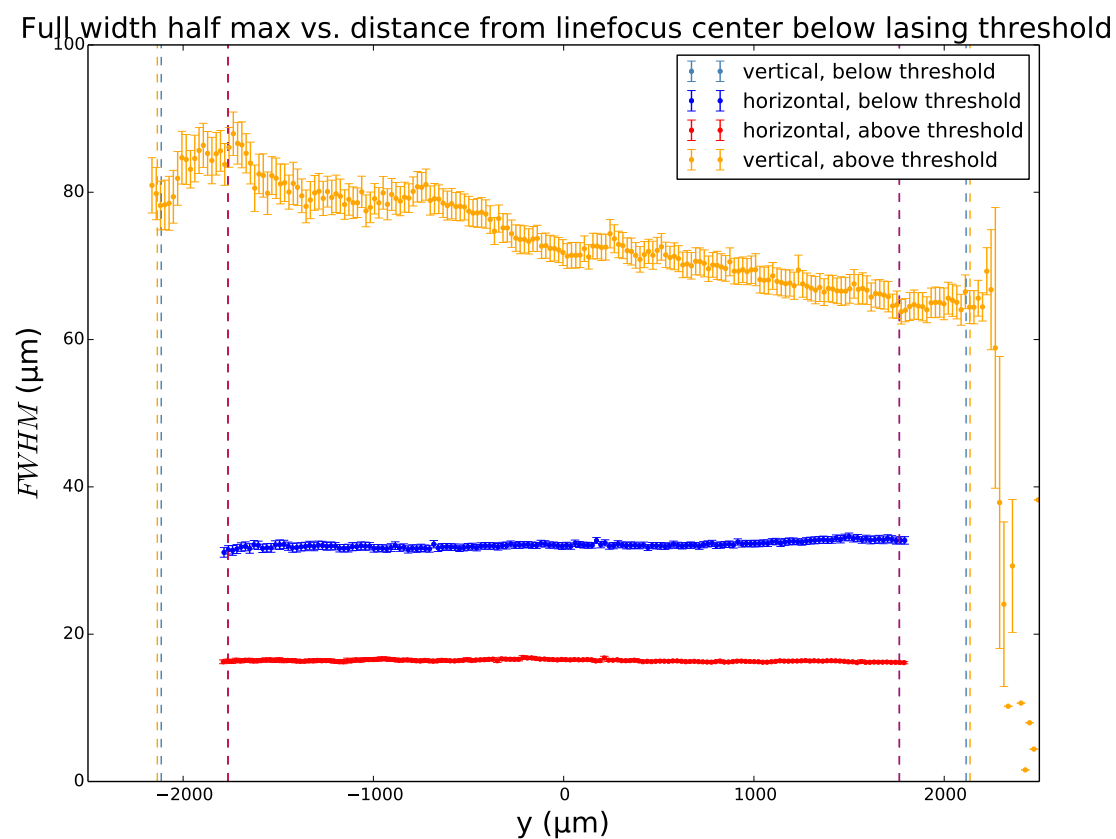
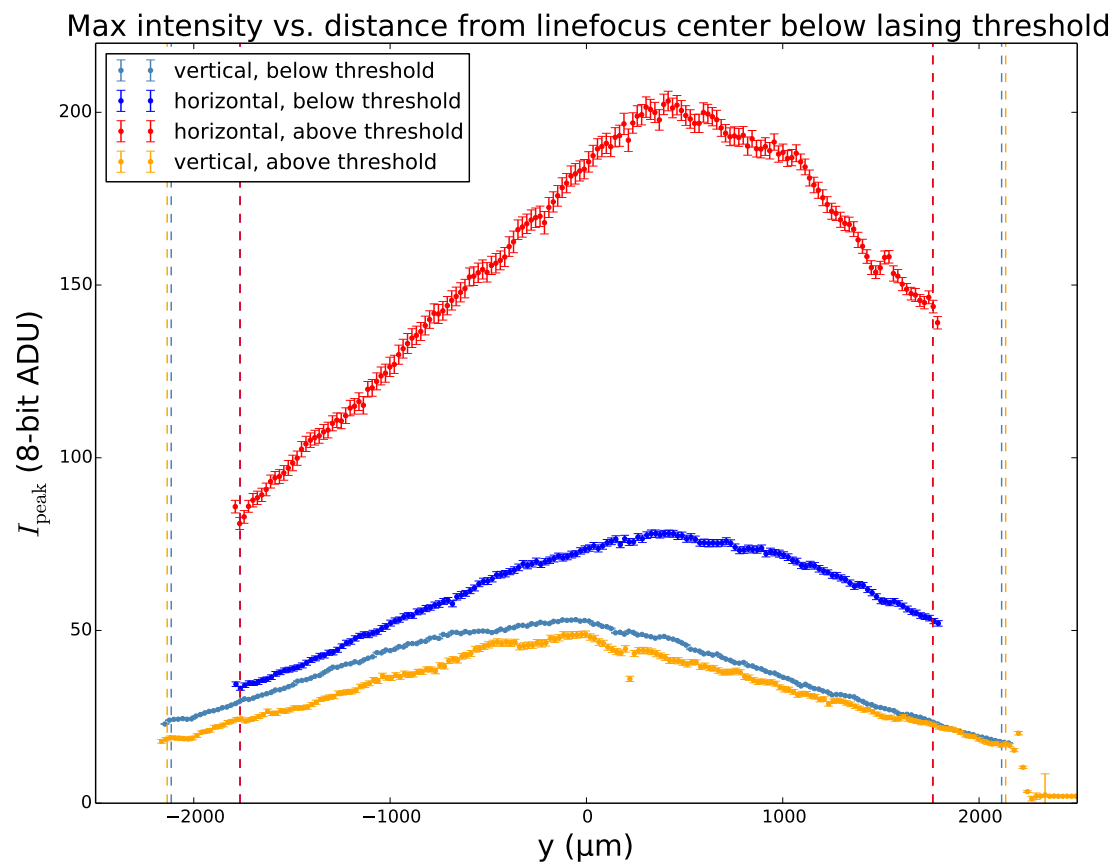


Figure 4.8: The gaussian fit values of I_{peak} and the FWHM. See Fig.4.10 for all FWHMs and Fig. 4.9 for further details.

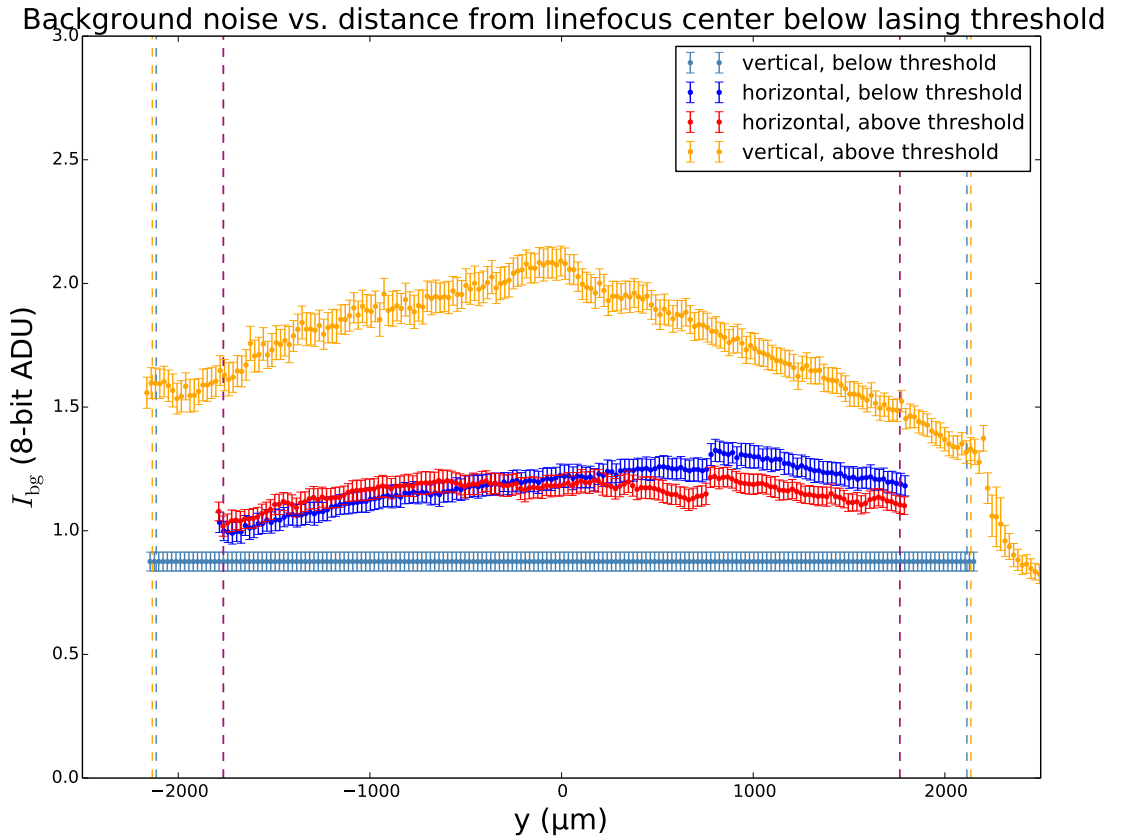
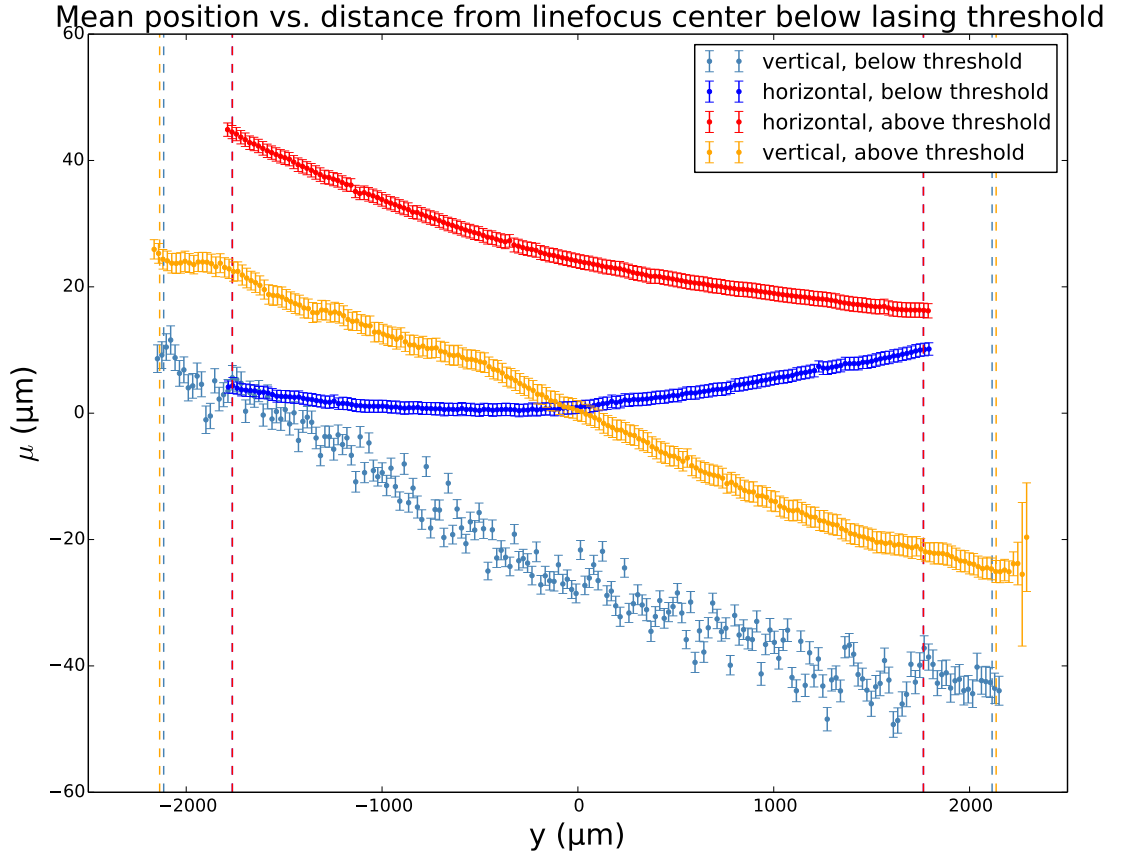


Figure 4.9: The gaussian fit values of μ and I_{bg} (see Eq. 3.1) for the horizontal and vertical linefocus above and below threshold. See Tables 4.2 and 4.3 for further details. In all cases the transverse fits are made for 960 pixels. To avoid cluttering, each point here represents the average of four adjacent data points. The error bar shown is the square root of the quadratic sum of the error bars of the individual points. For the horizontal linefocus, 4% of the rows were discarded in the masking procedure versus 16% of the columns for the vertical linefocus. Below threshold we set $I_{\text{LD}} = 18.2\text{mA}$ and above threshold $I_{\text{LD}} = 51.2\text{mA}$.

Parameter	Above lasing threshold		Below lasing threshold	
	Horizontal	Vertical	Horizontal	Vertical
Intensity I_{peak} (ADU)	$159.8 \pm 34.0 \pm 0.8$	$32.5 \pm 9.3 \pm 0.7$	$43.3 \pm 9.6 \pm 0.4$	$21.0 \pm 3.3 \pm 0.1$
FWHM (μm)	$16.4 \pm 0.2 \pm 0.1$	$77 \pm 7 \pm 2$	$31.9 \pm 0.8 \pm 0.4$	$1193 \pm 8 \pm 7$
Mean position μ (μm)	$26.42 \pm 8.05 \pm 0.04$	$0.51 \pm 15.5 \pm 0.8$	$7.0 \pm 3.0 \pm 0.1$	$-13 \pm 26 \pm 3$
Background I_{bg} (ADU)	$1.16 \pm 0.06 \pm 0.08$	$1.8 \pm 0.2 \pm 0.17$	$1.12 \pm 0.12 \pm 0.06$	$0.98 \pm 0.0 \pm 0.0$

Table 4.2: Average values of the gaussian fit-parameters for the linefoci shown in Figs.4.8 and 4.9. To negate edge effects, these numbers are calculated for the data between the vertical lines of the appropriate color. The first number indicates the average of the fit-parameter (e.g. $\langle \langle I_{\text{peak}}(y, t) \rangle_t \rangle_y$), the second its standard deviation in space (e.g. $\sqrt{\text{var}_y(\langle I_{\text{peak}}(y, t) \rangle_t)}$), and the third its average fitting error. The horizontal situation above threshold is comparable to the data reported in 3.1.

The mean positions μ are shifted in Fig.4.9a to make them cross around the middle of the linefocus. We observe that $\mu(y)$ is curved for the horizontal linefocus but *not* for the vertical linefocus, for which it is roughly straight instead. The curvatures found by quadratic fits are: vertical, below threshold $2.11 * 10^{-6} \pm 0.08 * 10^{-6} \mu\text{m}^{-1}$; vertical above threshold $0.02 * 10^{-6} \pm 0.029 * 10^{-6} \mu\text{m}^{-1}$; horizontal, below threshold $1.73 * 10^{-6} \pm 0.02 * 10^{-6} \mu\text{m}^{-1}$ and horizontal above threshold $1.84 * 10^{-6} \pm 0.03 * 10^{-6} \mu\text{m}^{-1}$. This confirms the idea that the curvature of $\mu(y)$ is related to the curvature of the DMD's surface, as is also found in Fig. 3.8b, but further indicates that the curvature is relevant only in the DMDs long dimension. The curvature of horizontal linefoci is not dependent on the coherent properties of the beam, because it occurs above and below threshold.

Concerning I_{bg} we only note that, since a full fit for the vertical linefocus below threshold is prohibited because the linefocus is broader than the CCD, we set I_{bg} equal to the average intensity of an empty region of the relevant image. For that reason the light blue data for I_{bg} varies in time but not in space.

4.4.2 Variation over time

As shown in Table 4.2, the fitting error of μ , although it increases with the FWHM, is much smaller than the time-variation represented by its error bar: over time, .

We conclude this section by investigating the stability over time of I_{peak} , μ and FWHM. We compare the horizontal and vertical orientations, broad and narrow spectra and shaped and unshaped intensities. The stability over time is characterized by preparing a linefocus and then recording and fitting 50 consecutive images at random time intervals smaller than a second.

Two quantities are calculated from those data and are shown in Table 4.3. First,

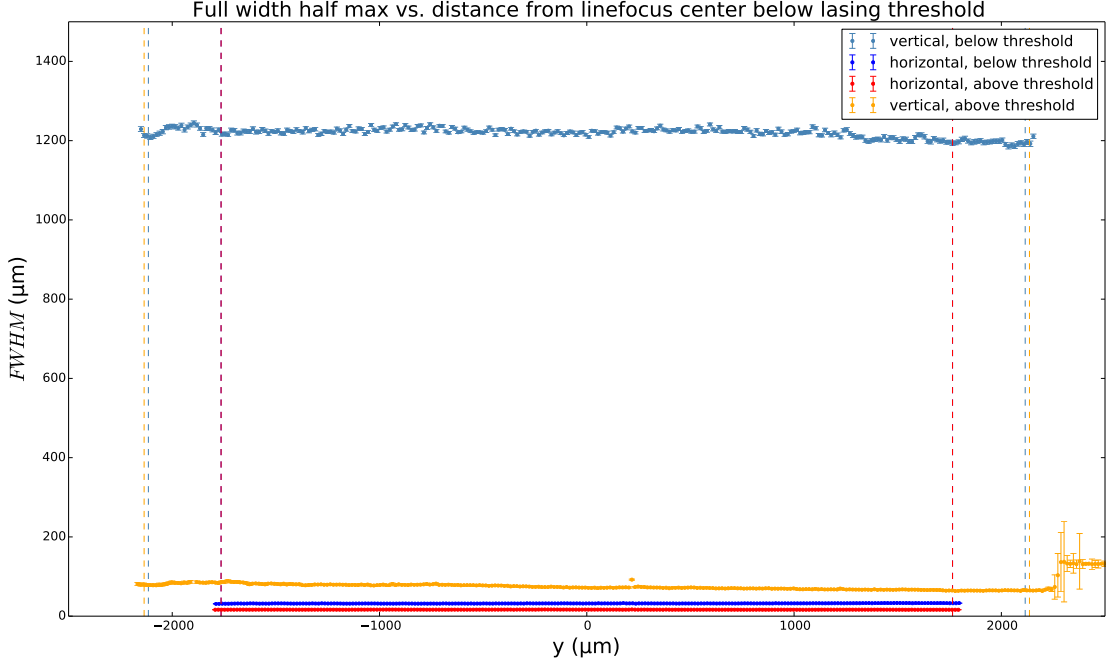


Figure 4.10

$\sqrt{\text{var}_t(\langle p(y, t) \rangle_y)}$, the standard deviation over time of the average value of each parameter - i.e. the variation of the mean, which is interpreted as the global time variation of the parameter. Second, $\langle \sqrt{\text{var}_t(p(y, t))} \rangle_y$, the average over space of the standard deviation over time of the values of each parameter - i.e. the mean variation, which is interpreted as the (average) local time variation of the parameter. Since we found that the values of I_{peak} change when the cylindrical lens is rotated and the time fluctuation of I_{peak} is expected to scale with its value, we report the relative time fluctuation for I_{peak} , i.e. $\sqrt{\text{var}_t(\langle I_{\text{peak}}(y, t) / \langle I_{\text{peak}}(y, t) \rangle_t \rangle_y)}$ and $\langle \sqrt{\text{var}_t(I_{\text{peak}}(y, t) / \langle I_{\text{peak}}(y, t) \rangle_t)} \rangle_y$.

Note that the variations of μ show the influence of the orientation, spectral width and beamshaping on the *pointing uncertainty* of the test setup. The observation that the global and local variation of μ is almost identical, indicates that the linefocus' position varies as a whole, possibly due to vibrations in the setup. The fact that the time fluctuation does not increase more than two-fold due to our beamshaping procedure - even for a spectrally broadened beam - gives confidence that the shaped linefocus will be stable in the ultrashort pulse setup.

Both the global and local variation are reported because their difference shows the effect of fitting errors on the calculated time variation. The fitting errors have nothing to do with time variation per se, but will increase the reported local time variation because the fitting errors statistically distribute the fitvalues. The fitting errors¹⁰ average out for

¹⁰And other variations that are compensated by neighbouring pixels.

Parameter	Above lasing threshold		Below lasing threshold			
	Hor	Ver	Hor	Ver	Hor, Shaped	Hor, Unshaped
relative global variation of I_{peak}	1.24%	1.49%	0.60%	0.064%	0.89%	0.39%
relative local variation of I_{peak}	1.62%	2.16%	1.45%	0.31%	2.84%	1.28%
global variation μ (μm)	1.09	1.52	0.95	1.02	1.18	1.05
local variation μ (μm)	1.10	1.75	0.97	1.71	1.21	1.07
global variation FWHM (μm)	0.14	1.33	0.73	2.00	0.12	0.082
local variation of FWHM (μm)	0.20	2.09	0.74	4.21	0.54	0.25

Table 4.3: As in Table 3.3, the quantities presented characterize the stability of the linefocus over time. Listed are both orientations above laser threshold (laser diode current: 51.2 mA) and below laser threshold (laser diode current: 18.2 mA). The first four columns from the left are calculated for the data in Fig.4.8, the two rightmost columns concern the data shown in Fig.4.6. All data is recorded with an 18 ms camera integration time. Fifty consecutive shots with random time intervals represent the time dimension. In the two rightmost columns 200 pixels are used to fit the parameters, versus 960 pixels in the other columns.

the global variation but not for the local variation. In the table, we indeed consistently find that the global time variation is smaller than the average local time variation. The observation that the difference between the global variation and the local variation is generally larger for vertical than for horizontal linefoci is thus explained by the fact that the vertical linefocus generally has a higher fitting error than the horizontal linefocus.

4.5 Depth of focus and depth of image

To confirm the applicability of the hybrid mode to an ultrashort pulse setup, we measure the depth of focus (Rayleigh range) of a horizontal linefocus produced by the hybrid mode setup in this final section. To make alignment of a the hybrid mode with a microscope objective feasible, not only the depth of focus but also the 'depth of image' - i.e. the thickness of the image plane - must not be too small. While the depth of focus is expected to increase when the spectrum is broadened, the depth of imaging is expected to decrease. The relevance of knowing the depth of image is further illustrated by the $I_{\text{peak}}(y, z)$ data in Fig.4.11b, which show that edge-fringes can develop into strong intensity peaks for misalignments of less than 0.5 mm.

By recording the beamprofile along the optical axis (z -direction), we find the beam

Parameter	FWHM(z)	$\Delta y_{\text{edge}}(z)$
$w_0(\mu\text{m})$	6.0 ± 0.65	18.5 ± 1.5
$z_R(\mu\text{m})$	513 ± 56	1750 ± 99
$z_0(\mu\text{m})$	1306 ± 45	1472 ± 315
a	-0.0012 ± 0.0002	-0.002 ± 0.001

Table 4.4

waist as a function of z from FWHM fits for a range of about 1 cm. . The depth of image is found from the same data by calculating the width of a longitudinal edge, Δy_{edge} , as a function of z , using the method described in Sec.4.2.2. The results of these measurements are shown in Fig.4.11a, performed at $I_{\text{LD}} = 44.95 \text{ mA}$ (at this current no multimode lasing was observed). The target plane that was used throughout this chapter, which is determined as the position where Δy_{edge} is minimal, is at $z = 0$.

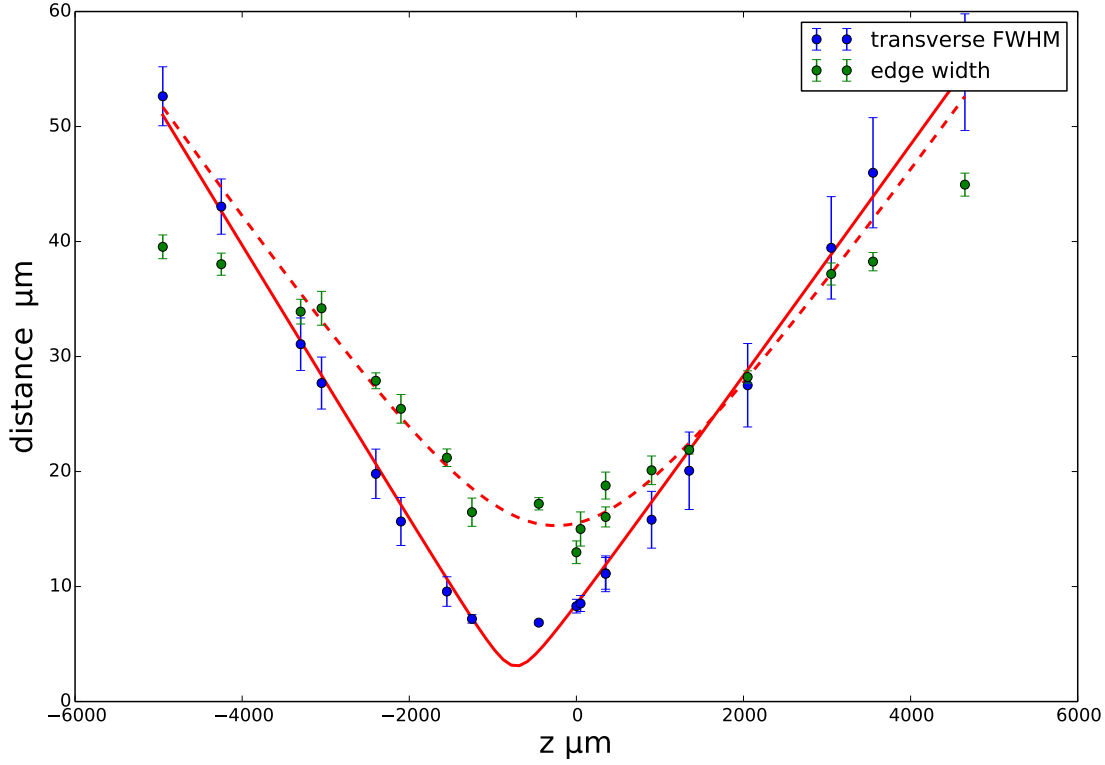
As a fit function we use $w_0 \sqrt{1 + ((z - z_0)/z_R)^2} + az$, for both $\text{FWHM}(z)$ and $\Delta y_{\text{edge}}(z)$. This function is adapted from the beam waist of a gaussian beam, given by $w(z) = w_0 \sqrt{1 + (z/z_R)^2}$, where z is the position along the optical axis, $z_R = \frac{\pi w_0^2}{\lambda}$ is the Rayleigh range and w_0 is the minimum beam waist. The dimensionless parameter a is included to account for the different slopes in Fig.4.11a to the left and right of the minimum waist¹¹. For an ideal gaussian beam, assuming the spot size on the lens has approximately the same dimension as the DMD array, we have $w(z = -15 \text{ cm}) = 6.16 \text{ mm}/2$ and, with $f = 15 \text{ cm}$ and $\lambda = 777 \text{ nm}$ we find $z_R = 0.22 \text{ mm}$ and $w_0 = 7.42 \mu\text{m}$. Fitting the $\text{FWHM}(z)$ we find $z_R = 0.51 \pm 0.06 \text{ mm}$ so the linefocus' Rayleigh range is about twice as large as that of a comparable ideal gaussian beam. Fitting $\Delta y_{\text{edge}}(z)$ we find $z_R = 1.7 \pm 0.1 \text{ mm}$. So we conclude that, since the depth of image is larger than the depth of focus, no alignment issues are expected when a microscope objective is used. For the values of all fit parameters see Table 4.4.

The fitted values of z_0 show that, in our test setup, the image and Fourier planes coincide to an accuracy within their fitting error. The effect of the spectral width on the depth of focus can be determined by performing the same measurement again below the lasing threshold.

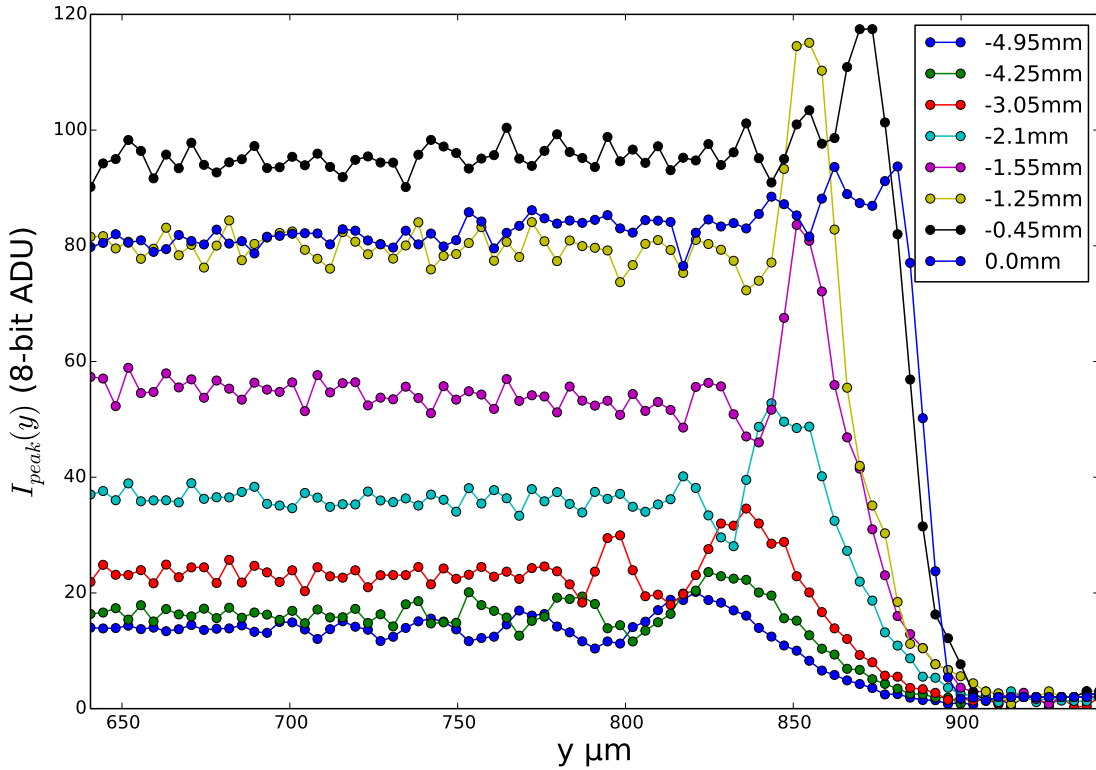
4.6 Conclusion

In this chapter we have found that spectral broadening by a factor 10 leads to longitudinal dispersion in a horizontal linefocus by a factor 2 and to transverse dispersion in a vertical linefocus by a factor 15. So the hybrid mode setup can largely compensate for broad spectra if the dispersed direction is imaged. Beamshaping works as well with spectrally broadened light as it does for light with narrow spectral width, and the resulting linefocus

¹¹if $a \equiv 0$, we find a Rayleigh range that is about 10% larger and a worse χ^2 fitting error



(a) Fit function: $\text{FWHM}(z) = w_0 \sqrt{1 + ((z - z_0)/z_R)^2} + az$. z is the distance from the imaging plane. The full red curve is the fit result of the transverse $\text{FWHM}(z)$, the dotted red curve is the fit result of $\Delta y_{\text{edge}}(z)$. The values of the fit parameters can be found in Table 4.4. For the $\Delta y_{\text{edge}}(z)$ fit, the two leftmost and the two rightmost points are discarded. The error bars of $\text{FWHM}(z)$ are the standard deviation of the FWHM of the linefocus at that position (i.e. $\sqrt{\text{var}_y(\text{FWHM}(y, z))}$). The error bars of $\Delta y_{\text{edge}}(z)$ come from error propagation of the three linear fits used to determine the edge width. The transverse ROI for the gaussian fits was 200 pixels wide.



(b) Gaussian fitted peak intensity of a horizontal linefocus for several positions in front of the target plane ($z < 0$ mm) for $I_{\text{LD}} = 44.95$ mA. Observe the fringes extending up to a few hundred μm into the bulk, which have an exceptionally low fitting error. Compare also Fig.4.5.

is stable in time. The curvature of the horizontal linefocus persists for non-coherent light, indicating that it is due to the curvature of the DMD. Sharp edges in kinoforms should be avoided to make precise alignment less critical. Since the depth of imaging is on the order of the depth of focus, no serious alignment issues are expected, so it is recommended to perform similar experiments with an actual pulse laser.

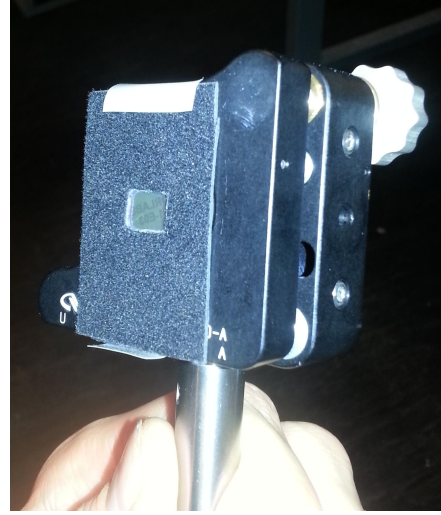
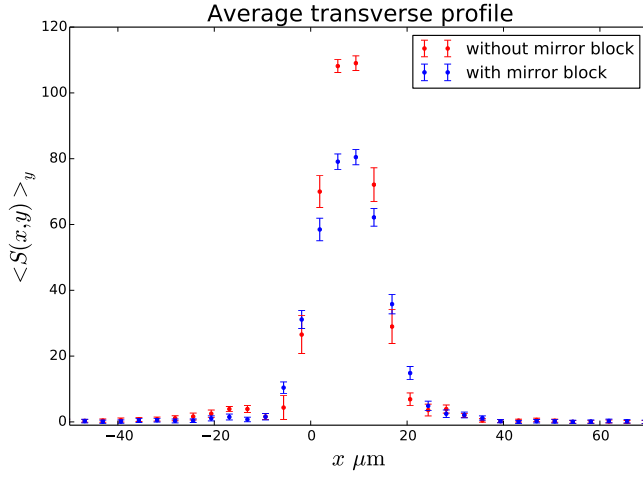


Figure 5.1: In this figure the DMD is replaced with a mirror and a removable mirror block is installed on the surface of the mirror, which has roughly the same dimensions as the DMD. Average transverse profiles calculated for linefoci with and without mirror block. The mirror block used is shown on the right.

5 Discussion

In this section we discuss questions that remained unanswered in previous chapters. We also provide an outlook to further experiments with beamshaped ultrashort pulses using the hybrid mode setup.

5.1 Effects of overfilling the DMD

We have not commented on the effect that overfilling the DMD has on the beam-profile. To find out what the effect is of the aperture shape of the DMD's active array, we place a removable mirror block with a hole that has approximately the same dimensions as the DMD on top of a mirror. The result is given as the average transverse profile in Fig.5.1 (see Sec.4.2.1 for the details of this analysis method). Due to diffraction, apertures normally produce fringes but Fig.5.1 shows that the profile of our quasi-gaussian beam gets more gaussian when the aperture effects are included. This is quantified by the average χ^2 fitting error, which is 73.1 with mirror block, and 161.4 without mirror block. However, without the mirror block, the linefocus is $13.1 \mu\text{m}$ wide, versus $16.2 \mu\text{m}$ with mirror block. I_{peak} is of course lower when the mirror block is placed due to the cutting of the tails in the transverse direction (see Table 5.1 for numbers). By comparing summed intensities, we find that 89% of the incident power remains after clipping.

Parameter	With mirror block	Without mirror block
Intensity I_{peak} (ADU)	$83.5 \pm 8.2 \pm 0.4$	$115.9 \pm 11.7 \pm 0.7$
FWHM (μm)	$16.2 \pm 0.5 \pm 0.1$	$13.1 \pm 0.89 \pm 0.09$
Mean position μ (μm)	$0.2 \pm 10.37 \pm 0.04$	$0.0 \pm 10.29 \pm 0.04$
Background I_{bg} (ADU)	$0.24 \pm 0.05 \pm 0.05$	$0.37 \pm 0.06 \pm 0.07$

Table 5.1: Averages of transverse gaussian fits of linefoci. The DMD is replaced with a mirror. The first number gives the average value (e.g. $\langle I_{\text{peak}}(y) \rangle$), the second number the variation in space (e.g. $\sqrt{\text{var}_y \mu(y)}$) and the final number the fitting error.

5.2 Power efficiency and phase control

Our shaping method would increase its uses if it were capable of phase control, besides the intensity control that has already been displayed. Schemes granting phase control in the target plane using a DMD have been devised [3, 16], but rely on using orders that are created by using (quasi-)periodic kinoforms. We found a total efficiency of less than 1% when reproducing this phase-control scheme, which is a loss of usable laser power that we cannot afford in our intended setup. In our hybrid mode setup, it is in principle possible to use a DMD-column as a 'superpixel' and bias the probability distribution by which pixels are turned off in order to correct a phase profile. Iterative algorithms exist to calculate such phase profiles [2].

We can estimate the total power efficiency of our beamshaping method $\eta_{\text{total}} = \eta_{\text{clipping}} \times \eta_{\text{diffraction}} \times (1 - \eta) \sim 24\%$ to 44% . Where we use $\eta_{\text{clipping}} = 89\%$, $\eta_{\text{diffraction}} = 55\%$ (see Sec. 1.3) and recall that η is the shaping strength, which typically ranges from 0.1 to 0.5.

5.3 Time variation due to periodic mirror flipping patterns

Some standard features of the DMD are not optimal for our purposes. We trace back the periodic variation of I_{peak} (see Sec.3.4) to the script we wrote to address the DMD, which has been used throughout this thesis. Although the script was based on the programmer's guide for the DLP series (Ref. [11]) it produces images that are not truly static. The documentation provided at the time we undertook our project was insufficient to resolve this issue. The manufacturer's intended setup for the DLP4500NIR DMD involves three colored LEDs which are sequentially blazed by flipping micromirrors. To bypass these color functionalities and obtain static images, the Pattern Display mode must be used. Even in Pattern Display mode, only 24-bit images containing only (0, 0, 0) or (255, 255, 255) as entries avoid the color sequencing functionality. The manufacturer provides a graphical user interface (GUI), going by the name Lightcrafter, through which these settings can be accessed. In this section we report the difference between kinoforms loaded using the Lightcrafter GUI and using our script.

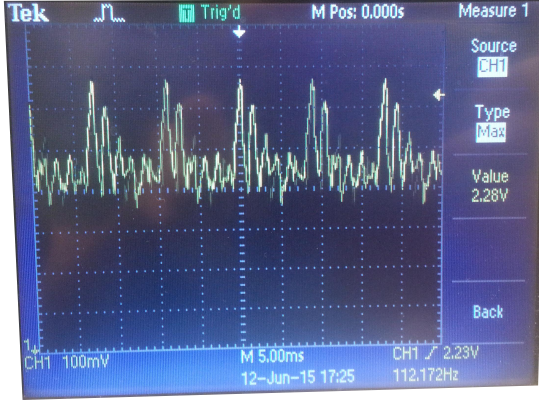
First, we record the previously observed time variation with high temporal resolution, we set up a photodiode (PD) in the focus of a spherical 15 cm-lens and display kinoforms with varying shaping strength¹² on the DMD, using our own script. All light in the blazed order is collected on the receptor of the PD. The PD-signal is displayed on an oscilloscope (Tektronix TDS2022B) yielding images such as Fig.5.2a, showing that the intensity can fluctuate strongly on millisecond timescales. For any kinoform, the signal varies with a period of 17.8ms, explaining why we can suppress the time variation by using a camera integration time of 18 ms. The average PD-signal and the peak-to-peak variation are plotted in Fig.5.2b as a function of the shaping strength η for various kinoforms. It is striking that the peak-to-peak value actually increases when the mean value decreases, which shows that the peak-to-peak variation is not due to noise. When all pixels are turned on, the signal varies by less than 0.5%, meaning that unshaped kinoforms can be displayed by our script with no time variation beyond noise.

To show that it *is* possible to display shaped kinoforms without time variation, we replace the photodiode with a camera and load a shaped kinoform with the script and with the GUI. We use our beamshaping algorithm (see Sec.3.2) to create a kinoform and obtain the shaping strength $\eta(y)$ by counting the number of off-pixels per column. The gaussian-fitted $I_{\text{peak}}(y)$ values of a shaped horizontal linefocus above lasing threshold ($I_{\text{LD}} = 43.9\text{mA}$) are shown as a function of shaping strength $\eta(y)$ in Fig.5.2a. We stress the fact that the kinoforms loaded to the DMD are identical in both cases. The figure shows that the GUI-loaded kinoform removes less intensity per off-pixel than the script-loaded kinoform. Linear fits find $\frac{dI}{d\eta} = -62.3 \pm 0.47 \text{ ADU}$ and $\frac{dI}{d\eta} = -39.5 \pm 0.86 \text{ ADU}$ for the script-loaded and GUI-loaded kinoforms respectively. This behavior indicates that, when addressed by the script, the DMD displays pixels that should be fully on as 'partially' off. At $\eta = 1$ the intensity should of course go to zero, but the linear fits find $I_{\text{peak}}(\eta = 1) = 9.6 \pm 0.57 \text{ ADU}$ (GUI) and $I_{\text{peak}}(\eta = 1) = -15.2 \pm 0.47 \text{ ADU}$ (script). We conclude that $I_{\text{peak}}(\eta)$ is not linear, regardless of how kinoforms are loaded. The other fitparameters did not exhibit relevant differences between the two situations, see Table 5.2.

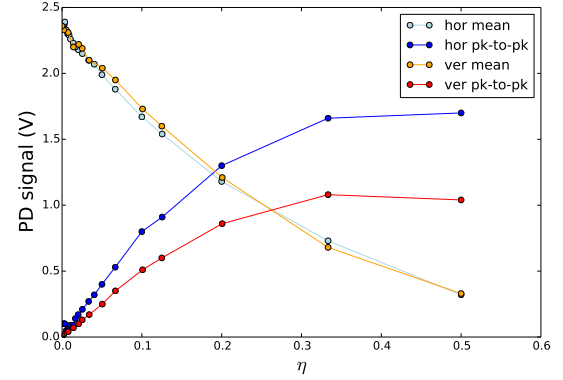
Not only the value of I_{peak} is affected by the periodic flipping of mirrors, but also its time variation. Fig.5.2b shows that the time variation of I_{peak} decreases with η for the GUI loaded images, but increases with η for the script-loaded images. Linear fits find $\frac{d\text{var}(I)}{d\eta} = -0.72 \pm 0.033 \text{ ADU}$ and $\text{var}(I(\eta = 1)) = 0.39 \pm 0.022 \text{ ADU}$ for the GUI-loaded images but $\frac{d\text{var}(I)}{d\eta} = 1.67 \pm 0.055 \text{ ADU}$ and $\text{var}(I(\eta = 1)) = 2.74 \pm 0.036 \text{ ADU}$ for script-loaded images. This positive slope is consistent with the increased peak-to-peak variation found in Fig. 5.2b. As usual, the time variation is average the standard deviation of each pixel over 50 shots recorded over $\sim 25\text{s}$. The camera integration time is 12 ms.

Note that, for $\eta \approx 0$, both I_{peak} and its time variation are approximately the same for both ways of loading kinoforms.

¹²Recall that we defined shaping strength $\eta(y)$ as the fraction of pixels turned off (in a DMD-row or -column).



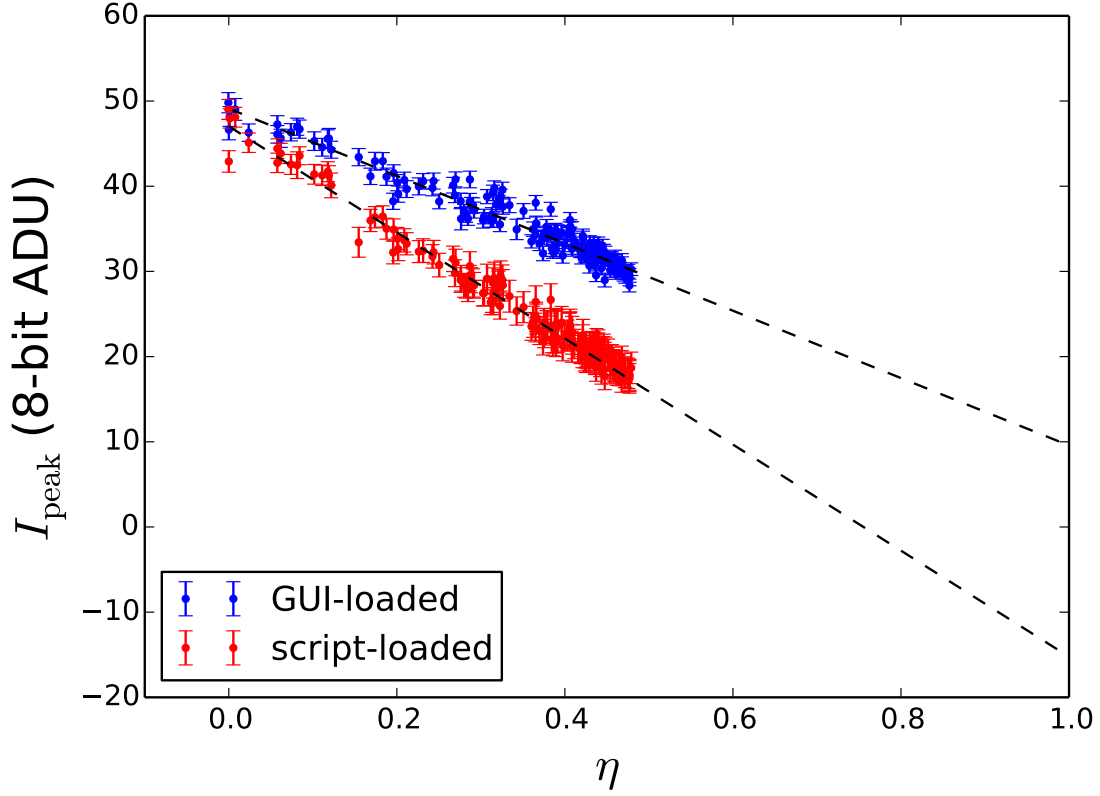
(a) An example of the fluctuation of the PD-signal when a horizontal grating with pitch of 25 pixels and linewidth of 1 off-pixel ($\eta = 0.040$) is shown on the DMD using our script. The period of this periodic signal is 17.8ms, recorded with a Tektronix TDS2022B digital oscilloscope.



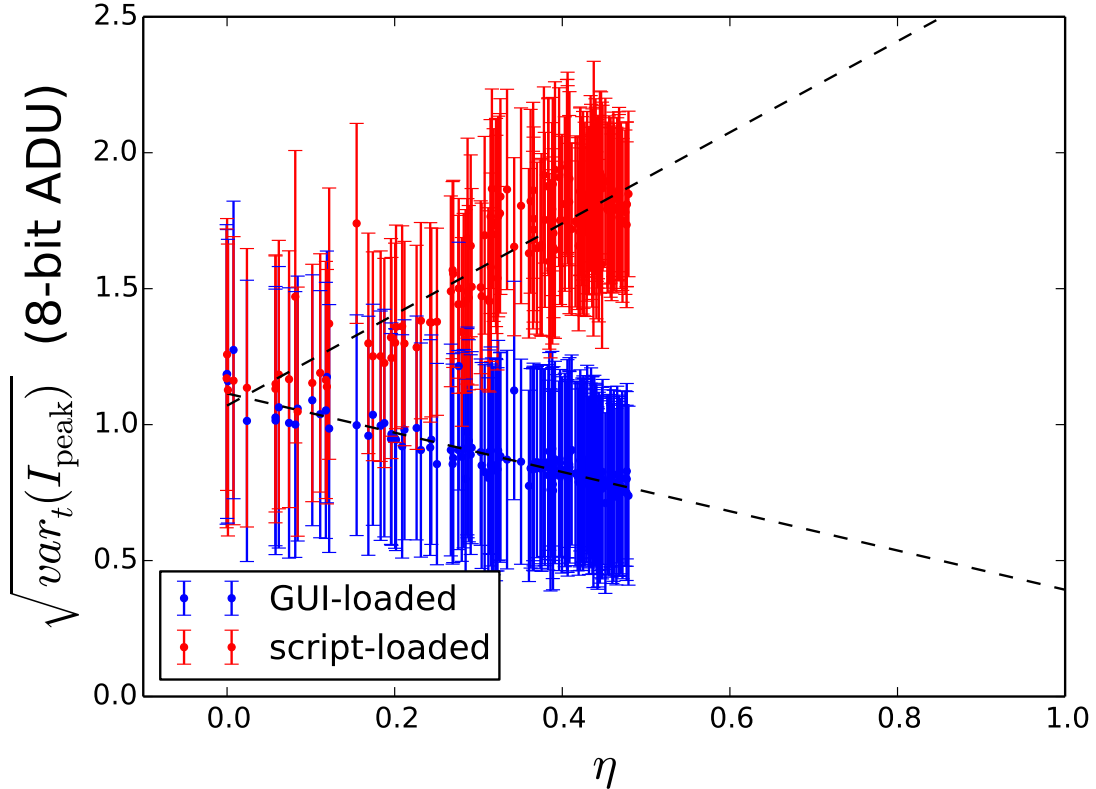
(b) This figure shows the peak-to-peak and mean PD-voltages as a function of shaping strength for horizontal and vertical gratings with a linewidth of one pixel but a varying pitch. The PD-voltage is proportional to the total power emitted in the blazed order of the DMD and $I_{LD} = 43.9\text{mA}$. The kinoforms are horizontal and vertical gratings with a linewidth of 1 pixel and varying pitches and are displayed using our own script.

We conclude this section by specifying the procedure that we use to load static images with the GUI:

- Prepare a beamshaped kinoform (as described in Sec. 3.2), save it as a 24-bit bitmap (three 8-bit color channels) where all colors are either fully black (0,0,0) or fully white (255,255,255).
- Use a Windows operating system to start the Lightcrafter GUI and create a new firmware set which includes the beamshaped kinoform, compile it and load it to the DMD.
- Now use the Pattern Sequence mode to load the image from the firmware to the pattern sequence, making sure to flip it both horizontally and vertically.
- To prevent the DMD from refreshing the image, set 'Pattern Exp = Trigger' and set the Pattern Exposure Time to a value larger than the Internal Trigger Time.
- Hit the Display button and record the GUI loaded image.



(a) Comparison between the time-fluctuation of a single kinoform loaded with the GUI or with our own script. The data points are means of fifty images recorded at random intervals over about 25s and an error bar represents the standard deviation of a data point over those fifty images. The camera integration time is 12ms. The black lines are linear fits of the form $a(\eta - 1) + b$, see text for values. To reduce cluttering five camera pixels and their errors are binned into a single data point .



(b) The time variation of the data in Fig. 5.2a, plotted against shaping strength. The error bars give the average fitting error of I_{peak} at the appropriate position. The black lines are linear fits of the form $a(\eta - 1) + b$, see text for values. The camera integration time is 12ms. To reduce cluttering five camera pixels and their errors are binned into a single data point .

Parameter	Horizontal above lasing threshold	
	Script loaded	GUI loaded
Intensity I_{peak} (ADU)	$25.9 \pm 1.7 \pm 0.3$	$35.6 \pm 0.9 \pm 0.4$
FWHM (μm)	$16.6 \pm 0.4 \pm 0.3$	$16.5 \pm 0.4 \pm 0.2$
Mean position μ (μm)	$-42.8 \pm 1.0 \pm 0.1$	$-54.46 \pm 1.9 \pm 0.08$
Background I_{bg} (ADU)	$0.24 \pm 0.02 \pm 0.04$	$0.25 \pm 0.03 \pm 0.04$

Table 5.2: Average values of the gaussian fit-parameters for linefoci recorded with a camera integration time of 12ms. The first number indicates the average of the fit-parameter (e.g. $\langle \langle \text{FWHM}(y, t) \rangle_t \rangle_y$), the second its time variation (e.g. $\langle \sqrt{\text{var}_t(\mu(y, t))} \rangle_y$), and the third its average fitting error. In both cases, fits are calculated from a ROI 200 pixels wide.

5.4 Alignment of the hybrid mode setup

For the benefit of the reader, the requirements that should be satisfied to successfully operate the DMD in hybrid mode are summed up in Table 5.3.

Requirement	Consequence if not satisfied
Blazed order departs DMD-surface perpendicularly ($\theta_{\text{in}} \sim 26.4^\circ$)	Variation in y of FWHM, only partial imaging
Camera parallel to DMD surface	Variation in y of FWHM, only partial imaging
Beam incident from the right (when facing DMD)	Outer 10 px are permanently 'on'.
Through center of spherical and cylindrical lens	Aberrations, wiggly linefocus
Precise placement of lenses along optical axis	Image- and Fourier planes do not coincide
Collimated incident beam	Image- and Fourier planes do not coincide
Cylindrical lens oriented parallel to a DMD-edge	Variation in y of FWHM due y -dependent clipping
for pulses: y in plane with diffraction angle	(extreme) increase of the FWHM

Table 5.3

5.5 Outlook

The objective of this thesis is to beamshape ultrashort pulses, so in this outlook we will first sum up the steps that remain to achieve this goal. Secondly we will list some minor improvements that could be made.

- Improve our script so that it loads truly static kinoforms to the DMD.

- To check the effect of high magnification and high NA, reproduce the CW shaping results using the microscope objective. One may also check whether the best results are obtained when the target plane is in the front or the back focal plane of the objective.
- Try to beamshape ultrashort pulses.
- Instead of shuffling randomly, use a non-trivial probability function to distribute off-pixels within a kinoform-column. In principle, this allows phase control, allowing the focus to be shaped in the transverse direction.

Minor improvements:

- Since the peak intensity is the most relevant parameter in non-linear optics experiments, it is better to beamshape a linefocus using I_{peak} as a target variable, rather than the (quicker) summed intensity S_{BS} .
- Improve the accuracy of the CCD-DMD mapping by recording the pointspread function of each (visible) column and fitting its mean position, instead of assuming a linear map between the end-points.
- Measure I_{peak} as a function of η all the way to $\eta = 1$ to see if it is truly non-linear.

6 Conclusion

In this thesis we have developed a setup which combines the strengths of image- and Fourier-mode setups and have shaped the intensity of infrared CW-light in a target plane, using a DMD as a spatial light modulator. Our beamshaping method allows us to create a flattop with 4.3 rms-error and approximate translational symmetry over 3 mm. The estimated total power efficiency of our method is $34 \pm 10\%$. For CW-light at $\lambda = 777 \pm 8.3$ nm, the dispersion of the linefocus that occurs when passing broad spectra over a diffraction grating was solved by orienting the cylindrical lens so that it images the dispersion. The only source of broadening left in the longitudinal (imaged) direction is the λ -dependence of the point spread function of the imaging system. The main source of time variation of the shaped intensity is understood, enabling more precise beamshaping in future experiments. The technique is ready to be attempted with ultrashort pulses.

7 Acknowledgements

I would like to thank my thesis supervisor, Dries van Oosten for trusting us to run his lab with a minimum of supervision. Big thanks are due to my friend and labmate Gordian Zomer. We started out on this project together, and if not for him, I would never have been able to unlock the DMD. I would like to thank the PhDs: Ole, Sebas, Sandy and Arjon, and prof. P. van der Straten for having open doors and helping me with many questions. To all the other master students - Marcel Scholten, James Findley de Regt, Jasper Smits, Broos Vermeulen, Qiao Li, Jasper Clarijs and Koen Sponselee - I would like to say: thanks for all good and interesting times, I hope to be seeing more of you in the future.

I will end by acknowledging the essential support of our technicians: Cees de Kok, **o**Paul Jurrius and Dante Killian.

Appendix A The paraxial approximation leads to Fourier optics

We have used the term 'Fourier plane' to designate the back focal plane of a lens, and we have used the result that the electric fields in the back and front focal plane of a spherical lens are related by Fourier transformation. In this appendix we will back up this statement with a derivation.

For an arbitrary initial field in a source plane $z' = \text{constant}$, the scalar Kirchhoff diffraction integral [8] gives the field in the parallel target plane $z = \text{constant}$:

$$E(x, y, z) = \frac{1}{i\lambda} \iint_{-\infty}^{+\infty} E'(x', y', z') \frac{\cos(\theta_{n,r})}{r(x, y, z, x', y', z')} \exp(ikr(x, y, z, x', y', z')) dx' dy'. \quad (\text{A.1})$$

Here E', x', y', z' and E, x, y, z are the scalar electric fields and the coordinates in the source and target planes respectively, $\mathbf{k} = (k_x, k_y, k_z)$ is the wavenumber ($|\mathbf{k}| = 2\pi/\lambda$), $\theta_{n,r}$ is the angle between \mathbf{r} and the unit vector normal to either plane, and \mathbf{r} is the vector connecting point (x', y', z') and (x, y, z) . In what follows, primed coordinates are always used for the source plane and unprimed coordinates for the target plane.

Heuristically, this integral can be understood by Huygens' principle, which states that every point on the wavefront of a light wave acts as a spherical source and that all these sources are in phase. The field of a spherical wave emitted by a point source at \mathbf{x}'_0 is $\mathbf{E} \exp(ikr(\mathbf{x}'_0, \mathbf{x})) \frac{1}{r(\mathbf{x}'_0, \mathbf{x})}$, and the integral over $dx' dy'$ sums over a continuum of point sources in the source plane. Note that kr here is a scalar, because \mathbf{k} and \mathbf{r} always align for a spherical wave. By starting with this scalar form of the Kirchhoff diffraction integral we work in the approximation that the polarization of the electric field changes only negligibly for the k -vectors that significantly contribute to the integral. Recall that, in homogeneous media, the Maxwell equations always require the polarization of plane waves to be perpendicular to \mathbf{k} . In this approximation we can therefore ignore the vectorial nature of the electric field and simply write scalar electric fields that are understood to have some polarization in the x, y plane.

This integral cannot generally be solved except by computationally expensive numerical methods. However, for beams of light we can make some approximations that lead to the so-called Fraunhofer limit, where the relation between E' and E reduces to little more than a Fourier transformation, which is quickly computed using the Fast Fourier Transform algorithm. This limit will be derived next, following the derivation in Ref. [6]. From the field in the Fraunhofer limit it will be easy to show why lenses perform Fourier transformations between their back and front focal plane.

We consider the limit $z \gg x, y$, which is valid for electric fields that decline rapidly with

x and y but not with z , such as narrow beams of light propagating in the z -direction. The same requirement holds for the primed coordinates. Then

$$\cos(\theta_{n,r}) \approx 1,$$

$$\frac{1}{r} \approx \frac{1}{z} + \mathcal{O}(1/z^2),$$

and, placing the source plane at $z' = 0$ without loss of generality,

$$\exp(ikr) = \exp(ikz\sqrt{1 + \frac{(x' - x)^2}{z^2} + \frac{(y' - y)^2}{z^2}}) \approx \exp(ikz(1 + \frac{(x' - x)^2}{2z^2} + \frac{(y' - y)^2}{2z^2}) + \mathcal{O}(1/z^3)).$$

Where we have Taylor expanded in the small parameter $1/z$. Note that we include quadratic terms in the Taylor expansion of r in the exponential but not in the fraction. This is done because the phase factor is much more sensitive to change in r than the $1/r$ factor is. Inserting these approximations, Eq.A.1 can be rearranged to:

$$E(x, y, z) = \frac{1}{i\lambda z} \exp(ik(z + \frac{x^2 + y^2}{2z})) \iint_{-\infty}^{+\infty} E'(x', y', 0) \exp(\frac{ik}{2z}(x'^2 + y'^2 - 2xx' - 2yy')) dx' dy'.$$

Now, only the quadratic terms in x'^2 and y'^2 stand in the way of reducing this integral to a 2D Fourier transform. Therefore we introduce the final approximation: $2z \gg k(x'^2 + y'^2)$, which leads us to the Fraunhofer limit¹³. We did not need to make a similar approximation for x^2 and y^2 because they could be taken out of the integral. The final result is

$$E(x, y, z) = \frac{1}{i\lambda z} \exp(ik(z + \frac{x^2 + y^2}{2z})) \iint_{-\infty}^{+\infty} E'(x', y', 0) \exp(\frac{-ikx}{z}x') \exp(\frac{-iky}{z}y') dx' dy',$$

so that we have the relation

$$E(x, y, z) = \frac{1}{i\lambda z} \exp(ik(z + \frac{x^2 + y^2}{2z})) \mathfrak{F}_{2D}\{E'(x', y', 0)\}(\frac{kx}{2\pi z}, \frac{ky}{2\pi z}). \quad (\text{A.2})$$

¹³For our infrared laser $k \approx 8 \cdot 10^6 m$ and $x, y \sim 0.5 \cdot 10^{-2} m$ (we use a relatively large beam), this means that the Fraunhofer limit accurately describes the field only for $z \gg 200m$. This estimate shows why the Fraunhofer limit is said to describe the *far field*.

It is important to realize that the source field is Fourier transformed with respect to the spatial coordinates of the target plane (times the factor $\frac{k}{z}$), not with respect to more common variables like time or momentum. The far field therefore displays the spatial frequencies of the source field, where low spatial frequencies are close to the optical axis and high spatial frequencies are furthest away. The Fraunhofer limit shows why even a beam with a gaussian beam profile, which is the only function that retains its form under Fourier transformation, cannot be collimated perfectly.

Somewhat confusingly, all approximations applied above are considered versions of the *paraxial approximation*.

Since a lens reproduces the field at infinity in its focal plane, the Fraunhofer limit shows that the E -fields in the front focal plane and the back focal plane of a lens are related by the (Fourier) transform Eq. A.2, thus motivating the name *Fourier plane* to indicate the back focal plane in this context.

In practice the field in the front focal plane of a lens is not an exact Fourier transform of the field in its back focal plane because non-idealized optics always has a so-called *point spread function*, due to the finite dimensions of the lenses. The point spread function between the plane $z' = 0$ and the plane $z = \text{constant}$ is found by computing $\mathbf{I}(x, y, z)$ using Eq. A.1 for an input field $E(x', y', 0) = E_0 \delta(x' - x'_0) \delta(y' - y'_0)$ and a given optical system through which it propagates. The optical system is incorporated into the integral by letting the wavenumber depend on space in a specific way.

References

- [1] L. Brillouin. *Wave propagation and group velocity*. Academic Press.
- [2] A.L. Gaunt and Z. Hadzibabic. Robust digital holography for ultracold atom trapping. *arXiv preprint arXiv:1111.5941*, 2011. 5.2
- [3] S.A. Goorden, J. Bertolotti, and A.P. Mosk. Superpixel-based spatial amplitude and phase modulation using a digital micromirror device. *Optics express*, 22(15):17999–18009, 2014. 1.3, 5.2
- [4] P.A. Himmer, D.L. Dickensheets, and R.A. Friholm. Micromachined silicon nitride deformable mirrors for focus control. *Optics Letters*, 26(16):1280–1282, 2001. 1.2
- [5] Jinyang L., R. Kohn Jr, M F Becker, D J Heinzen, et al. 1.5% root-mean-square flat-intensity laser beam formed using a binary-amplitude spatial light modulator. *Applied optics*, 48(10):1955–1962, 2009. 1.3, 2, 3.3.4
- [6] W. Lauterborn, T. Kurz, and M. Wiesenfeldt. *Coherent Optics, Fundamentals and Applications*. Springer-Verlag, Berlin, Germany, 2nd edition, 1999. A
- [7] D. Maystre. Diffraction gratings. *Scholarpedia*, 7(6):11403, 2012. revision 143446. 1.3.1
- [8] L. Novotny and B. Hecht. *Principles of nano-optics*. Cambridge University Press, 2012. A
- [9] C.A. Palmer and E.G. Loewen. *Diffraction grating handbook*. Newport Corporation Springfield, Ohio, USA, 2005. 1.3.2
- [10] N. Sanner, N. Huot, E. Audouard, C. Larat, J. Huignard, and B. Loiseaux. Programmable focal spot shaping of amplified femtosecond laser pulses. *Optics letters*, 30(12):1479–1481, 2005. 1.2
- [11] Texas Instruments. *DLPC350 Programmer’s Guide*, 5 2013. Rev. Feb. 2015. 5.3
- [12] Texas Instruments. *DLP4500NIR 0.45 WXGA Near-Infrared DMD*, 2 2014. Rev. A, <http://www.ti.com/product/DLP4500NIR/datasheet>. 1.2, 1.3
- [13] J.C. Vaughan, T. Feurer, and K.A. Nelson. Automated two-dimensional femtosecond pulse shaping. *JOSA B*, 19(10):2489–2495, 2002. 1.2
- [14] B. Wattellier, C. Sauteret, J-C. Chanteloup, and A. Migus. Beam-focus shaping by use of programmable phase-only filters: application to an ultralong focal line. *Optics letters*, 27(4):213–215, 2002. 1.2
- [15] H. Zhang. Single-shot femtosecond laser ablation on the nanoscale. page 97, 2013.

References

- [16] P. Zupancic. Master's thesis: Dynamic holography and beamshaping using digital micromirror devices. *LMU München, Greiner Lab Harvard*, 2013. 1.3, 5.2